Experimental Studies of Atom-Photon Interaction with Rydberg Atoms

A Thesis presented for the degree of

Doctor of Philosophy

by

Shovan Kanti Barik.

(Enrollment No: RRI/2017/012)

Under the guidance of

Supervisor: **Dr. Sanjukta Roy**

Co-Supervisor: **Dr. Saptarishi Chaudhuri**



Raman Research Institute
India

February 2025

Abstract

In this thesis, we report our studies of Rydberg atom-light interactions and interactions between Rydberg atoms in cold and thermal ensembles. Our studies focus on alkali ^{87}Rb atom which has an energy structure similar to that of a Hydrogen atom.

Rydberg atoms [1] are highly excited atoms where one or more electrons are excited to the orbitals far away from nucleus with large principal quantum number, n. The excitation of atoms to the Rydberg state is performed using lasers through single photon [2] or multi-photon excitation process. In case of single-photon excitation, a single photon with sufficient energy is absorbed by the atom, exciting an electron directly to a Rydberg state. This sufficient energy or frequency of the photon should be equal to the energy difference between the ground state and the Rydberg state. In a multi-photon process, multiple lower energy photons are used sequentially to excite the atom to the Rydberg state. An atom in a Rydberg state has very distinct properties due to the large spatial extension of its orbitals compared to an atom in its ground state. Due to their large size, Rydberg atoms are highly polarizable and extremely sensitive to the external electric fields. Thus Rydberg atoms play a significant role in Quantum sensing [3, 4]. Rydberg atoms have very long life-times compared to the atoms in their ground states. This is because the wave-function overlap between the ground state and the Rydberg state is typically negligibly small. In other words, the transition dipole matrix element is very weak between these states which results in a slower decay of the Rydberg states. The long life-times of Rydberg atoms enhances the coherence time of Quantum superposition involving these states. The enhanced coherence time is immensely crucial for implementation of high-fidelity quantum gates [5]. Besides, long lived Rydberg states can be used as frequency standards and precise spectroscopic measurements, which are very useful in atomic clocks [6] to be used in navigation system and synchronization protocols.

Due to their large dipole moments ($\propto n^2$), dipole-dipole and Van der Waals interactions play important roles in influencing the behaviour and properties of the Rydberg atomic systems especially in cold Rydberg atoms. Dipole-dipole interac-

tion in Rydberg atoms leads to the several interesting phenomena such as Rydberg blockade [7, 8] and collective-excitations [9]. Rydberg blockade emerges when two Rydberg atoms are brought close together, the strong dipole-dipole interaction prevents both the atoms from simultaneously going to the Rydberg state. Dipole-dipole interaction varies as $\frac{n^4}{R^3}$, R is the inter-atomic distance between two atoms. The Van der Waals interaction between Rydberg atoms arises when two atoms are excited to the same Rydberg state resulting in interaction which varies as $\frac{n^{11}}{R^6}$. Both the effect of Rydberg blockade and Van der Waals interactions have been utilized in quantum information processing like implementation of two-qubit quantum gate [10, 11], ensemble qubits [7], Quantum memory [12] etc.

One of the convenient ways of detecting Rydberg excitation in an ensemble of neutral atoms is to use Electromagnetically Induced Transparency (EIT) [13]. EIT is one of the striking phenomena of atom-light interactions that can lead to dramatic changes in transmission and absorption properties of a medium. It was first observed experimentally by Haris et al in 1991 while working with Sr atoms. Specifically, the presence of a coupling beam makes the medium transparent to a probe laser at a particular frequency in a three-level system. This effect arises due to coherent interaction between coupling and probe laser with the atomic ensembles. Rydberg Electromagnetically Induced Transparency (Rydberg EIT) [14] combines the aspects of EIT and unique properties of Rydberg atoms, offering new possibilities for strong, tunable light-matter interactions. Rydberg EIT has been used for RF sensing [15, 16], slowing light [17], to name a few.

In this thesis, I start by presenting the results on a comprehensive measurement of Rydberg excitation in neutral ^{87}Rb. Next, I shall describe the technique of Doppler enhanced magnetometry with thermal Rydberg atoms to detect weak magnetic fields. In conventional setup for three level ladder system Rydberg EIT, a probe laser connecting ground state $|g\rangle$, intermediate state $|e\rangle$ and a strong coupling laser connecting intermediate state, Rydberg state $|r\rangle$ are aligned in counter-propagating configuration to reduce the Doppler mismatch. Here we show, on the contrary, that one can harness Doppler shifts in a co-propagating arrangement to produce an enhanced response to a magnetic field. In particular, I demonstrate an order-of-magnitude enhanced splitting in the transmission spectrum as compared to the counter-propagating case.

Thereafter I shall describe our cold atom setup. We cool and trap ^{87}Rb atoms in a Magneto Optical Trap (MOT) with temperature few hundreds of micro-Kelvins. We have performed sub-Doppler cooling to reduce the MOT cloud temperature down to twenty of micro-Kelvin. Sub-Doppler cooling plays a crucial role in preparing ultracold atoms for loading into optical dipole trap from MOT. We utilize two-photon excitation to prepare the atoms in high Rydberg states. One important feature of a Rydberg state is that it cannot be trapped in a MOT; rather, it will be lost from the trap. We have performed a comprehensive study of trap-loss spectroscopy in the time of flight measurement. Our study involves how the variation of effective two-photon Rabi frequency and excitation time affect the atom loss from the trap. Additionally, I shall present experimental results on Autler-Townes splitting in the cold atom setup.

Experiments with thermal atoms: Quantum sensors based on their Quan-

tum properties viz. interference, superposition, entanglement and squeezed states are used to precisely measure the physical quantities. The advantage of these sensors is that they don't require frequent calibration since atomic properties remain the same anywhere and anytime across the universe. Precision magnetometry has diverse application, including geophysics, medical imaging, material characterization, space exploration etc. In this experiment, we utilize the aspects of EIT, in combined with thermal Doppler shifts, to demonstrate the enhanced response to magnetic field of thermal atoms. In a conventional three level ladder type EIT setup, a weak probe beam(ω_p) is counter-propagated with a control beam (ω_c) to reduce the Doppler broadening and Doppler shift of the transmission peak of probe beam. In contrast, we demonstrate an order of magnitude enhancement of the magnetic-field response in a copropagating arrangement for various polarizations of the two lasers, compared to their counterpropagating configuration. The experimental setup is shown in figure 1a). In this figure, red colored beam represents the probe beam (780 nm) which split into two parts. One beam acts a probe beam and another acts as a reference beam. Probe beam has Gaussian radius of 0.7 mm. Blue colored beam (480 nm) is represented as a coupling beam. A pair of counter-propagated coupling beams are aligned with the probe beam co-axially so that one pair of probe and coupling beam serves as co-propagating EIT configuration, while other pair serves as counter-propagating configuration.

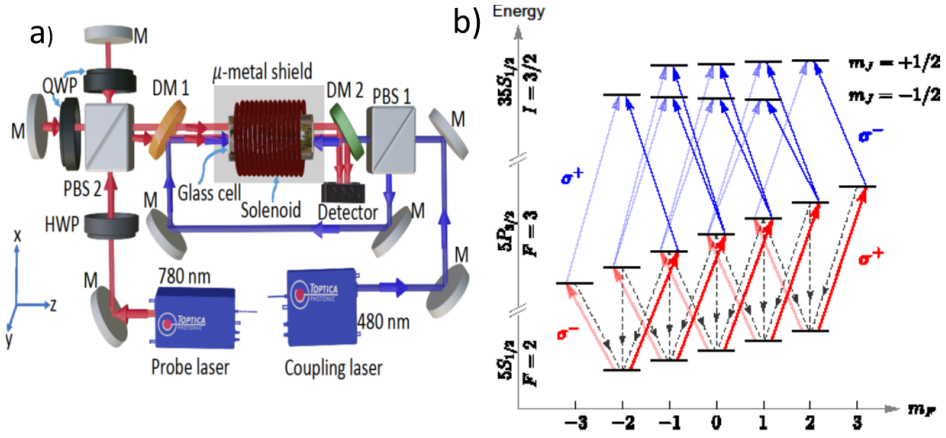


Figure 1: a)Experimental setup for Doppler enhanced quantum magnetometry. b) Energy levels diagram for ^{87}Rb under magnetic field

A solenoid coil of 33.61 Gauss/Amp field gradient with current is used to generate magnetic field along it's axis (z-axis). A ^{87}Rb thermal vapor cell is kept along coil's axis to observe the effect of magnetic field on EIT transmission peak. The level diagram for ^{87}Rb for this experiment is shown in figure 1b). Probe laser is scanned across hyperfine level $\{5S_{\frac{1}{2}}, F = 2\}$ to $\{5P_{\frac{3}{2}}, F' = 3\}$ transition, while coupling laser tuned from $\{5P_{\frac{3}{2}}, F' = 3\}$ to $\{35S_{\frac{1}{2}}, F'' = 2\}$ transition. Under the magnetic field ground state hyperfine level is Zeeman split to 5 sublevels with energy $\epsilon(m_F^g) = g_F^g m_F^g \mu_B B$, B magnetic field. g_F^g is Lande g-factor for ground state, μ_B is Bohr

Magneton and $m_F^g \in \{-2, ..., +2\}$ Similarly, due to the Zeeman splitting, the excited state $\{5P_{\frac{3}{2}}, F' = 3\}$ has 7 sub-levels with energies $\epsilon(m_F^e) = \epsilon_{g,e} + g_F^e m_F^e \mu_B B$, $\epsilon_{g,e}$ is energy with respect to ground state at zero magnetic field. However, in Rydberg manifold, a few Gauss of magnetic field is sufficient enough to decouple the angular momentum state $J = \frac{1}{2}$ from nuclear spin state $I = \frac{3}{2}$, resulting in the Paschen-Back effect. Because of this effect, hyperfine levels $F'' = 1$ and $F'' = 2$ are combined to give 8 sub-levels with energies $\epsilon(m_I^r, m_j^r) = \epsilon(g, r) + A_{hf} m_I^r m_j^r + (g_I^r m_I^r + g_j^r m_j^r)\mu_B B$, A_{hf} is hyperfine interaction constant, $\epsilon(g, r)$ energy reference from ground state at zero magnetic field. After solving the Linblad master equation due to the interaction of probe and coupling laser with these atomic levels, we derived an expression for susceptibility(χ_0) as a function of probe frequency at absolute zero temperature. To add the effect of room temperature on the susceptibility, χ_0 is averaged over thermal distribution. So, susceptibility of thermal atoms for the counter-propagation(co-propagation) is given as

$$\chi = \frac{1}{\sqrt{\pi}} \int_{-\infty}^{\infty} \mathrm{d}u \; e^{-u^2} \chi_0\big(\Delta_p + \Delta_p^T u, \Delta_c \mp \Delta_c^T u\big) \; , \tag{1}$$

with $u = v/v_T$, $\Delta_{p(c)}^T \omega_{p(c)} v_T/c$, and $v_T = \sqrt{2k_B T/m}$, m being the mass of a ^{87} Rb atom and k_B the Boltzmann constant.

$\{+, -\}(+, +)$ signs in eqn. 1 are due to the Doppler shift for counter-propagation(co-propagation) cases.

The distinct differences between co-propagating EIT and counter-propagating EIT are the line-width, transmission peak height and peak position of their signals. The line-widths for counter-propagating and co-propagating cases derived as $(1 \mp \frac{\omega_p}{\omega_c})\omega_{ge}$, ω_{ge} is line-width of two level due to lifetime of the excited state. We measure the transmitted signal under magnetic field with different set of coupling-probe laser polarization. In general, peak position changes linearly with magnetic field, with a slope as

$$\frac{\partial \Delta_p}{\partial(\mu_B B)} \approx g_F^e m_F^e - g_F^g m_F^g \mp \frac{\omega_p}{\omega_c}(g_F^e m_F^e - g_J^r m_J^r) \; . \tag{2}$$

The excitation pathways are shown for probe and coupling laser polarization combinations of $\{\sigma^+, \sigma^-\}$ or $\{\sigma^-, \sigma^+\}$ in Fig. 1 b) So for the these circular polarization combinations, single peak changes its position with magnetic field, with a slope given by

$$\frac{\partial \Delta_p}{\partial(\mu_B B)} \approx (1 \mp \omega_p/\omega_c). \tag{3}$$

$\mp$ signs are counter and co-propagation cases respectively.

For the linear-linear polarization case, each EIT peak is split into two peaks under magnetic field. A linear polarized light is combination of two opposite circular polarization. So, for linear-linear polarization combination of probe and coupling lasers, two simultaneous excitation pathways of $\{\sigma^+, \sigma^-\}$ and $\{\sigma^-, \sigma^+\}$ give rise to splitting into two peaks. The relative splitting of two peaks with slope is derived from eqn. 2 as

$$\frac{\partial \Delta_p}{\partial(\mu_B B)} \approx 2(1 \mp \omega_p/\omega_c). \tag{4}$$

$\mp$ signs are counter and co-propagation cases respectively. Thus, we have observed that peaks for co-propagating case exhibit higher splitting rate with magnetic field than that

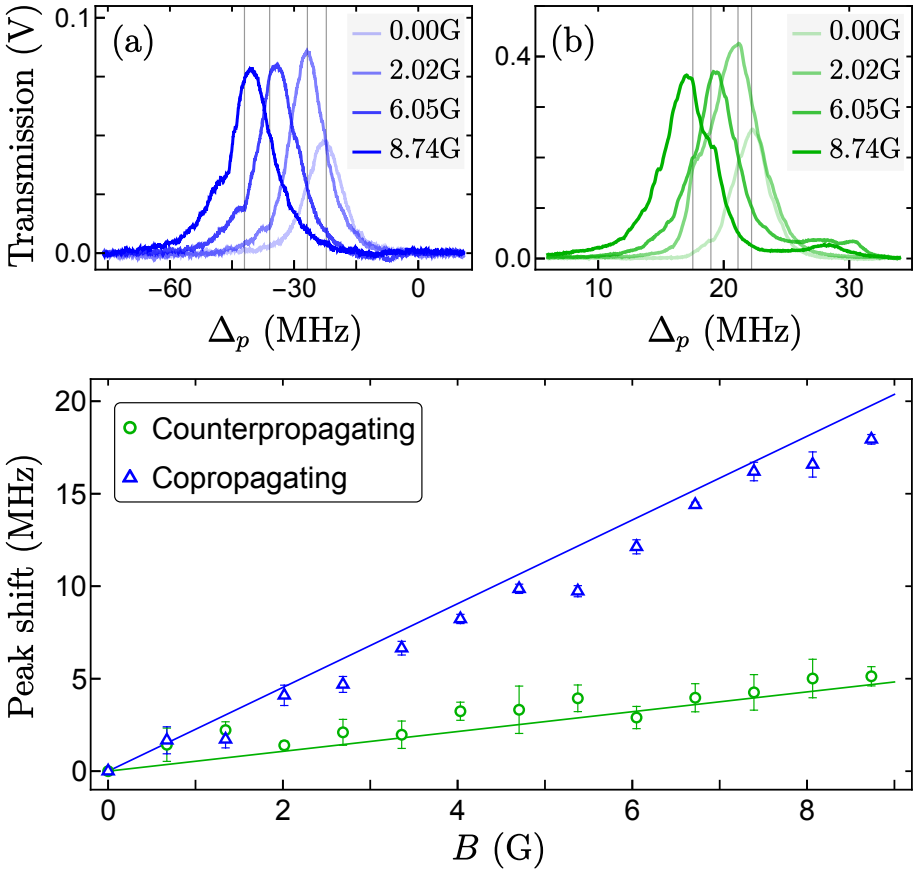


Figure 2: Top: Showing experimental data of EIT signal with magnetic field (B) variation for $\{\sigma^-, \sigma^+\}$ polarization. a)co-propagating configuration b)counter-propagating configuration. Bottom:peak shift with magnetic field. solid line represents theoretical predictions. Magnetic field changed from 0 to 10 Gauss

of counter-propagating case. The enhanced response for co-propagating EIT is given as $\frac{\omega_p+\omega_c}{\omega_p-\omega_c} \approx 4.2$

In Fig. 2, the results from experiment and theroy are given for $\{\sigma^+, \sigma^-\}$ polarization. The experiment and theoretical results for linear-linear polarization are shown in figure 3. In another experiment with the thermal atoms, we use counter-propagating three level ladder type EIT configuration to measure the transition frequencies of high lying Rydberg states($45 < n < 124$) of ^{87}Rb atom. We measure transition frequencies of $nS_{\frac{1}{2}}$, $nD_{\frac{3}{2}}$ and $nD_{\frac{5}{2}}$ levels with respect to the $\{5P_{\frac{3}{2}}, F = 3\}$ state. Our accuracy of measurement is limited to $\leq 2MHz$. For high lying Rydberg states $n \geq 81$, we applied lock-in detection technique to improve the signal to noise ratio > 10 of the Rydberg EIT signal. To measure the Rydberg states, we lock the weak probe laser to $\{5S_{\frac{1}{2}}, F = 2\}$ to $\{5P_{\frac{3}{2}}, F' = 3\}$ transition using LIR lock and scan the coupling laser corresponding $\{5P_{\frac{3}{2}}, F' = 3\}$ to nS or nD states. The intensity of the coupling beam is modulated by a mechanical chopper to generate

lock-in signal using a lock-in amplifier (SRS850). The mechanical vibrations originating from the chopper effect the long term stability of EIT signal. Instead, we use another lock-in detection technique where probe laser is frequency modulated and scanned across the probe transition and coupling laser frequency is fixed at the frequency measured from the first lock-in detection technique. Same lock-in amplifier used to generate the lock-in signal.

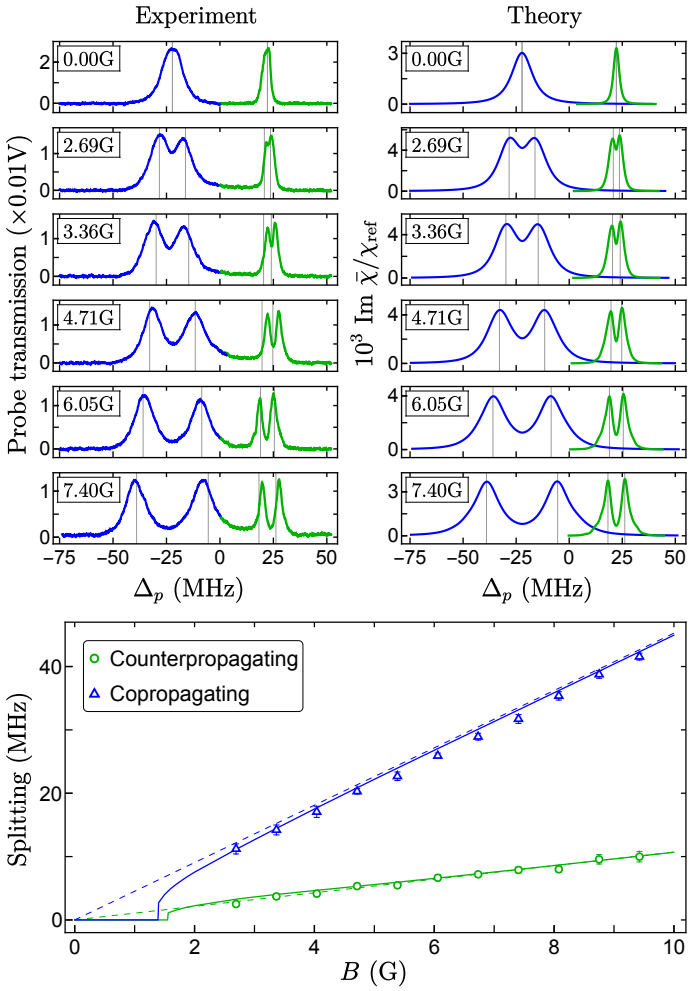


Figure 3: Top: showing experimental data(left)and simulations data(right) with magnetic field . blue curve represents co-propagating EIT, green curve showing counter-propagating EIT. Bottom: relative peak splitting with magnetic field. solid line represents theoretical predictions

In this method, measured lock-in signal is second harmonic of the Rydberg EIT, which is narrower than the Rydberg EIT signal. This lock-in technique is extremely helpful in resolving higher principal number $D_{\frac{3}{2}}$ and $D_{\frac{5}{2}}$ states. The EIT signals corresponding to direct measurement and lock-in amplifier detection are shown in figure 4.

The important outcome of this measurement is that we could address the higher level Rydberg state accurately, using these high sensitive states RF field sensing [18], precision [19] can be performed.

Experiments with cold Rydberg atoms: In our cold experiment setup, atoms are cooled and trapped using Magneto Optical Trap (MOT), as schematic shown in figure 5a). We can trap ^{87}Rb atom with 10^5 atom number at $\sim$ 150 μK temperature. Cooling and repumper beams are generated from two different External Cavity Diode Lasers (ECDL).

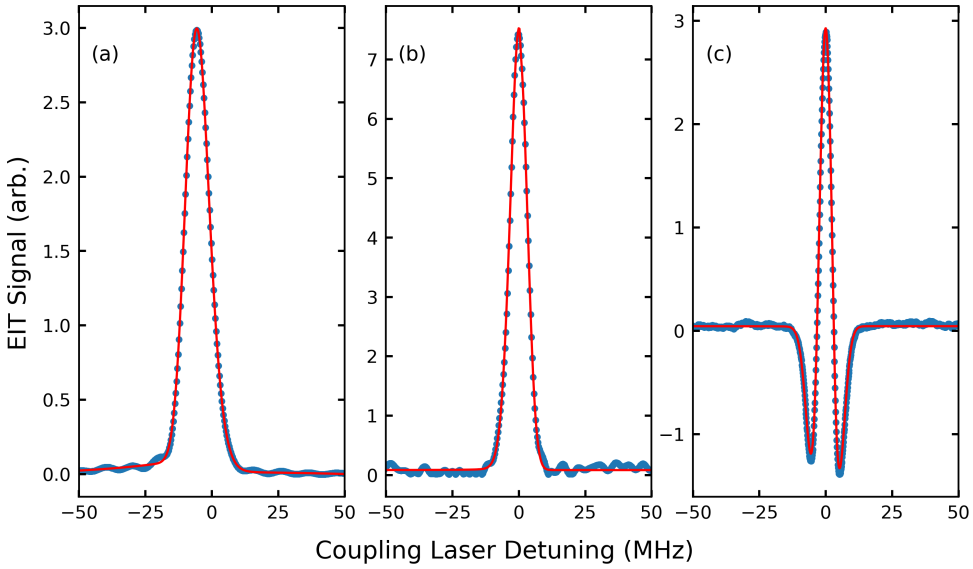


Figure 4: a) EIT signal measured directly, locking the probe laser and scanning the coupling laser. b)lock-in amplifier detection by modulating the coupling laser with mechanical chopper. c)lock-in amplifier detection by modulating the frequency of probe laser.

The locking of cooling and repumper frequencies is based on Saturation Absorption Spectroscopy(SAS) technique with Lock-in-Regulator(LIR) module from Toptica. Frequency of cooling laser is red detuned by 2Γ from $\{5S_{\frac{1}{2}}, F = 2\}$ to $\{5P_{\frac{3}{2}}, F' = 3\}$ (D_2)transition. On the other hand, repumper laser is kept resonant at $\{5S_{\frac{1}{2}}, F = 1\}$ to $\{5P_{\frac{3}{2}}, F' = 2\}$ (D1) transition. The size of atomic cloud is measured to be $\sim 400\mu m$. We image the atomic cloud through fluorescence imaging technique. We have two kind of fluorescence detection setup, one is imaging the whole cloud using an EMCCD camera and other is detecting the fluorescence through high numerical aperture (HNA) lens (see figure 5c) . We have used Avalanche Photo-Detector (APD) to collect the fluorescence through HNA lens by coupling it to the single mode polarization maintaining fiber. Two-photon excitation scheme, as shown in figure 5b), is used to excite the trapped atoms to Rydberg states. In this process, atom is first excited to an intermediate state by one photon and the Rydberg excitation is performed by another photon, connecting intermediate state to Rydberg state. We use 780 nm laser and 480 nm laser in a counter-propagation setup for two photon Rydberg excitation, as shown in figure 5a). The 780 nm laser is drawn from an ECDL, locked using SAS spectroscopy technique and 480 nm laser is generated from TOPTICA SHG pro.The 780 nm laser is blue detuned by Δ =487

MHz to the $\{5S_{\frac{1}{2}}, F = 2\}$ to $\{5P_{\frac{3}{2}}, F' = 3\}$ transition to avoid decoherence due to excited state $\{5P_{\frac{3}{2}}, F' = 3\}$ high decay rate. The 480 nm laser is red detuned by same amount from $\{5P_{\frac{3}{2}}, F' = 3\}$ to $nS_{\frac{1}{2}}$ transition to match the two photon resonant condition. In this technique, if Ω1,Ω2 are the rabi frequencies of these two transitions, then effective rabi frequency of the two photon excitation scheme is given as $\frac{\Omega_1\Omega_2}{2\Delta}$. Trap loss spectroscopy [20] is one of the techniques to detect the Rydberg atoms. If an atom is excited to the Rydberg states then it will no longer be in MOT cooling cycle, so it will not see any MOT potential, eventually be lost from the trap. In this experiment, we have measured the trap-loss due to the Rydberg excitation to $nS_{\frac{1}{2}}$ states. After the Rydberg excitation, the trap-loss is measured by

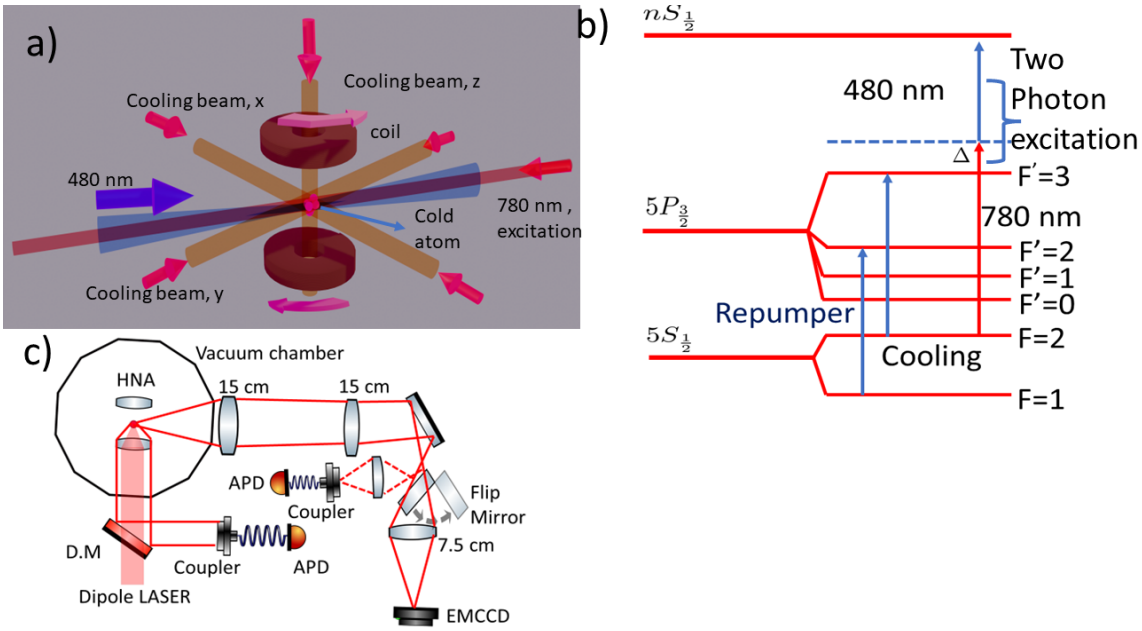


Figure 5: a) schematic of MOT setup and two photon excitation lasers are shown. b)level diagram of MOT and two photon excitation scheme.It shows the excitation from $5S_{\frac{1}{2}}$ to $5P_{\frac{3}{2}}$ using 780 nm and excitation from $5P_{\frac{3}{2}}$ to $nS_{\frac{1}{2}}$ using 480 nm laser. c)This figure shows fluorescence imaging setup using APD and EMCCD camera.

switching off the MOT to prevent the loading of additional atoms.

In figure 6a), fraction of atom loss is measured at different excitation time while keeping the effective Rabi frequency constant at different values. In figure 6b), fraction of atom loss is also measured at different detuning while keeping effective Rabi frequency and excitation time fixed at 31 KHz, 100 ms respectively.

We have also measured the Autler-Townes spectra of three level ladder system by using trap-loss spectroscopy, the experimental setup is same as shown in figure 5. The trap-loss signal is recorded by an APD kept at the fluorescence imaging path, as shown in figure 5c). The strong MOT cooling beam (780 nm) is used to dressed the the cooling transition $\{5S_{\frac{1}{2}}, F = 2\}$ to $\{5P_{\frac{3}{2}}, F' = 3\}$ state. The 480 nm laser tuned to the Rydberg state $(nS_{\frac{1}{2}})$ from $\{5P_{\frac{3}{2}}, F' = 3\}$, is used as probe laser for the trap-loss measurement. The results shows that the broadening of Autler-Townes peak at higher principal quantum number due to long range-interaction among Rydberg

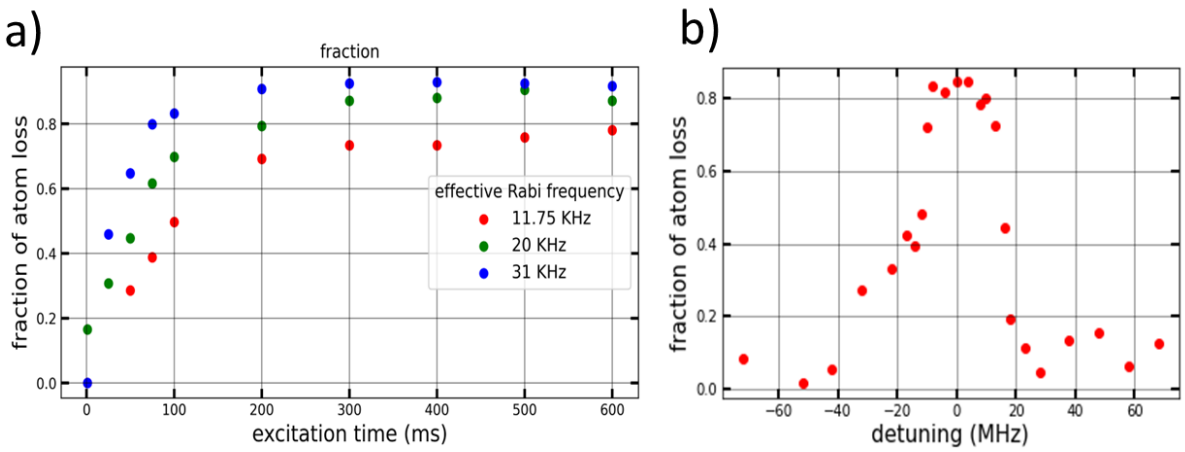


Figure 6: a) showing fraction of atom loss vs different excitation time at three different effective Rabi frequencies b)fractional atom loss measured vs different detuning while keeping excitation time and effective Rabi frequency at 100 ms, 31 KHz respectively

atoms.

Our system is also equipped to trap single atom or multi atoms. We use 850 nm laser for trapping ^{87}Rb atom in the dipole trap. The 850 nm laser, as shown in figure 5c), is tightly focused to a diffracted limited spot size on the MOT centre by the HNA lens (C240TME-B) to trap single atom. Dipole trap depth [21] due to the focused beam is given as $U_0 = \frac{\hbar\Gamma}{2}\frac{P}{\pi\omega_0^2 I_0}\frac{\Gamma}{\Delta}$, P is dipole laser power, ω_0 is beam waist size, Δ effective detuning, I_0 saturation Intensity. The life time of atom in a dipole trap depends on several factors like trap depth, back-ground pressure, scattering from dipole laser, relative intensity noise [22] of dipole laser, initial temperature of atom. Relative intensity noise of dipole trap laser is measured by a spectrum analyzer. For the same trap depth, reducing the initial energy of the loaded atoms could increase the lifetime of the atoms. We have performed polarization gradient cooling of Magneto optically trap atoms, using this technique the atomic cloud temperature is reduced to below 25 μK

Summary and Outlook: We have carried out quantum magnetometry using ^{87}Rb atom using three label ladder type EIT scheme. It is shown that co-propagation EIT scheme has an enhanced response to magnetic field compare to counter-propagation EIT scheme in ladder type system. The enhancement depends on the ratio of probe and coupling frequencies. We could tune the enhancement by targeting different atomic energy levels. This measurement provides strong motivation, potentially leading to important applications in quantum sensing and magnetometry. Another experiment with thermal atoms, we measured the transition frequencies of high principal quantum number Rydberg states using conventional counter-propagating three level ladder type EIT scheme. Using the results from this experiment, we could accurately address the highly sensitive Rydberg states to perform precision electrometry, RF field sensing. In experiments with cold atoms, we have measured traploss spectroscopy due to Rydberg excitation using two photon excitation scheme. This measurement will help us to understand interaction

mechanisms leading to the trap-loss. We further cool the magneto optically trapped (MOT) atom by using polarization gradient cooling. This cooling of MOT atoms will help us to trap the single or multiple atoms in dipole trap. Single atom is an ideal candidate for high sensitive magnetometer [23], using an array of single atom dipole traps, spatially resolved magnetometer can be built. Interaction controlled multiple single-atom dipole traps are useful platform to explore quantum simulation [24], quantum computation [25].

Declaration of Original and Sole Authorship

I, **Shovan Kanti Barik**, declare that this thesis titled **" Experimental Studies of Atom-Photon Interaction with Rydberg Atoms"** and the data presented in it are original and my own work under the supervision of Dr. Sanjukta Roy. I confirm that the work presented here has not been submitted for the award of any other degree, diploma, membership, associateship, fellowship, etc. of any other university or Institute. Keeping with the general practice, due acknowledgements have been made wherever the work described is based on other investigations. I have also run the thesis through the Drillbit plagiarism software.

Shovan Kanti Barik ..... Sanjukta

(Signature of the student) (Signature of the Supervisor)

Shovan Kanti Barik Dr. Sanjukta Roy

Saptarishi

.....

(Signature of the Co-Supervisor)

Dr. Saptarishi Chaudhuri

Date: .....

Place: .....

Certificate

This is to certify that the research presented in this thesis titled **"Experimental Studies of Atom-Photon Interaction with Rydberg Atoms"**, submitted by **Shovan Kanti Barik** (Enrollment no. RRI/2017/012) to **Jawaharlal Nehru University** for the award of the degree of **Doctor of Philosophy** in Physical Sciences, is the bonafide record of original research work carried out by the candidate from July 2017- February 2025, under my guidance and supervision at **Raman Research Institute**, Bengaluru, India. The results embodied in the thesis have not been submitted to any other University or Institute for the award of any degree or diploma.

.....
(Signature of the Director)
Prof. Tarun Souradeep

.....
(Signature of the Supervisor)
Dr. Sanjukta Roy

.....
(Signature of the Co-Supervisor)
Dr. Saptarishi Chaudhuri

Acknowledgements

I am deeply grateful to Dr. Sanjukta Roy and Dr. Saptarishi Chaudhuri for their unwavering mentorship and support throughout my doctoral journey. I also wish to honor and acknowledge my late advisor, Prof. Hema Ramachandran, whose guidance, wisdom, and unwavering support were instrumental to this work. Her memory continues to inspire me.

Dr. Sanjukta Roy's optimism and encouragement during my final years played a crucial role in the completion of my thesis after the unfortunate passing of Prof. Hema. I am also deeply grateful to Dr. Saptarishi Chaudhuri, whose steadfast support and guidance during this difficult period were invaluable. His willingness to intervene, provide thoughtful insight, and help me navigate the challenges that arose ensured the continuity of my research. His mentorship extended beyond academics, offering reassurance and motivation when I needed it the most. The time and effort he dedicated to my progress, along with his patience and encouragement, have had a profound impact on my journey, and I am truly grateful for his unwavering support.

I also extend my gratitude to our collaborators, Shovan Dutta (RRI), Rejish Nath (IISER Pune), and his students Varna, Soham, and Diya, for their valuable contributions to the theoretical support to our experiments. I would also like to express my gratitude to my advisory committee members, including Prof. Reji Philip and C M Chandrashekar. I also acknowledge DST and the funding from the I-HUB Quantum Technology Foundation via the SPIKE Project Grant No. I-HUB/SPIKE/2023-24/004.

I am grateful to Mrs. Meena Suresh, Mr. Mohamed Ibrahim for their invaluable assistance in designing, developing, and characterizing various electronic and mechanical components essential to this work. I also thank all the members in library and computer section for their support. I also thank all the cooks in RMV and Vayalikaval hostel. I sincerely thank my lab members—Silpa, Snehal, Yashica, Sukanya, Venkat, Aishariya, Sagar da, Maheswar da, Sayari, Gourab, Anirban and Swarnva —for their support and assistance in designing and conducting experiments. I also thank my seniors Avik da, Rishav da, Deepak da and Bapan da for creating

a friendly environment around me. I also extend thanks to my juniors Swarnadeep, Sayan, Shoumen, Rupak, Imran, Shuvojit, soumyajit and all other friends at RRI. I also thank my friends Argha, Sandipan, Shuvra, Reshma, Simran for their support and motivation in hard times.

Finally I am deeply grateful to my parents for their unwavering support, sacrifices, throughout the journey. Their unconditional love, encouragement and guidance have been the source of my success.

Shovan Kanti Barik.

List of publications

1. "Transition frequency measurement of highly excited Rydberg states of ^{87}Rb for a wide range of principal quantum numbers", Silpa B S, Shovan Kanti Barik, Saptarishi Chaudhuri, and Sanjukta Roy, Optics Continuum **1** (5), 1176-1192(2022). doi: https://doi.org/10.1364/OPTCON.458153.

2. "Quantum Technologies with Rydberg atoms", Shovan Kanti Barik, Aishwarya Thakur, Yashica Jindal, Silpa B S and Sanjukta Roy, Frontiers in Quantum Science and Technology **3** 1426216 (2024).

3. "Doppler-enhanced quantum magnetometry with thermal Rydberg atoms", Shovan Kanti Barik, BS Silpa, M Venkat Ramana, Shovan Dutta, and Sanjukta Roy. New Journal of Physics, **26** (7):073036, 2024.

4. "Observation of effects of inter-atomic interaction on Autler-Townes splitting in cold Rydberg atoms", Silpa B S, Shovan Kanti Barik, Varna Shenoy, Soham Chandak, Rejish Nath and Sanjukta Roy (Manuscript in preparation).

5. "Rydberg excitation mediated trap-loss in cold atoms", Shovan Kanti Barik, Yashica Jindal, Silpa B S, Varna Shenoy, Soham Chandak, Rejish Nath and Sanjukta Roy (Manuscript in preparation).

Student Supervisor Co-Supervisor

Contents

Abstract **ii**

Declaration **xii**

Certificate **xiv**

Acknowledgements **xv**

List of Figures **xxi**

List of Tables **xxx**

Dedication **xxxi**

1 Introduction **1**

1.1 Structure of the thesis 5

2 Basics of Atom-Light Interactions **7**

2.1 Phenomena of atom-photon interactions 7

2.1.1 Semi-classical theory Electromagnetically Induced Transparency (EIT) 7

2.1.2 Electromagnetically Induced Transparency (EIT) and Autler-Townes splitting (ATS) in the dressed state picture 15
2.2 Rydberg atoms 17
2.2.1 Lifetime of Rydberg atoms 19
2.2.2 Interactions between Rydberg atoms 22
2.2.3 Rydberg Blockade 25
2.3 Conclusion 27

3 Absolute transition frequency measurement of high lying Rydberg states using Electromagnetically Induced Transparency 28
3.1 Experimental setup 29
3.2 Lock-in Detection 33
3.3 Results and discussion 34
3.4 Conclusion 36

4 Doppler-Enhanced Quantum-Magnetometry using Rydberg atoms at room-temperature 37
4.1 Interaction with external magnetic fields 38
4.1.1 Weak-field Zeeman effect of Hyperfine state 38
4.1.2 Strong-field Zeeman effect 39
4.1.3 Intermediate-field Zeeman effect 39
4.2 Experimental Setup 41
4.3 Theoretical Model 44
4.4 Results and Discussion 47
4.5 Conclusion 54

5 Experimental setup for cooling and trapping atoms 56
5.1 Trapping and cooling of ^{87}Rb atom 57
5.1.1 Principle of Magneto-Optical Trap (MOT) 57
5.1.2 Experimental setup of the MOT 59
5.1.3 Fluorescence Detection setup 64
5.1.4 Characterization of the MOT 65

5.1.5 Sub-Doppler cooling 68
5.2 Far-off resonance Dipole Trap 77
5.3 Conclusion 85

6 Probing of Rydberg interaction using Autler-Townes splitting 86
6.1 Experimental setup 87
6.2 Results and discussion 88
6.3 Summary 91

7 Rydberg-excitation mediated trap-loss spectroscopy 92
7.1 Experimental setup 93
7.1.1 Excitation laser 93
7.2 Results 99
7.2.1 Trap loss versus excitation time 100
7.2.2 Trap loss versus Rabi frequency 101
7.2.3 Trap loss versus detuning 103
7.2.4 Discussion and Summary 103

8 Summary and future Perspective 106
8.1 Summary 106
8.2 Future perspective 108

A Switching circuit for MOT coils 110
A.1 IGBT switching circuit 110

Appendix 110

B Cooling and Repumper SAS 112

C Simulation for other polarizations of probe and coupling laser 114
C.1 Parameter values used for measurements and numerical simulations . 115

List of Figures

1 a)Experimental setup for Doppler enhanced quantum magnetometry. b) Energy levels diagram for ^{87}Rb under magnetic field iv

2 Top: Showing experimental data of EIT signal with magnetic field (B) variation for $\{\sigma^-, \sigma^+\}$ polarization. a)co-propagating configuration b)counter-propagating configuration. Bottom:peak shift with magnetic field. solid line represents theoretical predictions. Magnetic field changed from 0 to 10 Gauss vi

3 Top: showing experimental data(left)and simulations data(right) with magnetic field . blue curve represents co-propagating EIT, green curve showing counter-propagating EIT. Bottom: relative peak splitting with magnetic field. solid line represents theoretical predictions . vii

4 a) EIT signal measured directly, locking the probe laser and scanning the coupling laser. b)lock-in amplifier detection by modulating the coupling laser with mechanical chopper. c)lock-in amplifier detection by modulating the frequency of probe laser. viii

5 a) schematic of MOT setup and two photon excitation lasers are shown. b)level diagram of MOT and two photon excitation scheme.It shows the excitation from $5S_{\frac{1}{2}}$ to $5P_{\frac{3}{2}}$ using 780 nm and excitation from $5P_{\frac{3}{2}}$ to $nS_{\frac{1}{2}}$ using 480 nm laser. c)This figure shows fluorescence imaging setup using APD and EMCCD camera. ix

6 a) showing fraction of atom loss vs different excitation time at three different effective Rabi frequencies b)fractional atom loss measured vs different detuning while keeping excitation time and effective Rabi frequency at 100 ms, 31 KHz respectively x

2.1 a) Lambda system b) V-system c) Ladder system; ω_p: probe laser; ω_c: coupling laser. 8

2.2 a) EIT due to the destructive quantum interference between transition pathways (1) and (2), it is explained in bare atomic state picture. b) EIT is explained in the dressed state basis. 16

2.3 ATS effect, left: probe and coupling lasers are shown, right: ATS effect explained in dressed state picture. 16

2.4 Rydberg atom 17

2.5 Probability density of electron $l = 0$ (blue line) and $l = 4$ (orange line), vertical line represents the core size. 18

2.6 Energy levels of ^{87}Rb, the value of principal quantum number (n) is varied from 6 to 80, and the l ranges from 0 to 5. 19

2.7 Transition rate from $30S_{\frac{1}{2}}$ to $n'P_{\frac{1}{2},\frac{3}{2}}$ states. Red-colored bars represent the transition rates due to the spontaneous emission and green-colored bars represent the transition rates due to the BBR. 21

2.8 Mechanism of resonant dipole-dipole interaction 23

2.9 Van der Waals interaction mechanism 24

2.10 Super atom model due to the Rydberg blockade. Red colored point represents the Rydberg atom and blue colored points represent the ground state atoms. 25

2.11 This figure shows the mechanism of Rydberg blockade. When the atom B is inside the blockade radius (R_B), the excited state ($|r\rangle$) of atom B undergoes a shift of $V_{vdw}(R) = \frac{C_6}{R_B^6}$. However at long distance $R >> R_B$, the shift is zero and both the atom can be simultaneously excited. 26

3.1 Vapor cell EIT setup used for the transition frequency measurements. 29

3.2 a) shows EIT signal by locking the probe laser and scanning the coupling laser. b) represents the lock-in signal measured by modulating the coupling beam, in this case probe laser is locked and coupling is scanned. c) shows the second harmonic of EIT signal measured by modulating the probe laser frequency, in this case probe laser is scanned and coupling laser is fixed near the resonance. 31

3.3 SAS signal and typical second harmonic of EIT signal recorded simultaneously. 32

3.4 a)Fine structure splittings of D-levels b) shows the lock-in signals of EIT for $46D, 55D$ and $88D$ levels. 35

4.1 Schematic diagram of the Experimental setup. The red colored beam represents the probe beam (780 nm). The blue colored beam (480 nm) represents the coupling beam. PBS: Polarising Beam Splitter; DM: Dichoric Mirror; HWP: Half Wave Plate; QWP: Quarter Wave Plate; M: Mirror 42

4.2 a) Shows the magnetic field variation along its axis. The same is measured at different coil currents. The origin (0 point in the graph) started from one side of the coil. b) it shows the average magnetic field vs the coil current (see text). 43

4.3 Doppler shift of an atom with velocity v with respect probe and coupling beam 44

4.4 a) Black line represents the imaginary part of zero-temperature susceptibility at $\Delta_c = 2MHz$ and $\sigma^+ - \sigma^-$ polarization, dotted curve shows the imaginary part of susceptibility without coupling beam, vertical line represents the two-photon resonance condition for zero-temperature, $\Delta_p = -\Delta_c$, where $\chi_{\text{ref}} = 2Nea_0/(\varepsilon_0\mathcal{E}_p) \approx 2 \times 10^{-4}$. b) Imaginary part of thermally averaged susceptibility $\bar{\chi} = \chi^{g,e} - \chi$, with $\Delta_c = -51$ MHz, vertical lines corresponding to the two-photon resonant condition, $\Delta_p = \mp\Delta^*$, where $\Delta^* = \frac{\omega_p}{\omega_c}\Delta_c$. c) Describes the zero temperature difference susceptibility $\bar{\chi}_0$, corresponding to a narrow EIT window, green (blue) line represents the thermal averaged counter-propagating (co-propagating) peak as $\Delta_p = \mp\Delta^*$. d) Contribution of different velocities to the susceptibility $\chi_0(v) := \chi_0(\Delta_p + \omega_p v/c, \Delta_c \mp \omega_c v/c)$, for $\Delta_c = -10$ MHz at $\Delta_p = \mp\Delta^*$ (solid lines) and at $\Delta_p = \mp\Delta^*/2$ 45

4.5 Measurements (left) and simulations (right) of the peak strength vs coupling laser power for $x - x$ polarizations. Green color curve represents the counter-propagating and blue color curve represents the co-propagating EIT. 47

4.6 Measurements (left) and simulation (right),green curve represents counter configuration EIT and blue curve represents co-propagation configuration EIT. 48

4.7 Energy-level diagram showing the ground manifold $\{5S_{1/2}, F = 2\}$, the excited manifold $\{5P_{3/2}, F' = 3\}$, and the Rydberg manifold $\{35S_{1/2}, I = 3/2\}$ of ^{87}Rb in the presence of a magnetic field. The red and blue arrows denote coherent pumping by the probe and coupling lasers, respectively, for $\sigma^{\pm}$ polarizations. The dashed lines represent incoherent decay of the excited states back to the ground manifold. . 50

4.8 Top: Measurements showing the variation of the EIT signal with B for σ^--σ^+ polarizations and $\Delta_c = -36$ MHz for (a) copropagating and (b) counter-propagating lasers. Vertical lines show the predicted peak locations at $\Delta_p(B)$ given by Eq. (4.17). Bottom: Displacement of the fitted peaks with B. Solid lines show theoretical predictions. . 52

4.9 Top: Measurements (left) and simulations (right) for increasing B with $\Delta_c = -36$ MHz and x-x polarizations. As before, green and blue curves stand for counter- and copropagating cases. Vertical lines show $\Delta_p(\pm B)$ from Eq. (4.19) 54

5.1 a) The Mechanism of the MOT shown for $F = 0$ and $F = 1$ total angular momentum states. The Zeeman splitting of the F levels is also shown. Two counter-propagated circular polarized laser beams of opposite helicity are used create a magnto-optical force for trapping atoms. b) showing the design of the MOT where the three pairs of counter-propagated beams with correct circular polarization are aligned so that they intersect at the center where magnetic field is zero. 58

5.2 Dodecagon vacuum chmaber with twelve view ports, high numerical aperture lens system built inside it. 59

5.3 Vacuum chamber used for our experiment 60

5.4 Energy level diagram of ^{87}Rb D2 line, $5S_{\frac{1}{2}}$: ground state, $5S_{\frac{3}{2}}$: excited state. 61

5.5 Cooling laser setup for the MOT. $\frac{\lambda}{2}$: HWP, $\frac{\lambda}{4}$: QWP, PBS: Polarizing Beam Splitter, M: mirror, BS: Beam Splitter, AOM: Acousto Optic Modulator, L: lens 62

5.6 Repump laser system for the MOT. $\frac{\lambda}{2}$: HWP, PBS: Polarizing Beam Splitter, BS: Beam Splitter, M: mirror, AOM : Acousto Optic Modulator. 63

5.7 Fluorescence imaging setup, L1: lens with focal length 15 cm, L2: lens with focal length 15 cm, L3: lens with focal length 7.5 cm. x,y represent the MOT cooling beams 64

5.8 Typical image of the atomic cloud in the MOT recorded with an EMCCD camera. The values along the x and y axes are pixel numbers of the EMCCD camera. 66
5.9 σ^2 vs τ^2 plot to determine the MOT atom cloud temperature. 68
5.10 Optical pumping in the presence of σ^+ polarized light 69
5.11 1) standing wave for linear parallel-parallel polarization, (see Eqn.(5.9)). 2) Polarization gradient for Sisyphus cooling, see(Eqn.(5.10)). 3) Standing wave for MASE cooling, see Eqn.(5.11). 4) Polarization gradient for corkscrew cooling mechanism, see Eqn.(5.12) 71
5.12 a) Zeeman sub-level structure of an atom with ground state $F_g = 1/2$ and excited state $F_e = 3/2$, coupling strength proportional to the square of the Clebsh-Gordon coefficient of that transition. b) Light shifts of ground states due to the polarization gradient. The polarization gradient is set as it is mentioned in 5.112). 72
5.13 Clebsh-Gordon coefficients and transition pathways for $J_g = 1$ and $J_e = 2$ 74
5.14 Time sequence of sub-Doppler cooling: the 'S' denotes that detuning reduced in one step, the 'R' denotes that the intensity is reduced step by step. In the 'S' stage, cooling intensity remains the same and in the 'R' stage cooling detuning remains the same. 76
5.15 Temperature of the atoms vs detuning $(-\delta/\Gamma)$ of the cooling beams during the sub-Doppler cooling phase. The detuning is changed in one step in the 'S' stage and is kept at the same value during the 'R' state. The detuning in the MOT loading phase is kept at -2Γ. 77
5.16 σ^2 vs τ^2 plot at sub-Doppler cooling stage. 78
5.17 a) light-shift for two level system b) 3D visualization of dipole potential. 79
5.18 Trap depth of the optical dipole trap as a function of the trapping laser power 80
5.19 Schematic of the setup for single atom trapping. L1 and L2: HNA lenses placed inside the vacuum chamber, DM: Dichroic mirror, M: Mirror, HWP: Half Wave Plate, PBS: Polarizing Beam Splitter, . . . 81

5.20 The red colored line shows the relative intensity noise of the dipole trap. The detector noise is represented by the blue colored line. . . . 83
5.21 lifetime as a function initial energy. Beam waist is kept at 2 μm. . . 84

6.1 a) Experimental setup used to probe the inter-atomic interaction between Rydberg atoms using trap-loss spectroscopy. b) Energy-level diagram for the measurement of Autler-Townes spectra. 87
6.2 Autler-Townes spectra of $\{35S_{\frac{1}{2}}\}$ Rydberg state, Ω' is generalized Rabi frequency. Y-scale defined as normalized atom number in the MOT. Two dips in Autler-Townes spectra corresponding to $|+\rangle$ and $|-\rangle$ dressed states. The generalized Rabi frequency is set around $\Omega' = 2\pi \times 21$ MHz. 88
6.3 a) Experimental measurements of the Autler-Townes splitting for various principal quantum numbers. b) Theoretically estimated Autler-Townes spectra for the same set of principal quantum numbers. . . . 89
6.4 Energy diagram for the Autler-Townes splitting of ^{87}Rb 90
6.5 (a) Linewidth of the red-detuned and blue-detuned peaks of the Autler-Townes spectra vs n. (b) Dephasing rate vs n, obtained by optimizing Binary Cross-Entropy loss function. 91

7.1 Schematic for frequency shifting of the 780 nm laser. HWP1, HWP2, HWP3: Half wave plate, QWP1: Quarter wave plate, AOM: Acousto Optic Modulator, PBS1, PBS2: Polarizing Beam Splitter, M1, M2, M3: mirror, SAS: Saturation Absorption Spectroscopy, L1 and L2: Lens 94
7.2 Schematic of the 480 nm laser utilized for frequency shifting and switching on/off of the laser. HWP1, HWP2, HWP3 : Half Wave Plate, QWP: Quarter Wave Plate. PBS1, PBS2, PBS3: Polarizing Beam Splitter. L1 and L1: lens with focal length 10 cm. AOM: Acousto Optic Modulator. 95
7.3 Two-photon excitation scheme, Δ_e is detuning of the laser from the transition to the intermediate state $\{5P_{\frac{3}{2}}, F' = 3\}$. 96

7.4 Schematic of the setup used for Rydberg excitation. For imaging setup: see chapter 2. L3: A-coated lens used for focusing the 480 nm laser. X,Y: MOT cooling beam (Z MOT beam is not shown in the figure.) 97
7.5 IGBT switching circuit 98
7.6 Time sequence of the Rydberg excitation using LabVIEW. 99
7.7 Fraction of atom loss vs excitation time. Excitation times are varied from 1 ms to 600 ms. a)effective Rabi frequency fixed at $2\pi \times 11.75$ kHz. b)Rabi frequency of $2\pi \times 20.36$ kHz. c)Rabi frequency of $2\pi \times 31.11$ kHz. The measurements are shown for $n = 48S$, $n = 68S$ and $n = 78S$ Rydberg states represented by the solid red-colored circles, the solid green-colored rectangles, and the solid green-colored triangles, respectively. 101
7.8 Fraction of trap loss at various Rabi frequencies. a) at excitation time of 100 ms. b)excitation time of 200 ms. c) at excitation time of 400 ms. The measurements for $n = 48$, $n = 68$ and $n = 78$ Rydberg states are represented by the solid red-colored circles, the solid green-colored rectangles, and the solid green-colored triangles, respectively. 102
7.9 Trap loss vs two photon detuning: the solid red-colored points represent the data for $48S$, the solid green-colored circles represent data for $68S$ state and the blue-colored triangles represent $78S$ state. . . . 103
7.10 Trap loss versus principal quantum number 'n' of the Rydberg state. The two-photon effective Rabi frequency is fixed at $2\pi \times 11.75$ kHz and excitation time is kept at 400 ms. 105

A.1 IGBT switching circuit 110

B.1 Cooling manifold of ^{87}Rb atom, dotted arrows are cross-over transitions. 112
B.2 Repump manifold of ^{87}Rb, dotted arrows are used to indicate cross-over transitions. 113

C.1 Steady-state difference susceptibility with $\Delta_c = -36$ MHz for σ^+-x (left) and x-σ^+ (right) polarizations. For σ^+-x the peak follows $\Delta_p(B)$ from Eq. (4.19). For x-σ^+ the dominant peak follows $\Delta_p(-B)$; the other line is obtained from Eq. (4.18) with $(m_F^g, m_F^e, m_J^r) = (-1, -2, 1/2)$ for counterpropagating (green) and $(0, 1, -1/2)$ for copropagating (blue) geometries. 115

C.2 Steady-state difference susceptibility with $\Delta_c = -36$ MHz for π-π (left) and π-x (right) polarizations. For both counterpropagating (green) and copropagating (blue) cases the vertical lines tracking the peaks are obtained from Eq. (4.18) with $(m_F^g, m_F^e, m_J^r) = (0, 0, \pm 1/2)$. 116

List of Tables

3.1 Values of the quantum defects. 36

4.1 weak-field Zeeman splitting of $|5S_{\frac{1}{2}}, F = 2\rangle$ 40

4.2 Weak-field Zeeman splitting of $|5P_{\frac{3}{2}}, F = 3\rangle$ per unit Gauss of magnetic field 41

4.3 Strong-field Zeeman effect of $35S_{\frac{1}{2}}$ state 41

C.1 Coupling laser power P_c used in different plots. 116

Dedication

Dedicated to my beloved parents, whose love and support have been my guiding light.

CHAPTER 1

Introduction

The advancement in atomic physics began after the invention of the laser in 1960s. A lot of technological development has happened since then. In present times, atomic physics is the front-runner for the development of the state-of-the-art technologies. With rising abilities to control many-body atomic systems and their internal states, it will be interesting to see what kind of breakthrough awaits us in the near future. Atomic physics has applications in a wide range of fields including time-keeping [26], GPS [27], quantum sensing [28, 29], quantum information [30–32], astrophysics [33] and many more.

Rydberg atoms [34] are one of the most important candidates in atomic physics that are pushing the boundaries in the development of cutting-edge quantum technologies [35]. It was first formulated by Johannes Rydberg in 1890 following the observation of hydrogen spectral line by Angstrom. Rydberg atoms are highly excited atoms with the outer electron excited to states with large principal quantum number. As the electrons are loosely bound to the nucleus, the Rydberg atom shows some unique properties like large size, high dipole moment ($\propto n^2$), strong dipole-dipole interactions ($\propto n^4$), large polarizability ($\alpha \propto n^7$) and long lifetime. Significant progress in the field of Rydberg physics started in 1970s and 1980s,

driven by the introduction of narrow linewidth lasers and innovative methods to cool and trap atoms. The current directions of research with Rydberg atoms are mainly catergorised into three areas: quantum computing, quantum sensing, quantum simulation of many-body physics and quantum optics.

The Rydberg states have long lifetimes and small transition probabilities to the ground state, which results in reducing the decay of optical photons from highly-excited Rydberg states. That is why atoms in Rydberg states are very difficult to detect by using direct fluorescence spectroscopy. However, the ionization threshold energy of Rydberg states decreases at higher Rydberg states, so it is easy to ionize the atoms in Rydberg states by static electric field. The electrons and ions created by field ionization can be detected by micro channel plates (MCP).

Another way of detecting Rydberg atoms is based on Electromagnetically Induced Transparency (EIT) [36], in the presence of a strong coupling beam, the previously optically opaque medium becomes transparent to the probe beam and a narrow peak of probe transmission is observed. The discovery of EIT has added a new dimension in the field of quantum sensing. As the polarizability of Rydberg atoms are very high, a feeble electric field can perturb the EIT signal significantly. EIT can be employed to detect AC, DC and RF electric fields [18]. Here, I will explain in simple ways how the EIT scheme can be used to detect electric fields. The EIT peak will be split into two Autler Towns (ATS) peaks in the presence of nearby resonant RF field, and the distance between the two peaks is equal to the Rabi frequency ($\Delta f = \frac{\hat{d}|E|}{\hbar}$) of the atomic transition due to the external RF field, $\hat{d}$ is dipole moment of the transition. From the peak separation Autler-Townes splitting signal, the amplitude of the RF field can be determined. This technique works for a wide range of frequencies from MHz to a few THz. The off-resonant fields like DC or low frequency AC fields cause shifts in the EIT peak positions, which is also called Stark effect. The field strength can be determined from the Stark shifts. If E is the electric field amplitude, then the Stark shift of the EIT signal peak due to the off-resonant field is $\Delta_f = -\frac{\alpha E^2}{2}$, α being the polarizability of the Rydberg state. The electric field can be generated by inserting two parallel plates inside a vapor cell [18] and connecting the plates to an AC or a DC power supply. If 'd' is

the distance between the two parallel plates then $E = -\frac{V}{d}$, V is the voltage. So the applied voltage can be determined from the Stark shift as both are related via the following equation, $V = d\sqrt{\frac{2\Delta_f}{\alpha}}$.

Another important application of Rydberg atoms is terahertz (THz) imaging [37–39]. The terahertz spectrum lies from wavelengths of 1 mm to 30 μm in the electromagnetic spectrum. The principle of terahertz imaging is to transfer the population from the ground state to a Rydberg state by using a laser and a THz field (two-photon Raman process) so that the atom emits optical fluorescence from the final Rydberg state. The photon emission rate is proportional to the intensity of the THz and the laser field. An EMCCD camera can be used to image the fluorescence from the atoms. The motivation behind terahertz imaging is that THz frequency can penetrate into non-metalic substance (plastic, cloth, etc.), so it can be used as an alternative to X-ray based imaging in airport security, crack detection, and many other similar applications.

All the methods I have explained above involve multiple photons. However, Rydberg atom-based sensors can detect even a single photon. Single-photon-level detection was pioneered by Serge Haroche who along with his team performed a quantum non-demolition measurement [40] to detect the single photon without destroying it. In this method, the Rydberg atom is prepared in a superposition of two Rydberg states (highly sensitive circular Rydberg states) by applying light pulses, then the atom passes through the cavity and interacts with the off-resonant photon, creating a shift in the energy levels. If the interaction time is τ and the energy shift of any state is δE, then the phase shift is $\delta E.\tau$. If there are more photons in the cavity then the energy shift will be more due to the off-resonant interaction, hence more phase shift will occur. Finally, the phase shift is measured by the Ramsey interferometer. In short, the photon numbers are determined by measuring the phase shift. Since no photons are absorbed or destroyed in the process, it is called a non-demolition measurement. For more detailed information about the measurement, please refer to [40]. For the ground-breaking work, Serge Haroche was awarded the Nobel prize in 2012.

Rydberg atoms are important candidates for quantum simulation and quan-

tum information processing. Quantum simulation [41] acts as a synthetic platform that mimics the simplest versions of the real-world complex systems. To perform quantum simulation, we need the control of individual atoms, their distances and interactions among them. For the last two decades, there have been a significant advancement in technology to trap single atoms in multiple arrays and optical lattices. The introduction of Digital mirror device (DMD) [42, 43] and spatial light Modulator (SLM) [44] has simplified the generation of multiple arrays and control of individual distances between them. Since the Rydberg atom has a large dipole moment, two types of strong inter-atomic interactions exist between Rydberg atoms: one is dipole-dipole interaction ($\frac{C_3}{R^3}$) and the other is Van der Waals interaction ($\frac{C_6}{R^6}$). Another important feature of Rydberg atom interaction is Rydberg blockade [8], it is an effect that is explained as the presence of a Rydberg atom prevents the Rydberg excitation of the second atom if it is within a certain distance from the Rydberg atom, called the 'Blockade radius'. By exciting the individually trapped atoms to the Rydberg states, different kinds of spin models, such as Ising spin [45], XY spin models [46] have been studied.

Qubits are the building blocks for quantum information processing and quantum computing. The superposition of atomic states is mapped as a qubit state. Trapping neutral atoms in optical tweezers and tuning Rydberg interactions, high-fidelity quantum gates have been achieved [47, 48].

In this thesis, I present the experiments performed on Rydberg atoms in vapor cell at room temperature as well as cold atoms in a magneto-optical trap. We use Rydberg Electromagnetically Induced Transparency (EIT) spectroscopy to measure the transition frequencies of high lying Rydberg states. We also perform Quantum Magnetometry using EIT spectroscopy of Rydberg atoms. The Autler-Townes Splitting (ATS) spectroscopy is used to measure the Van der Waals interaction mediated dephasing in cold Rydberg atoms. We also conduct Rydberg excitation by using two-photon excitation to study the losses of Rydberg atoms from the trap.

1.1 Structure of the thesis

I will outline here the flow of the thesis chapter by chapter:

- Chapter 2

  In this chapter, I describe the basics of atom-photon interactions that result in different coherent phenomena such as EIT and ATS. I also discuss the properties of Rydberg atoms and their different types of interactions.

- Chapter 3

  This chapter includes measurements conducted using EIT spectroscopy in the vapor cell to determine the transition frequencies of the highly excited Rydberg states for a wide range of principal quantum numbers.

- Chapter 4

  This chapter covers Doppler-Enhanced Quantum Magnetometry with Rydberg atoms. We measure the response of Rydberg EIT signal of a three-level ladder type system to an external magnetic field in a counter and co-propagating configuration. We find an enhanced response to the magnetic field in the co-propagating configuration. We explain our measurements using theoretical modelling and simulations based on Lindblad master equation.

- Chapter 5

  In this chapter, I have described our cold atom experimental setup and explained different cooling mechanisms to reduce the temperature of the atoms using Doppler as well as sub-Doppler cooling. I also describe the detection techniques for various measurements on cold atoms. I also explain the mechanism of trapping single atom in optical tweezers.

- Chapter 6

  In this chapter, we measure the effect of Rydberg interactions by using Autler-Townes splitting (ATS) spectroscopy in cold atoms.

- Chapter 7

This chapter covers the effects of Rydberg excitation in cold atoms. We measure the trap loss due to the Rydberg excitation in a cold atomic ensemble.

- Chapter 8 This chapter summarizes the experiments performed in the thesis and outlines the future plans and experiments to be performed with the current experimental setup.

CHAPTER 2

Basics of Atom-Light Interactions

This chapter describes the different processes emerging as a result of atom-photon interactions, dipole-dipole interactions to get a sense of the underlying physics of the experiments discussed in the later part of the thesis.

2.1 Phenomena of atom-photon interactions

The topic of atom-photon interaction encompasses a wide range of phenomena like spontaneous emission, stimulated emission, Electromagnetically Induced Transparency (EIT), Autler Townes Splitting (ATS), AC stark effect, Lamb shift etc. In this chapter, I will discuss only those phenomena involving atom-light interaction which are relevant to the experiments performed in this thesis.

2.1.1 Semi-classical theory Electromagnetically Induced Transparency (EIT)

Electromagnetically Induced transparency is a quantum interference phenomenon where a medium generally absorbent to a particular probe light, turns into an optically transparent medium upon the application of another strong light, called the

coupling laser. So minimum three levels of an atom are required to observe the EIT effect. Depending on the three-level structure, the EIT schemes are divided into three groups:

i) **Lambda scheme:** In this configuration, see Fig.2.1a), two energy levels are lower ($|1\rangle$, $|2\rangle$) and there is a third upper level ($|3\rangle$). A weak probe light is connected from one lower level to the upper level while the coupling light is associated with another lower level and the upper level as shown in Fig.2.1a).

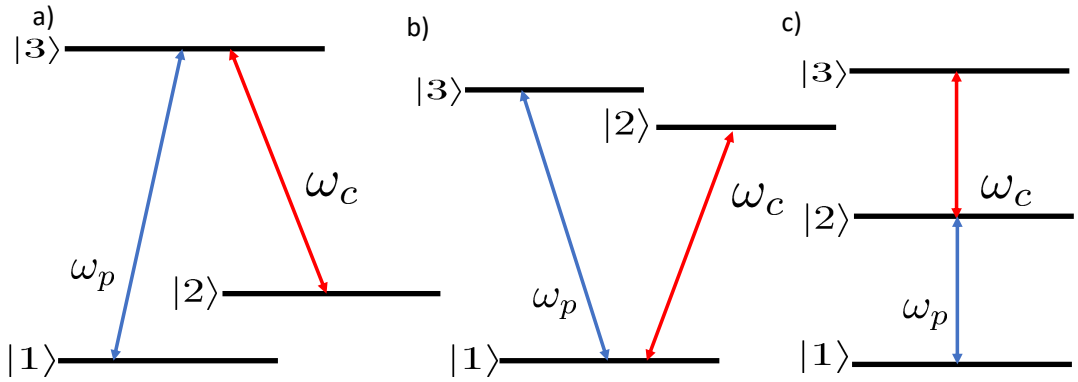


Figure 2.1: a) Lambda system b) V-system c) Ladder system; ω_p: probe laser; ω_c: coupling laser.

ii) **V-system scheme:** The V-system consists of two upper levels ($|2\rangle$, $|3\rangle$) and one ground level ($|1\rangle$). The configuration of the weak probe beam and the strong coupling beam is shown in the Fig.2.1b).

iii) **Cascade or Ladder system:** In this configuration, the three energy levels are sequenced in a ladder-style configuration (see Fig.2.1c)). The probe laser makes the transition from the ground state ($|1\rangle$) to the intermediate state ($|2\rangle$) and the coupling laser couples from the intermediate to the excited state ($|3\rangle$). In this chapter, I will discuss the semi-classical theory of the ladder-type system as our experiments are based on Rydberg EIT in a three-level ladder-type atomic system.

Semi-classical approach: We follow Lindblad Master equation [49] to obtain the expression for complex susceptibility at EIT condition, the density matrix equation for driven-dissipative system is given as,

$$\frac{d\rho_0}{dt} = -\frac{i}{\hbar}[H, \rho_0] + \sum_k \gamma_k (L_k \rho_0 L_k^\dagger - \frac{1}{2}\{L_k^\dagger L_k, \rho_0\}) \tag{2.1}$$

ρ_0 is the density matrix, L_k is the projection operator ($|i\rangle\langle j|$) describing the transition from $|j\rangle$ to $|i\rangle$, γ_k is the decay rate, k denotes all the decay channels. The atomic Hamiltonian for the three-level bare states is given by:

$H_A = \hbar\omega_1|1\rangle\langle 1| + \hbar\omega_2|2\rangle\langle 2| + \hbar\omega_3|3\rangle\langle 3|$

The interaction of the atom with light is treated semi-classically, so the interaction Hamiltonian is, H_I = **-d.E**, d is the dipole moment, E is the electric field.

$$H_I = \sum_{m,n=1,2,3} |n\rangle\langle n|d.E|m\rangle\langle m| = d_{nm}E_{nm}|n\rangle\langle m| \tag{2.2}$$

E_{nm} is the electric field conecting $|n\rangle$ and $|m\rangle$ states.

The probe electric field is given by $E_{12} = E_{21} = E_p cos(\omega_p t)$ and the coupling electric field $E_{23} = E_{32} = E_c cos(\omega_c t)$. Putting these electric field values in *Eqn.* (2.2), the interaction Hamiltonian can be written as,

$$H_I = \frac{\hbar\Omega_{12}}{2}(e^{i\omega_p t} + e^{-i\omega_p t})|1\rangle\langle 2| + c.c + \frac{\hbar\Omega_{23}}{2}(e^{i\omega_c t} + e^{-i\omega_c t})|2\rangle\langle 3| + c.c \tag{2.3}$$

$\mathbf{\Omega_{12}} = \frac{\mathbf{d_{12}Ep}}{\hbar}$ is the probe Rabi frequency and $\mathbf{\Omega_{23}} = \frac{\mathbf{d_{23}E_c}}{\hbar}$ is the coupling Rabi frequency. Hence, the total Hamiltonian is given by:

$$H = H_A + H_I \tag{2.4}$$

Since the Hamiltonian (H) is time-dependent, it is difficult to solve. This Hamiltonian is also called the Lab frame Hamiltonian. I label this Hamiltonian as $H_{Lab} = H$. To extract the time-averaged dynamics of this interaction Hamiltonian, a co-rotational transformation has to be done with transformation $U = e^{-i\omega_p t|2\rangle\langle 2| - i(\omega_p+\omega_c)t|3\rangle\langle 3|}$.

So the Hamiltonian in the rotational frame is given by

$$H_{rot} = i\hbar\frac{\partial U}{\partial t}U^{\dagger} + UH_{Lab}U^{\dagger} \tag{2.5}$$

Here are the basic tools used for doing co-rotational transformation,

$$e^{i\omega t|e\rangle\langle e|} = \sum_{n=0}^{\infty}(i\omega t|e\rangle\langle e|)^n = \mathbf{I} + (e^{i\omega t} - 1)|e\rangle\langle e| \tag{2.6}$$

so,

$$e^{i\omega t|e\rangle\langle e|}|e\rangle = e^{i\omega t}|e\rangle \tag{2.7}$$

and

$$e^{i\omega t|e\rangle\langle e|}|g\rangle = |g\rangle \tag{2.8}$$

Using Baker-Campbell-Hausdorff formula, $U = e^{-i\omega_p t|2\rangle\langle 2| - i(\omega_p+\omega_c)t|3\rangle\langle 3|}$ can be written as,

$$U = e^{-i\omega_p t|2\rangle\langle 2|}e^{-i(\omega_p+\omega_c)t|3\rangle\langle 3|} \tag{2.9}$$

Let us consider the "$UH_{Lab}U^{\dagger}$" part of $Eqn.2.5$. The diagonal elements are obtained using $Eqn.$ 2.6-2.9 as:

$$U\hbar\omega_1|1\rangle\langle 1|U^{\dagger} = \hbar\omega_1|1\rangle\langle 1|, U\hbar\omega_2|2\rangle\langle 2|U^{\dagger} = \hbar\omega_2|2\rangle\langle 2|, U\hbar\omega_3|3\rangle\langle 3|U^{\dagger} = \hbar\omega_3|3\rangle\langle 3| \tag{2.10}$$

Off-diagonal terms or interaction part of $UH_{Lab}U^{\dagger}$ (using $Eqn.$ 2.6-2.9):

$U\frac{\hbar\Omega_{12}}{2}(e^{i\omega_p t} + e^{-i\omega_p t})|1\rangle\langle 2|U^{\dagger}$

$= e^{i\omega_p t|2\rangle\langle 2|}e^{i(\omega_p+\omega_c)t|3\rangle\langle 3|}\frac{\hbar\Omega_{12}}{2}(e^{i\omega_p t} + e^{-i\omega_c t})|1\rangle\langle 2|e^{-i\omega_p t|2\rangle\langle 2|}e^{-i(\omega_p+\omega_c)t|3\rangle\langle 3|}$

$= \frac{\hbar\Omega_{12}}{2}(1 + e^{-i2\omega_p t})|1\rangle\langle 2|$, $2\omega_p$ term is neglected using rotating wave approximation.

$$U\frac{\hbar\Omega_{12}}{2}(e^{i\omega_p t} + e^{-i\omega_p t})|1\rangle\langle 2|U^{\dagger} = \frac{\hbar\Omega_{12}}{2}|1\rangle\langle 2| \tag{2.11}$$

Similarly,

$$U\frac{\hbar\Omega_{23}}{2}(e^{i\omega_c t} + e^{-i\omega_c t})|2\rangle\langle 3|U^{\dagger} = \frac{\hbar\Omega_{23}}{2}|2\rangle\langle 3| \tag{2.12}$$

So, from *Eqn.* 2.10, 2.11, 2.12,

$$UH_{Lab}U^{\dagger} = \hbar\omega_1|1\rangle\langle 1| + \hbar\omega_2|2\rangle\langle 2| + \hbar\omega_3|3\rangle\langle 3| + \frac{\hbar\Omega_{12}}{2}|1\rangle\langle 2| + \frac{\hbar\Omega_{21}}{2}|2\rangle\langle 1| + \frac{\hbar\Omega_{23}}{2}|2\rangle\langle 3| + \frac{\hbar\Omega_{32}}{2}|3\rangle\langle 2| \quad (2.13)$$

From *Eqn.*2.5

$$i\hbar\frac{\partial U}{\partial t}U^{\dagger} = -\hbar\omega_p|2\rangle\langle 2| - \hbar(\omega_p + \omega_c)|3\rangle\langle 3| \quad (2.14)$$

Combining the *Eqn.* 2.13 and *Eqn.* 2.14,

$$H_{rot} = \hbar\omega_1|1\rangle\langle 1| - (\omega_p - \omega_2)|2\rangle\langle 2| - \hbar(\omega_p + \omega_c - \omega_3)|3\rangle\langle 3| + \frac{\hbar\Omega_{12}}{2}|1\rangle\langle 2| + \frac{\hbar\Omega_{21}}{2}|2\rangle\langle 1| + \frac{\hbar\Omega_{23}}{2}|2\rangle\langle 3| + \frac{\hbar\Omega_{32}}{2}|3\rangle\langle 2| \quad (2.15)$$

If we shift the atomic energy scale to $\hbar\omega_1\mathbf{I}$, the new Hamiltonian can be written as $\tilde{H} = H_{rot} - \hbar\omega_1\mathbf{I}$.

$$\tilde{H} = -\Delta_p|2\rangle\langle 2| - (\Delta_p + \Delta_c)|3\rangle\langle 3| + \frac{\Omega_p}{2}|1\rangle\langle 2| + \frac{\Omega_p}{2}|2\rangle\langle 1| + \frac{\Omega_c}{2}|2\rangle\langle 3| + \frac{\Omega_c}{2}|3\rangle\langle 2| \quad (2.16)$$

Here, the probe Rabi frequency is Ω_{12}=Ω_{21}=Ω_p and
the coupling Rabi frequency is Ω_{23}=Ω_{32}=Ω_c. $\hbar$ is omitted as it will be canceled in Linblad equation 2.1.

Decay matrices: For three-level ladder type system, there exist two channels, one from the excited state ($|3\rangle$) with decay rate γ_3 and other from the intermediate state ($|2\rangle$) with decay rate γ_2.

From *Eqn.* 2.1, the decay part for k=3 and k=2 is given as follows:

For excited state:

k=3, represents the decay channel of the excited state. $\gamma_3(|2\rangle\langle 3|\tilde{\rho}|3\rangle\langle 2| - \frac{1}{2}\{|3\rangle\langle 2|2\rangle|\langle 3|, \tilde{\rho}\})$

$$= \gamma_3\{\tilde{\rho}_{33}|2\rangle\langle 2| - \frac{1}{2}(\tilde{\rho}_{31}|3\rangle\langle 1| + \tilde{\rho}_{13}|1\rangle\langle 3| + \tilde{\rho}_{32}|3\rangle\langle 2| + \tilde{\rho}_{23}|2\rangle\langle 3| + 2\tilde{\rho}_{33}|3\rangle\langle 3|)\} \quad (2.17)$$

For intermediate state:

k=2, represents the decay channel from the intermediate state. $\gamma_2(|1\rangle\langle 2|\tilde{\rho}|2\rangle\langle 1| - \frac{1}{2}\{|2\rangle\langle 1|1\rangle 2|, \tilde{\rho}\})$

$$= \gamma_3\tilde{\rho}_{33}|2\rangle\langle 2| - \frac{\gamma_2}{2}\tilde{\rho}_{12}|1\rangle\langle 2| - \frac{(\gamma_3\tilde{\rho}_{32} + \gamma_2\tilde{\rho}_{32})}{2}|3\rangle\langle 2| - \frac{(\gamma_2\tilde{\rho}_{23} + \gamma_3\tilde{\rho}_{23})}{2}|2\rangle\langle 3| \quad (2.18)$$

$\tilde{\rho}_{ij}$ is the density matrix in the rotational frame. Since the ground state is a highly metastable state, the decay from the ground state $\gamma_1 = 0$.

Decay matrix from *Eqn.* 2.17and 2.18 is given as,

$$L_{decay}(\tilde{\rho}) = \begin{bmatrix} \gamma_2\tilde{\rho}_{22} & -\frac{\gamma_2}{2}\tilde{\rho}_{12} & -\frac{\gamma_3}{2}\tilde{\rho}_{13} \\ -\frac{\gamma_2}{2}\tilde{\rho}_{21} & \gamma_3\tilde{\rho}_{33} - \gamma_2\tilde{\rho}_{22} & -\frac{\gamma_2+\gamma_3}{2}\tilde{\rho}_{23} \\ \frac{\gamma_3}{2}\tilde{\rho}_{31} & -\frac{(\gamma_3+\gamma_2)}{2}\tilde{\rho}_{32} & -\gamma_3\tilde{\rho}_{33} \end{bmatrix}$$

From *Eqn.*2.16, the time-independent Hamiltonian matrix is given as,

$$\tilde{H} = \frac{1}{2}\begin{bmatrix} 0 & \Omega_p & 0 \\ \Omega_p & -2\Delta_p & \Omega_c \\ 0 & \Omega_c & -2(\Delta_p + \Delta_c) \\ \end{bmatrix} \quad (2.19)$$

The Lindblad equation from 2.1 is written as,

$$\frac{\partial\tilde{\rho}}{\partial t} = -i[\tilde{H}, \tilde{\rho}] + L_{decay}(\tilde{\rho}) \quad (2.20)$$

where, $\tilde{\rho} = \begin{bmatrix} \tilde{\rho}_{11} & \tilde{\rho}_{12} & \tilde{\rho}_{13} \\ \tilde{\rho}_{21} & \tilde{\rho}_{22} & \tilde{\rho}_{23} \\ \tilde{\rho}_{31} & \tilde{\rho}_{32} & \tilde{\rho}_{33} \end{bmatrix}$

The Lindblad equation 2.20 can be solved numerically or analytically.

Analytical solution:

Weak probe approximation is used to solve the *Eqn.* 2.20 analytically. In this approach, it is assumed that $\Omega_p \ll \Omega_c$, so $\tilde{\rho}_{11} \approx 1$, $\tilde{\rho}_{22} \approx 0$ and $\tilde{\rho}_{33} \approx 0$.

By taking the individual terms from the *Eqn.* 2.1, we get the following coupled equations:

$$\frac{\partial\tilde{\rho}_{21}}{\partial t} = \frac{\partial\tilde{\rho}^*_{12}}{\partial t} = -(\gamma_{21} - i\Delta_p)\tilde{\rho}_{21} + i\frac{\Omega_p}{2}(\tilde{\rho}_{22} - \tilde{\rho}_{11}) - i\frac{\Omega_c}{2}\tilde{\rho}_{31} \tag{2.21}$$

$$\frac{\partial\tilde{\rho}_{31}}{\partial t} = \frac{\partial\tilde{\rho}^*_{13}}{\partial t} = -\{\gamma_{31} - i(\Delta_p + \Delta_c)\}\tilde{\rho}_{31} - i\frac{\Omega_c}{2}\tilde{\rho}_{21} + i\frac{\Omega_p}{2}\tilde{\rho}_{32} \tag{2.22}$$

$$\frac{\partial\tilde{\rho}_{32}}{\partial t} = \frac{\partial\tilde{\rho}^*_{23}}{\partial t} = -(\gamma_{32} - i\Delta_c)\tilde{\rho}_{32} + i\frac{\Omega_c}{2}(\tilde{\rho}_{33} - \tilde{\rho}_{22}) + i\frac{\Omega_p}{2}\tilde{\rho}_{31} \tag{2.23}$$

$$\frac{\partial\tilde{\rho}_{11}}{\partial t} = \gamma_2\tilde{\rho}_{22} - i\frac{\Omega_p}{2}(\tilde{\rho}_{21} - \tilde{\rho}_{12}) \tag{2.24}$$

$$\frac{\partial\tilde{\rho}_{22}}{\partial t} = \gamma_3\tilde{\rho}_{33} - \gamma_2\tilde{\rho}_{22} - i\frac{\Omega_p}{2}(\tilde{\rho}_{12} - \tilde{\rho}_{21}) - i\frac{\Omega_c}{2}(\tilde{\rho}_{32} - \tilde{\rho}_{23}) \tag{2.25}$$

$$\frac{\partial\tilde{\rho}_{33}}{\partial t} = -i\frac{\Omega_c}{2}(\tilde{\rho}_{23} - \tilde{\rho}_{32}) - \gamma_3\tilde{\rho}_{33} \tag{2.26}$$

Where, $\gamma_{ij} = \frac{\gamma_i+\gamma_j}{2}$. Now, according to the weak-probe approximation, $\tilde{\rho}_{11} \approx 1$, $\tilde{\rho}_{22} \approx 0$, $\tilde{\rho}_{33} \approx 0$.

So, in the steady state [50], the *Eqn.* (2.23) becomes:

$$\tilde{\rho}_{32} \approx i\frac{\Omega_p}{2(\gamma_{32} - i\Delta_c)}\tilde{\rho}_{31} \tag{2.27}$$

Since the $\tilde{\rho}_{32}$ term is $\propto \Omega_p$, so the $\tilde{\rho}_{32}$ term in equation2.22 will be neglected. The equation 2.21 and 2.22 can be written as,

$$\frac{\partial\tilde{\rho}_{21}}{\partial t} = -(\gamma_{21} - i\Delta_p)\tilde{\rho}_{21} - i\frac{\Omega_p}{2} - i\frac{\Omega_c}{2}\tilde{\rho}_{31} \tag{2.28}$$

$$\frac{\tilde{\rho}_{31}}{\partial t} = -(\gamma_{31} - i(\Delta_p + \Delta_c))\tilde{\rho}_{31} - i\frac{\Omega_c}{2}\tilde{\rho}_{21} \tag{2.29}$$

So *Eqn.* 2.28 and 2.29 is a system of coupled equations and can be written as, $\dot{y} = Mx + c$ and it could be solved as $x = -M^{-1}c$ in the steady state, M^{-1} is the inverse of the M matrix. The solution of *Eqns.*2.28 and 2.29 is,

$$\tilde{\rho}_{21} = -\frac{\frac{i\Omega_p}{2}}{(\gamma_{21} - i\Delta_p) + \frac{\frac{\Omega_c^2}{4}}{(\gamma_{31} - i(\Delta_p + \Delta_c))}}. \tag{2.30}$$

$$\tilde{\rho}_{31} = -\frac{\frac{\Omega_c\Omega_P}{4}}{(\gamma_{21} - i\Delta_p)(\gamma_{31} - i(\Delta_p + \Delta_c)) + \frac{\Omega_c^2}{4}}. \tag{2.31}$$

Since the above solution is time-independent as it is in the co-rotational frame, after reverse transformation of $\rho = U^{\dagger}\tilde{\rho}U$, the coherence will be oscillating with the laser frequency.

Analytical form of the susceptibility:

If P is the macroscopic dipole moment per unit volume, then $P = N < p >$, N is the number of atoms per unit volume and $< p >$ is the average dipole moment for a single atom.

$$P = N < p >= NTr(\rho \mathbf{d}) = N(\tilde{\rho}_{12}d_{21} + \tilde{\rho}_{21}d_{12} + \tilde{\rho}_{23}d_{32} + \tilde{\rho}_{32}d_{23}) \tag{2.32}$$

if χ is the susceptibility of the probe light (ω_p), then

$$P = \epsilon_0 \chi E \tag{2.33}$$

where E = $E_p cos(\omega_p t)$

From *Eqn.* 2.32, 2.33 and 2.30, the expression of complex susceptibility for the probe light is evaluated as,

$$\chi_0(\omega_p) = \frac{2N|d_{21}|^2}{\epsilon_0 \hbar \Omega_p}\tilde{\rho}_{12} \tag{2.34}$$

$$= \frac{2N|d_{21}|^2}{\epsilon_0 \hbar \Omega_p} \frac{\frac{i\Omega_p}{2}}{(\gamma_{21} + i\Delta_p) + \frac{\frac{\Omega_c^2}{4}}{(\gamma_{31} + i(\Delta_p + \Delta_c)}} \tag{2.35}$$

Imaginary part of the susceptibility:

The imaginary part of equation 2.35 gives the absorption properties of the medium. EIT will happen at the two-photon resonance condition, so $\Delta_p + \Delta_c = 0$. The *Eqn.* 2.35 becomes,

$$\chi_0(\omega_p) = \frac{2N|d_{21}|^2}{\epsilon_0 \hbar \Omega_p} \frac{\frac{i\Omega_p}{2}}{(\gamma_{21} + i\Delta_p + \frac{\Omega_c^2}{4\gamma_{31}})} \tag{2.36}$$

Imaginary part of the susceptibility is expressed as,

$$Im(\chi_0(\omega_p)) = \frac{N|d_{21}|^2}{\epsilon_0 \hbar \Omega_p} \frac{\gamma_{EIT}\Omega_p}{(\Delta_p^2 + \gamma_{EIT}^2)} \tag{2.37}$$

$$\gamma_{EIT} = \gamma_{21} + \frac{\Omega_c^2}{4\gamma_{31}} \tag{2.38}$$

2.1.2 Electromagnetically Induced Transparency (EIT) and Autler-Townes splitting (ATS) in the dressed state picture

In this section, I will discuss EIT [51,52] and ATS effects in an intuitive way while the last section is devoted to describing EIT in a mathematical basis. EIT occurs due to the destructive quantum interference between the transition pathways between two states. In a bare state picture for three-level ladder-type system, the two possible transition pathways that destructively interfere are $|1\rangle \rightarrow |2\rangle$ and $|1\rangle \rightarrow |2\rangle \rightarrow |3\rangle \rightarrow |2\rangle$, as shown in Fig.2.2a).

The phenomenon of EIT is best understood in the dressed-state picture: the eigenstates of the time-independent Hamiltonian (*Eqn.* 2.19) are the dressed states and they are basically the linear superposition of the bare atomic states. The eigenvalues and eigenstates of the Hamiltonian (*Eqn.* 2.19) can be calculated analytically. At two-photon resonance, $\Delta_p + \Delta_c = 0$, the eigenvalues are 0 and $\frac{-\Delta_p \pm \sqrt{\Delta_p^2 + \Omega_c^2 + \Omega_p^2}}{2}$, and the corresponding eigenstates are $|0\rangle$ and $|\pm\rangle$ respectively. Using the weak-probe approximation, $\Omega_p << \Omega_c$, the eigenstates become $|0\rangle = |1\rangle$ and $|\pm\rangle = \frac{|3\rangle \pm |2\rangle}{\sqrt{2}}$. The $|0\rangle$ state is called the 'dark state' as it has zero eigenvalue. For weak-probe approximation the dark state is basically the ground state.

In the dressed state picture, the transition pathways will be $|0\rangle \rightarrow |+\rangle$ and $|0\rangle \rightarrow |-\rangle$, and the amplitudes of transition probability will destructively interfere only if the separation between the two dressed states ($|\pm\rangle$) is less than the line-widths of the dressed states, as shown in Fig.2.2b). So the total transition probability amplitude is $\langle 0|\hat{d}|+\rangle + \langle 0|\hat{d}|-\rangle = 0$, $\hat{d}$ is the dipole operator.

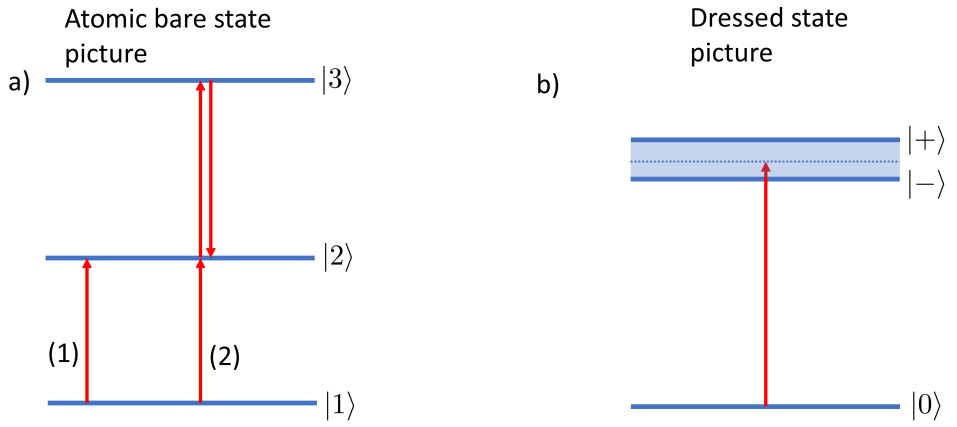


Figure 2.2: a) EIT due to the destructive quantum interference between transition pathways (1) and (2), it is explained in bare atomic state picture. b) EIT is explained in the dressed state basis.

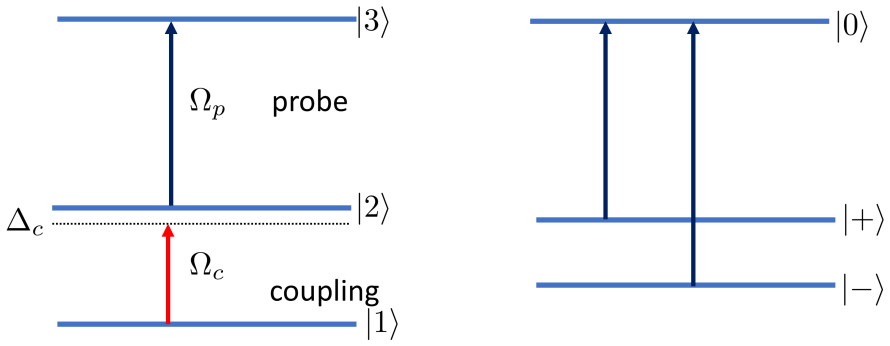


Figure 2.3: ATS effect, left: probe and coupling lasers are shown, right: ATS effect explained in dressed state picture.

ATS is another coherent phenomenon that is observed under the strong coupling regime, $\Omega_c >> \gamma_2$, γ_2 is the decay rate from the intermediate state for the three-level ladder-type atomic system. Let us consider again three-level ladder system but this time the coupling laser is used for the $|1\rangle \rightarrow |2\rangle$ transition and the weak probe laser is tuned to the $|2\rangle \rightarrow |3\rangle$ transition. In the strong coupling regime, $\Omega_c >> \gamma_2$ and weak probe approximation $\Omega_c >> \Omega_p$, the separation between the two dressed states ($|\pm\rangle$) is caused by the AC stark effect and it is expressed as $\sqrt{\Omega_c^2 + \Delta_c^2}$. Under the weak probe approximation, dressed states are $|\pm\rangle = \frac{|1\rangle \pm |2\rangle}{\sqrt{2}}$ and $|0\rangle = |3\rangle$, see Fig.2.3. Since the dressed state spacing is more than their widths, the doublet structure of ATS can be observed while scanning the probe laser.

2.2 Rydberg atoms

Rydberg atoms [34] (Fig.2.4) are highly excited atoms where one electron is excited to states with high principal quantum number ($n \gg 10$). Rydberg atoms were first discovered [53] by Johanes R. Rydberg in 1890. The first quantum theoretical description of atomic energy levels emerged from Bohr's atomic model (1911) of the Hydrogen atom, where energy of each level is described as

$$E_n = -\frac{R_y}{n^2} \tag{2.39}$$

R_y is the reduced mass corrected Rydberg constant and it is given as $R_y = \frac{R_\infty M}{M+m_e}$, where $R_\infty = \frac{m_e e^4}{16\pi^2\epsilon_0^2\hbar^2}$, m_e is the mass of the electron, M is atomic mass of nucleus and 'n' is the principal quantum number. However, the *Eqn.* 2.39 is specifically applied to the Hydrogen atom (Z=1).

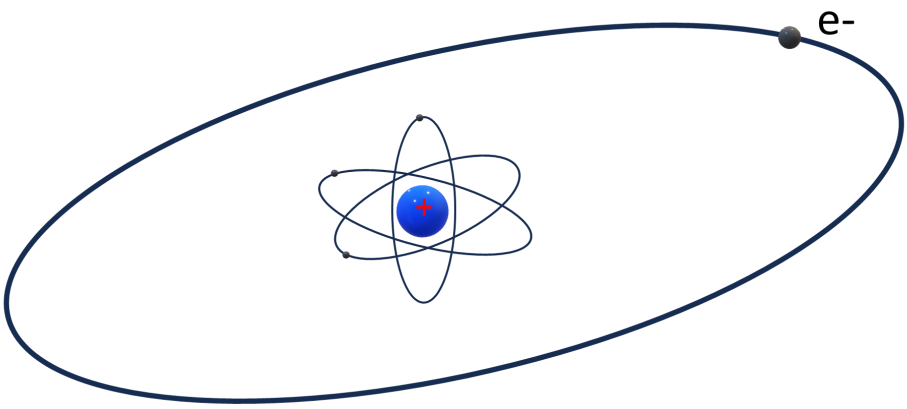


Figure 2.4: Rydberg atom

For the Hydrogen like system (^{87}Rb, $Z > 1$) where one valence electron is outside the core region (see Fig.2.4), the *Eqn.* 2.39 needs modification as electrons with orbital angular momentum quantum number $l \leq 3$ penetrate and polarize the Rb core giving rise to an effect called quantum defect [54,55]. In Fig. 2.5, the probability density of electrons for the orbital angular momentum quantum numbers $l = 0$ and $l = 4$ (for $n = 20$) is shown. The probability density of electrons for $l = 0$ state

inside the core region is more than that of $l = 4$ state. As a result of interactions with the core, the energy of the low orbital states ($l \leq 3$) is depressed compared to the energy of the same orbital angular momentum quantum number in Hydrogen atom. So the modified binding energy for Hydrogen-like atom is given as,

$$E_{nlj} = -\frac{R_y}{(n - \delta_{nlj})^2} \tag{2.40}$$

j is the total angular momentum and δ_{nlj} is the quantum defect. The quantum defect of any $|n, l, j\rangle$ state is parametrized as,

$$\delta_{nlj} = \delta_0 + \frac{\delta_2}{(n - \delta_0)^2} + \frac{\delta_4}{(n - \delta_0)^2} + \dots \tag{2.41}$$

The above equation is often called the Rydberg-Ritz formula. For higher 'n', the first two terms are enough to calculate the energy.

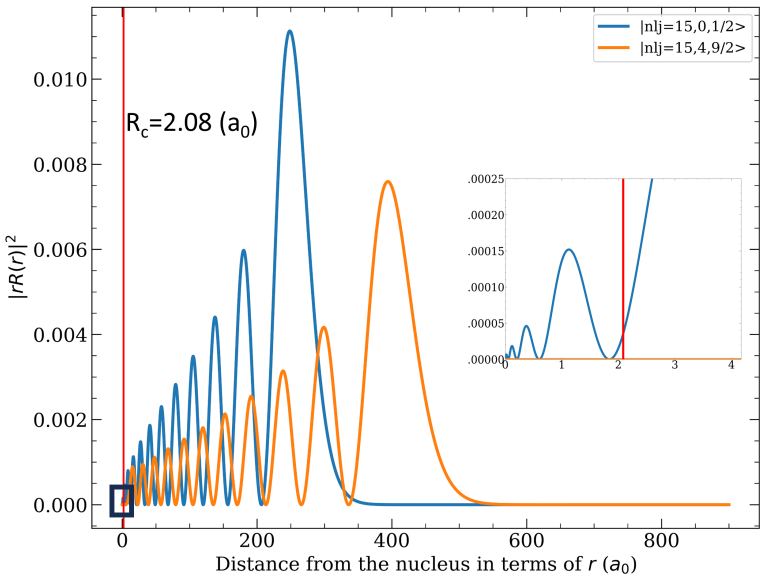


Figure 2.5: Probability density of electron $l = 0$ (blue line) and $l = 4$ (orange line), vertical line represents the core size.

Fig.2.6 illustrates the energy levels of ^{87}Rb atom with orbital quantum numbers from $l = 0$ to 5. The principal quantum number 'n' is varied from 6 to 80. It is evident that for $l > 3$, the effect of quantum defects is negligible, so the energies of the $l = 4$ and $l = 5$ states are almost identical. Since the electron in the Rydberg atom is located at far distance from the core, it is loosely bound to the nucleus. Due

to this, the Rydberg atom exhibits exaggerated properties such as high polarizability [56], a large dipole moment [57, 58], strong dipole-dipole interaction [59, 60], and extended lifetime [61]. Some important advantages of atom-based sensors are their stability and self-calibrating capabilities which means it doesn't require any external calibration. The properties of the atoms will be the same irrespective of the place and time. Due to their high polarizability, Rydberg atoms are highly responsive to weak external electric fields, making them excellent candidates for quantum sensing and high precision measurements [29, 62–74].

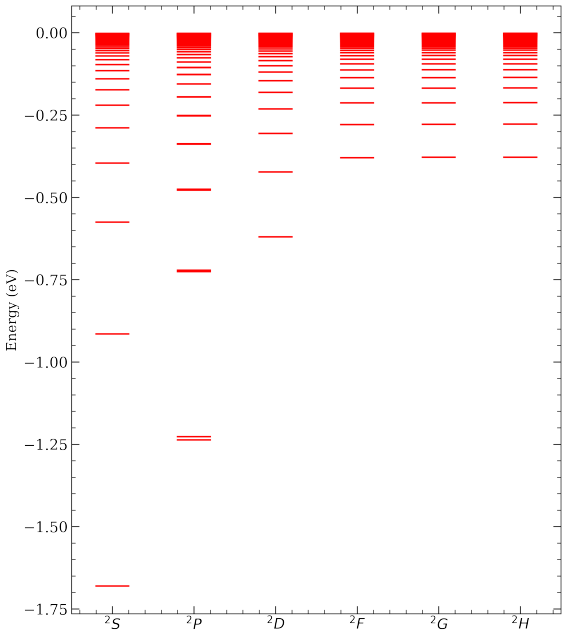


Figure 2.6: Energy levels of ^{87}Rb, the value of principal quantum number (n) is varied from 6 to 80, and the l ranges from 0 to 5.

2.2.1 Lifetime of Rydberg atoms

One of the important properties of the Rydberg atoms is that it has longer lifetime than that of the ground states. The main contributions to the lifetime come from the two types of decay processes: one is spontaneous decay and the other is Black-Body Radiation (BBR) induced depopulation. The spontaneous decay rate between nL and $n'L'$ states can be estimated using the Einstein $A(nL \rightarrow n'L')$ coefficient,

which is given as,

$$A(nL \rightarrow n'L') = \frac{4\omega_{nn'}^3 L_{max}}{3c^3(2L+1)} R^2(nL \rightarrow n'L'). \tag{2.42}$$

Where $\omega_{nn'}$ is the angular transition frequency between nL and $n'L'$ states, L_{max} is the maximum value of L and L', $R(nL \rightarrow n'L')$ is the radial component of transition dipole matrix, c is the velocity of light. So the total decay to all $n'L'$ states due to the spontaneous emission is written as,

$$\Gamma_{spon} = \sum_{n'L'} A(nL \rightarrow n'L'). \tag{2.43}$$

From *Eqn.* 2.42, it is clear that the spontaneous decay rate depends on the two factors: one is the transition frequency between the states where the decay is occurring and the other is the transition dipole matrix. As the 'n' increases, the overlap between the ground state and the Rydberg state decreases, making the relative decay to the ground states weaker. However, one would think that since the transition matrix element between the adjacent Rydberg states is $\propto n^2$, the decay to the closer Rydberg states might be strong but that is not the case as the number of vacuum modes causing spontaneous decay in the terahertz and microwave regions reduces fast.

The BBR-induced depopulation rate depends on the average number of photons per mode at temperature 'T'. The average number of photons for BBR radiation is given as,

$$\overline{n_w} = \frac{1}{e^{\frac{\hbar\omega_{nn'}}{k_B T}} - 1}. \tag{2.44}$$

So the total depopulation rate from nL state to other $n'L'$ states is written as,

$$\Gamma_{BBR} = \sum_{n'L'} A(nL \rightarrow n'L')\overline{n_\omega}. \tag{2.45}$$

The decay due to the spontaneous transition mostly populates the ground or lower excited states, so the effective contribution of n' will be around the ground or lower excited states. However, the BBR-induced depopulation can populate lower

or higher excited Rydberg states, significant contribution comes from $n' = n \pm 1$ states. Fig.2.7 shows the transition rate from $30S_{\frac{1}{2}}$ to $n'P_{\frac{1}{2}}$ and $n'P_{\frac{3}{2}}$ states due to spontaneous emission and BBR-induced depopulation, it is clear from the figure that the transition rate due to spontaneous emission is high in lower excited states ($5P_{\frac{1}{2},\frac{3}{2}}$, $6P_{\frac{1}{2},\frac{3}{2}}$, $7P_{\frac{1}{2},\frac{3}{2}}$), but the transition rate due to BBR is high in nearby Rydberg states which are $29P_{\frac{1}{2},\frac{3}{2}}$ and $30P_{\frac{1}{2},\frac{3}{2}}$. Figures 2.5, 2.6, and 2.7 are generated using the ARC library in Python [75]. The transition rates in Fig.2.7 were calculated by the authors in Ref. [76].

The total decay resulting from the spontaneous and BBR-induced decays can be expressed as their sum. So, from *Eqn.* 2.43 and 2.45, the total decay is,

$$\Gamma_{total} = \frac{1}{\tau_{lifetime}} = \Gamma_{spon} + \Gamma_{BBR}. \tag{2.46}$$

Here, $\tau_{lifetime}$ is the effective lifetime of the atom in a Rydberg state. It is

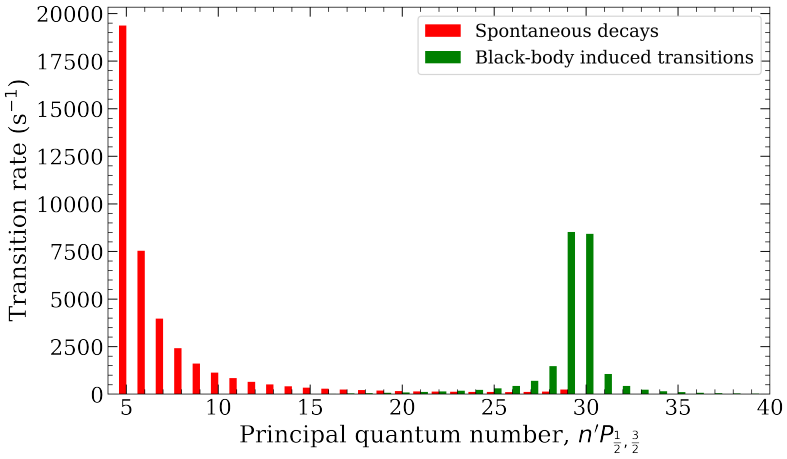


Figure 2.7: Transition rate from $30S_{\frac{1}{2}}$ to $n'P_{\frac{1}{2},\frac{3}{2}}$ states. Red-colored bars represent the transition rates due to the spontaneous emission and green-colored bars represent the transition rates due to the BBR.

clear from *Eqn.* 2.46 that effective lifetime depends on the radial component of the transition matrix element. It is calculated by various numerical methods [77] for Alkali atoms. The authors in the Ref. [76] calculated the lifetime of Rydberg states for different atoms using quasi-classical approach. They found that the lifetime due to radiative decay varies as,

$$\tau_0 = \tau_s n_{eff}^{\delta}. \tag{2.47}$$

They also deduced BBR-induced lifetime which can be written in parametrized form as,

$$\frac{1}{\tau_{BBR}} = \frac{A}{n_{eff}^{D}} \frac{21.4}{\exp(315780B/n_{eff}^{C}T) - 1} \tag{2.48}$$

So effective lifetime after combining the *Eqn.* 2.47 and 2.48 becomes,

$$\tau_{lifetime} = \tau_0 + \tau_{BBR} \tag{2.49}$$

The values of τ_s, δ, A, B, C and D for various atomic species can be found in the Ref. [76].

2.2.2 Interactions between Rydberg atoms

In this section, I will discuss the interactions between Rydberg atoms and the result of their interactions. If the two Rydberg atoms are separated by a distance (R) more than the Le Roy radius then their wave functions will not overlap, the Le Roy radius [78] for the two atoms having $|n_1, l_1, m_1\rangle$ and $|n_2, l_2, m_2\rangle$ states respectively is given as,

$$R_{LR} = 2(\sqrt{\langle n_1, l_1, m_1|r^2|n_1, l_1, m_1\rangle} + \sqrt{\langle n_2, l_2, m_2|r^2|n_2, l_2, m_2\rangle}). \tag{2.50}$$

The interaction potential [79] in this case can be written as,

$$V(r_1, r_2) = -\sum_{q=1}^{q=\infty} \frac{C_q}{R^q}. \tag{2.51}$$

For $q = 1$ and $q = 2$, the interaction potential becomes the Coulomb charge-charge potential and charge-dipole interaction, respectively. So the terms corresponding to $q = 1$ and $q = 2$ will be zero for neutral atoms. For $q = 3$, the interaction potential is the result of dipole-dipole interaction.

Let us consider an atom having a dipole moment $\vec{d_1}(\omega)$, which oscillates at an angular frequency ω. Classically, an oscillating dipole moment radiates an electric field. Let us denote the electric field generated by the first atom as $\vec{E_1}(\omega, r, t)$, then this electric field interacts with the other atom which has dipole moment $\vec{d_2}$. So the

dipole-dipole interaction between the two atoms is $\vec{E_1}(\omega, r, t).\vec{d_2}$.

Quantum mechanically, the dipole-dipole interactions occur by exchanging virtual photons. For interactions between Rydberg atoms with $n = 55$, the interatomic distance $R \approx 10\ \mu m$ and the wavelength (λ) of the photons or radiation is around $\approx 1\ mm$, so the interacting dipoles can be thought of as static in the $R << \lambda$ limit.

The potential operator due the dipole-dipole interaction [80] can be written as,

$$\hat{V}_{d-d} = \frac{1}{4\pi\epsilon_0}[\frac{\hat{d_1}.\hat{d_2}}{R^3} - 3\frac{(\hat{d_1}.\hat{R})(\hat{d_2}.\hat{R})}{R^3}]. \tag{2.52}$$

Let us consider two atoms initially in the Rydberg pair states $|r, r\rangle$, and dipole-coupled to the $|r', r''\rangle$ states. The energy defect between the final ($|r', r''\rangle$) and initial states ($|r, r\rangle$) is $\Delta_{r',r''} = E_{r'} + E_{r''} - 2E_r$, this energy defect is also called 'Forster defect'. The interaction Hamiltonian on pair state basis ($\{|r, r\rangle, |r', r''\}$) is given as,

$$\begin{bmatrix} 0 & V(R) \\ V(R) & \Delta_{r',r''} \end{bmatrix}. \tag{2.53}$$

Where, $V(R) = \langle r, r|\hat{V}_{d-d}|r', r''\rangle$.

The eigenvalues of the Hamiltonian (2.53) is $\lambda = \frac{\Delta_{r',r''} \pm \sqrt{\Delta^2_{r',r''} + V(R)^2}}{2}$.

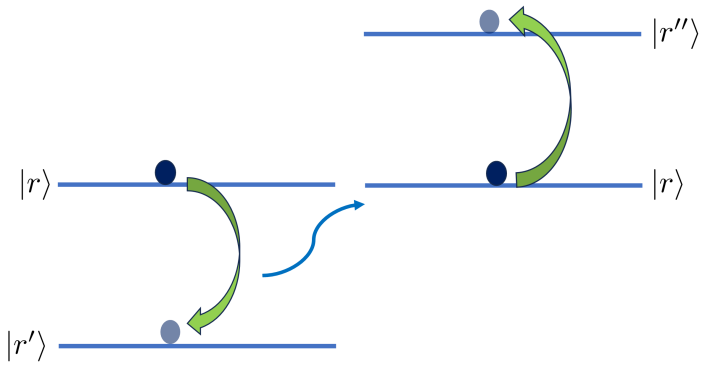


Figure 2.8: Mechanism of resonant dipole-dipole interaction

- $V(R) >> \Delta_{r',r''}$

  In this scenario [81], the energies of the eigen-states are $\lambda = \pm V(R)$, and so

energy shift of the $|r, r\rangle$ pair state due to the interaction with $|r', r''\rangle$ pair state is $V(R)$, and $V(R) \propto \langle \mathbf{d_1}.\mathbf{d_2} \rangle / R^3$. Since, $d_1 \propto n^2$, the energy shift $(V(R))$ scales as $\frac{n^4}{R^3}$. For $\Delta_{r',r''} = 0$, the interaction results to resonant dipole-dipole interaction.

The interaction mechanism is shown in the Fig.2.8. The first atom in $|r\rangle$ state releases one virtual photon and decays to $|r'\rangle$ state. The emitted virtual photon is then absorbed by the second atom and excited to $|r''\rangle$ state. As a result of resonant dipole-dipole interaction, atoms are redistributed to the new Rydberg states.

- $\Delta_{r',r''} >> V(R)$

  In this regime [81,82], the eigen values are $\lambda_1 = \Delta_{r',r''} + \frac{V(R)^2}{\Delta_{r',r''}}$ and $\lambda_2 = -\frac{V(R)^2}{\Delta_{r',r''}}$. The interaction energy scales as $\frac{n^8}{\Delta_{r',r''} R^6}$. If the interaction involves the neighborhood states then $\Delta_{r',r''} \propto n^{-3}$. So this kind of off-resonant interaction scales as $\frac{n^{11}}{R^6}$, this is called Van der Waals interaction, off-resonant as $\Delta_{r',r''} \neq 0$.

  Fig.2.9 shows the mechanism in this type of interaction.

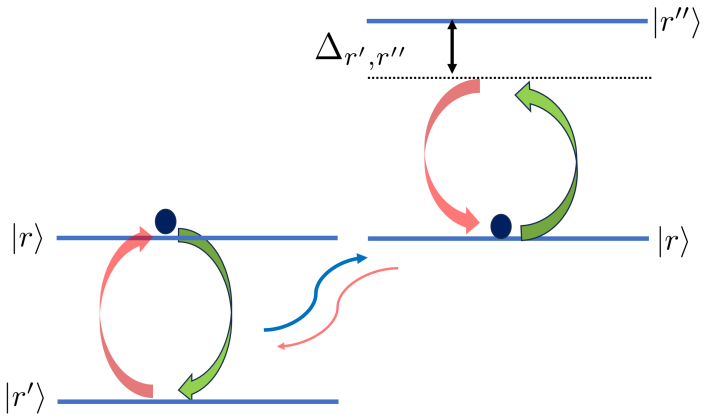


Figure 2.9: Van der Waals interaction mechanism

The second atom absorbs the virtual photon after it is emitted by the first atom. Since the energy defect $\Delta_{r',r''} \neq 0$, the second atom will not be excited to the $|r''\rangle$ state rather to a virtual state. The second atom then instantly releases the virtual photon and returns to the $|r\rangle$ state. The first atom absorbs the virtual photon and returns to the $|r\rangle$ state, as a result there is no distribution of atomic states. This is

a second-order process, as the virtual photon is exchanged twice. The energy shift of $|r,r\rangle$ states in this interaction is often represented as $V_{vdw}(R) = \frac{C_6}{R^6}$, the sign of C_6 can be positive (repulsive interaction) or negative (attractive interaction).

2.2.3 Rydberg Blockade

Rydberg blockade [8, 83] appears as a consequence of the dipole-dipole or Van der Waals interaction. Here I try to explain first the Rydberg blockade using two atoms and then extend the explanation to multiple atoms. From the previous section, the energy shift of $|r,r\rangle$ pair state due to the Van der Waals interaction is calculated as $V_{vdw}(R) = \frac{C_6}{R^6}$. So if one atom (atom A in Fig.2.11) is excited to the Rydberg state $|r\rangle$ then the energy shift of other atom's (atom B) Rydberg state $|r\rangle$ varies as $\frac{C_6}{R^6}$. For strong interaction, $V_{vdw}(R)$ is greater than the linewidth of $|r\rangle$ state, which results in prohibiting excitation of the second atom, this is known as Rydberg blockade. If Ω

$$|R_{coll}>=|r,g,g,\ldots,g>+|g,r,g,g,\ldots,g>+\cdots+|g,g,g,g\ldots,r>$$

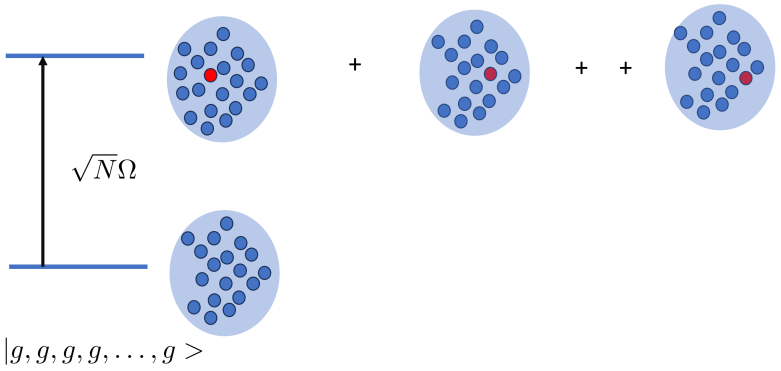


Figure 2.10: Super atom model due to the Rydberg blockade. Red colored point represents the Rydberg atom and blue colored points represent the ground state atoms.

be the Rabi frequency between $|g\rangle$ and $|r\rangle$ states and Γ_r is the dephasing rate of the Rydberg state $|r\rangle$. For $\Omega > \Gamma_r$, the condition for Blockade [82, 84] is

$$\frac{|C_6|}{R_B^6} = \hbar\Omega. \tag{2.54}$$

R_B is the blockade radius and it is expressed as $R_B = (\frac{C_6}{\hbar\Omega})^{\frac{1}{6}}$.

When there are multiple atoms (N) inside the blockade radius, then only one atom will be excited to the Rydberg state and the excitation of other atoms will be suppressed. The multi-atomic wave function of the atoms inside the blockade radius can be written as $|R_{coll}\rangle = \frac{1}{\sqrt{N}} \sum_i |g_1, g_2, g_3, r_i, \ldots, g_N\rangle$ [85] and the ground state wave function is $|G\rangle = |g_1, g_2, g_3, \ldots, g_N\rangle$. All atoms within the blockade radius (R_B)

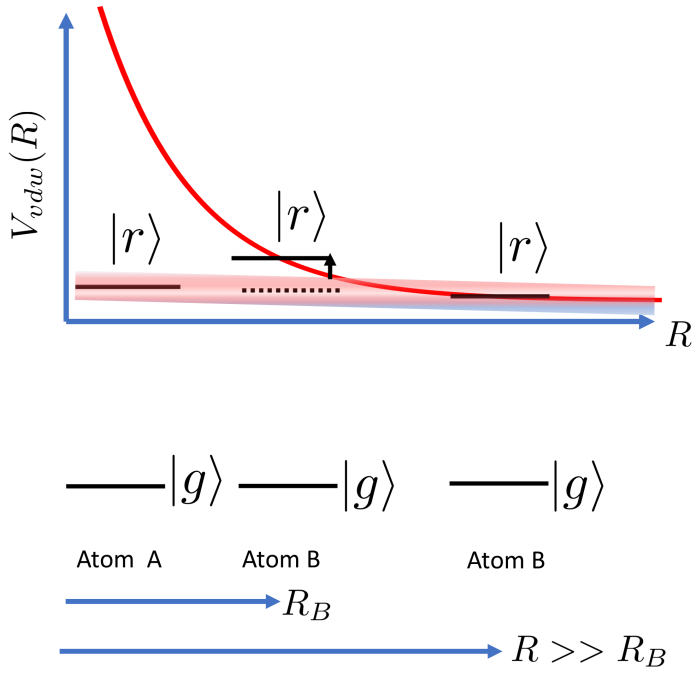


Figure 2.11: This figure shows the mechanism of Rydberg blockade. When the atom B is inside the blockade radius (R_B), the excited state ($|r\rangle$) of atom B undergoes a shift of $V_{vdw}(R) = \frac{C_6}{R_B^6}$. However at long distance $R >> R_B$, the shift is zero and both the atom can be simultaneously excited.

collectively act as a single atom that effectively has two energy levels; the collective system is called a super atom. The effective Rabi frequency of the superatom is written as $\Omega_{eff} = \langle R_{coll}|H_I|G\rangle = \sqrt{N}\Omega$. H_I is total interaction Hamiltonian of the collective system. A superatom with enhanced coupling plays crucial role in efficient single photon generation [86], quantum information processing [87] and many more. Fig.2.10 shows the pictorial representation of superatom [87, 88].

2.3 Conclusion

In this chapter, I have discussed Electromagnetically Induced Transparency and Autler-Townes splitting. The experiments described in this thesis utilizes these two phenomena for excitation to Rydberg states. I have also explained the Rydberg atom and it's distinctive properties. Strong dipole-dipole interactions between Rydberg atoms play an important role in quantum information processing, quantum sensing and Quantum simulation of many-body physics.

CHAPTER 3

Absolute transition frequency measurement of high lying Rydberg states using Electromagnetically Induced Transparency

To utilize the strong dipole-dipole interactions in Rydberg atoms and perform quantum sensing [35] using Rydberg atoms with high principal quantum number, it is essential to have the knowledge of the absolute transition frequencies of high-lying Rydberg states. In this chapter, I have shown the results on absolute transition frequency measurements of $nS_{\frac{1}{2}}$ and $nD_{3/2,5/2}$ Rydberg states of ^{87}Rb atom for a wide range of the principal quantum numbers $n = 45 - 124$. The accuracy of the measurement is ≤ 2 MHz. We also extract the values of the quantum defects for nS and nD states from the transition frequencies. We employ Electromagnetically Induced Transparency (EIT) scheme in a three-level ladder-type system for the measurement of transition frequencies. As discussed in chapter 2, EIT occurs due to the destructive quantum interference between the two transition pathways. We observe that for principal quantum numbers $n > 80$, the signal to noise ratio (SNR) of the EIT signal is less than 10. We use two kinds of lock-in detection technique in order to improve the SNR of the EIT signal. In the next section, I will discuss the results

of the experiment and also give the technical description of the lock-in detection scheme used in our setup.

3.1 Experimental setup

Fig.3.1 shows the schematic of our experimental setup. For three-level EIT scheme, two types of lasers are generally required: one is the probe laser and the other is the coupling laser. Probe laser is sourced from an External Cavity Diode Laser (ECDL, DL100 from Toptica) and it's frequency is tuned to the $\{5S_{\frac{1}{2}}, F = 2\} \rightarrow \{5P_{\frac{3}{2}}, F' = 3\}$ transition, with a wavelength of 780 nm.

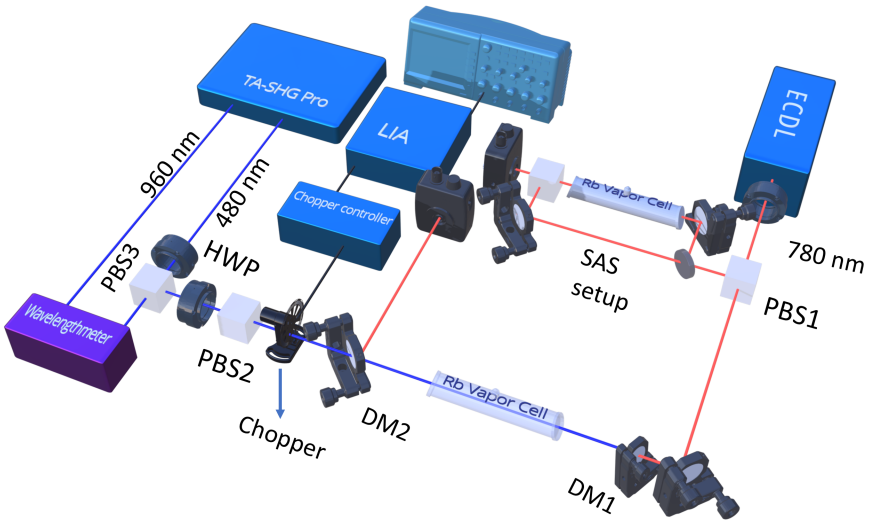


Figure 3.1: Vapor cell EIT setup used for the transition frequency measurements.

The coupling laser is obtained from a different tunable laser (TA-SHG pro from Toptica) and its frequency is tuned to $\{5P_{\frac{3}{2}}, F' = 3\} \rightarrow nl$, with a wavelength of 480 nm. This laser system works on the principle of second harmonic generation with master seed laser 960 nm and final output after the second harmonic generation is 480 nm. Since the coupling laser is tuned from $5P_{\frac{3}{2}}$ fine structure state, the final Rydberg states (nl) where the transition can occur are nS and nD. So we can only measure the transition frequencies of nS and nD states with respect to the $\{5P_{\frac{3}{2}}, F' = 3\}$ state in this experiment.

After the optical isolator (not shown in Fig.3.1), the laser beam of wavelength 780 nm is divided into two parts using a polarizing beam splitter (PBS1) and a half-wave plate (HWP): one part is sent to the saturation absorption spectroscopy (SAS) setup, and the other part is used as a probe laser. The probe laser is aligned through the vapor cell of length 10 cm using a dichroic mirror (DM1) and the FWHM diameter of the probe laser beam is 0.8 mm.

The coupling laser beam (480 nm) is split into two parts by using a PBS (PBS3) and a HWP: one part is sent to the wavelength meter for monitoring the frequency and the other part is overlapped with the probe laser beam in the counter-propagating direction using a dichroic mirror (DM2) to reduce the Doppler shift. The diameter of the coupling beam is 0.7 mm. The frequencies of the coupling beam (480 nm) and the and seed laser beam (960 nm) are monitored using a commercial wavelength meter from Highfinesse (model Highfinesse WS8-2) with an absolute accuracy of 2 MHz (frequency resolution of 200 kHz). The wavelength meter is placed in a thermally insulated box to reduce drift due to the external thermal fluctuation. We calibrate the wavelength meter using the laser locked to the $\{5S_{\frac{1}{2}}, F = 2 \rightarrow 5P_{\frac{3}{2}}, F' = 3\}$ transition with a linewidth of $\approx$ 400 kHz.

To measure the absolute transition frequencies to the Rydberg states, first the probe laser is locked to the $\{5S_{\frac{1}{2}}F = 2\} \rightarrow \{5P_{\frac{3}{2}}, F' = 3\}$ transition using saturation absorption spectroscopy technique. Then we record the Rydberg EIT signal by scanning the master laser (960 nm) of the TA-SHG pro laser, effectively scanning the coupling laser, and simultaneously recording the frequency on a wavelength meter. The transition frequency is determined by fitting the EIT signal using the pseodo-voigt function, as shown in Fig.3.2a. In this way, we could measure the transition frequencies upto 'n'=80. The Signal to Noise Ratio (SNR) of the Rydberg EIT signal for Rydberg states with 'n'¿80 is less than ten, making it challenging to fit the data and calculate the transition frequencies. So we use lock-in detection technique to enhance the SNR of the EIT signal. We use two kinds of lock-in detection technique: one is modulating the coupling intensity using a mechanical chopper and the other is modulating the frequency of the probe laser.

Fig.3.2b) represents the lock-in EIT signal of $50D_{\frac{5}{2}}$ Rydberg state measured

using modulating the intensity of coupling laser. In this case, the probe laser is locked to the $\{5S_{\frac{1}{2}}F = 2\} \rightarrow \{5P_{\frac{3}{2}}, F' = 3\}$ transition and the coupling laser is scanned across the resonance of the nl Rydberg state. One disadvantage of this method is that the mechanical noise from the chopper wheel impacts the long-term stability of the experimental system.

Another lock-in technique we use involves modulating the frequency of the probe laser. In this case, the coupling frequency is fixed near the transition frequency measured by previous methods and the probe laser is scanned across the D2 transition of ^{87}Rb with a modulation frequency of 4 kHz. For lock-in detection, we utilize the digital Lock-in Amplifier model SR-850 from Stanford Research Systems. The

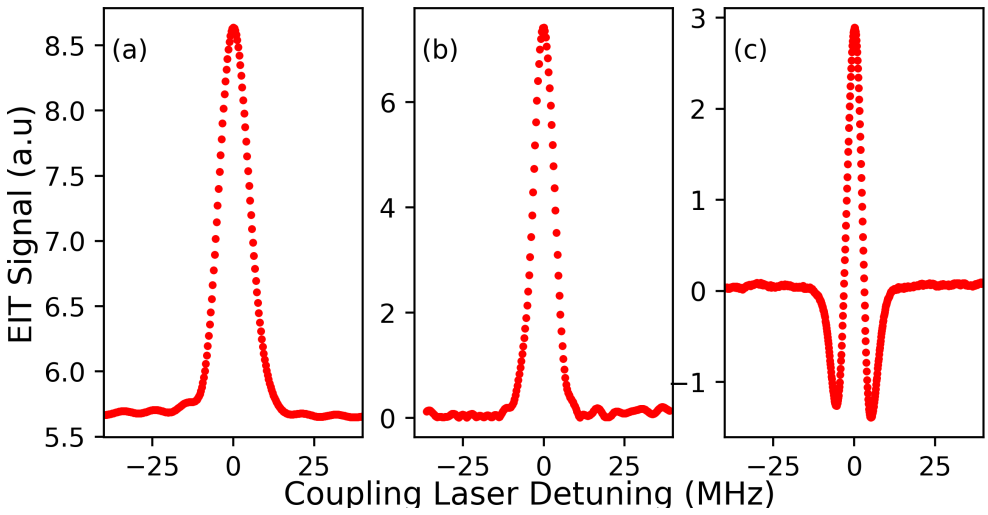


Figure 3.2: a) shows EIT signal by locking the probe laser and scanning the coupling laser. b) represents the lock-in signal measured by modulating the coupling beam, in this case probe laser is locked and coupling is scanned. c) shows the second harmonic of EIT signal measured by modulating the probe laser frequency, in this case probe laser is scanned and coupling laser is fixed near the resonance.

advantage of this method is that the frequency modulation is done via modulating the voltage given to the piezo of the the diffraction grating of the External Cavity Diode Laser (ECDL), making it free from mechanical vibration. Additionally, we are detecting the second harmonics (basically second derivative of the EIT signal) of the EIT signal, making it narrower than the original EIT signal, which helps reducing the error during the curve fitting for transition frequency estimation.

Fig.3.2c) illustrates the lock-in signal of $50D_{\frac{5}{2}}$ state detected using the probe frequency modulation technique. Each signal represents the average of 100 measurements. We first record both the Rydberg EIT and the Saturation Absorption Spectroscopy (SAS) signals. After averaging the signals, we convert to the frequency scale by finding the peak-to-peak distance of the SAS peaks and referencing their previously reported peak separation in frequency, as shown in Fig.3.3.

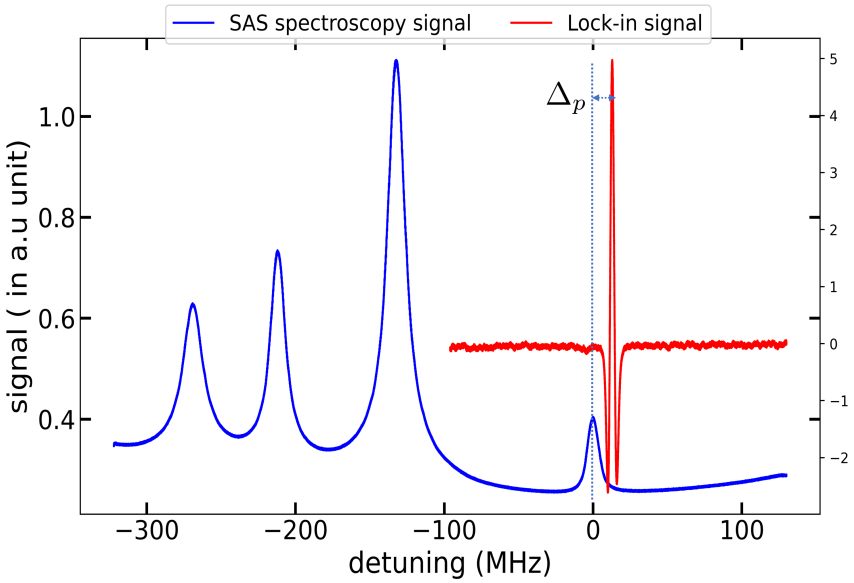


Figure 3.3: SAS signal and typical second harmonic of EIT signal recorded simultaneously.

We measure the peak-to-peak frequency (Δ_p) separation by fitting the $\{5S_{\frac{3}{2}}, F = 2\} \rightarrow \{5P_{\frac{3}{2}}, F' = 3\}$ SAS peak and the averaged lock-in signal. For a three-level ladder-type system in a counter-propagating arrangement, the Doppler shift arises due to the wave-vector mismatch between the probe (ω_p) and the coupling (ω_c) beams, disrupting the two-photon resonance condition (discussed in more detail in chapter4). Two-photon resonance will happen at the coupling detuning of,

$$\Delta_c = -\frac{\omega_c}{\omega_p}\Delta_p \tag{3.1}$$

Finally, we correct the shift (Δ_c) in the coupling frequency recorded with a wavelength meter.

3.2 Lock-in Detection

Lock-in detection is an effective technique that allows us to measure signals buried under the noise. It is a very useful technique to enhance the SNR of the noisy signals. It is achieved by first modulating the signal of interest with a specific frequency (reference frequency) and then the modulated signal is connected to a phase-sensitive detector (lock-in amplifier, model SR-850). The input modulated signal is multiplied with a reference signal inside the lock-in amplifier using a mixer circuit. Here, the reference signal is a sine or a cosine signal with the same modulation frequency generated from any signal generator which is used to modulate the signal. After that, the mixed signal is passed through a low-pass filter to filter out the high frequency components of the signals including the noise.

We generally use an external signal generator, whose output is connected to the external modulation connector located in the Lock-in Regulator (LIR-110 module) of the laser controller electronics rack of the Toptica DL-100 laser system. Here, we will provide a mathematical description of the lock-in detection technique, specifically the lock-in detection using the modulation of the probe frequency. Let us consider $I(\omega_p)$ as the signal, ω_p the angular frequency of the probe, Ω_m to be the modulation frequency and 'A' be the modulation amplitude. The typical modulation frequency for our case is set to ≈ 4 kHz. The frequency-modulated signal is written as $I(\omega_p + Asin\Omega_m t)$. Using Taylor expansion around ω_p,

$$I(\omega_p + Asin(\Omega_m t + \theta)) + N(t) = N(t) + I(\omega_p) + Asin(\Omega_m t + \theta)\frac{dI}{d\omega}|_{\omega_p} + \frac{A^2 sin^2(\Omega_m t + \theta)}{2}\frac{d^2 I}{d\omega^2}|_{\omega_p} + \dots$$

N(t) denotes the noise in the signal. Since we are detecting the second harmonic of the Rydberg EIT signal, modulated signal will be multiplied by $cos(2\Omega_m t + \phi)$ term

in the mixer circuit.

$$\{I(\omega_p + Asin(\Omega_m t + \theta)) + N(t)\} \times cos(2\Omega_m t + \phi) = N(t) \times cos(2\Omega_m t + \phi)$$
$$+I(\omega_p) \times cos(2\Omega_m t + \phi) + Asin(\Omega_m t + \theta)\frac{dI}{d\omega}|_{\omega_p} \times cos(2\Omega_m t + \phi) +$$
$$\frac{A^2 sin^2(\Omega_m t + \theta)}{2}\frac{d^2 I}{d\omega^2}|_{\omega_p} \times cos(2\Omega_m t + \phi) + \ldots$$

The low-pass filter removes all the high-frequency components, including the noise, leaving only the DC component as the output. The lock-in output is $\propto \frac{A^2}{4}\frac{d^2 I}{d\omega^2}|_{\omega_p}$ (see Fig.3.3), so in this technique we detect the second derivative of the Rydberg EIT signal. $(2\theta - \phi)$ is the phase difference between the signal and the reference signal. The lock-in output can be maximized by adjusting the phase difference.

3.3 Results and discussion

Rydberg atoms resemble hydrogen-atom-like energy scaling. So energy [34, 89] of the $|n, l, j\rangle$ states relative to the ionization limit E_i can be written as,

$$E_{nlj} = E_i - \frac{R_{Rb}}{(n - \delta_{nlj})^2} \tag{3.2}$$

where δ_{nlj} is the quantum defect discussed in the chapter 2. R_{Rb} is the Rydberg constant of ^{87}Rb atom and it is given as,

$$R_{Rb} = \frac{m_{Rb} R_\infty}{m_e + m_{Rb}} \tag{3.3}$$

We measure the transition frequencies of $nS_{\frac{1}{2}}$, $nD_{\frac{3}{2}}$ and $nD_{\frac{5}{2}}$ states. Since the hyperfine effect of the $nS_{\frac{1}{2}}$ states are strong, the only allowed hyperfine state is $\{nS_{\frac{1}{2}}, F'' = 2\}$. The hyperfine shift [90] of $\{nS_{\frac{1}{2}}, F'' = 2\}$ level is given as,

$$\Delta_{hfs,F=2} = \frac{3}{8}\frac{37.1(2)}{n^{*3}} GHz \tag{3.4}$$

In the experiment, we directly measure the transition frequencies of $\{5P_{\frac{3}{2}}, F' = 3\} \rightarrow \{nS_{\frac{1}{2}}, F'' = 2\}$ transition. We subtract the shift (in Eq.3.4) from the measured

transition frequencies to estimate the same for the states $nS_{\frac{1}{2}}$.

However, the hyperfine effect for the high principal quantum nD states is negligible, so we directly measure the transition frequencies of these states.

Fig.3.4a) shows the fine structure splitting of nD states with the principal quantum number 'n'. The fine structure splitting of nD states vary as $\propto \frac{A}{n^3}$ [34, 89]. Fig.3.4b) shows that lock-in detection signal of Rydberg EIT for the D levels of n = 46, 55 and 88. It is clear that the the fine structure splitting decreases as the value of 'n' increases. We observe the fine structure splitting upto 'n'=120. Beyond n=120, the fine structure splitting and the linewidth of the lock-in detection signal becomes the same order of magnitude, making it difficult to measure further. We could measure the transition frequencies of nS levels upto 'n'=124 as the SNR of the lock-in detection signal reduces after this level.

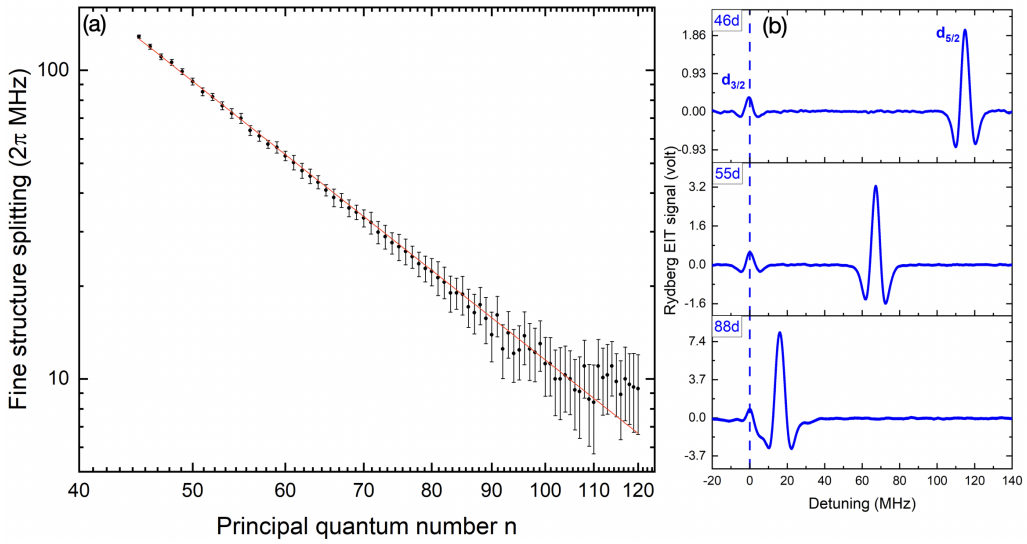


Figure 3.4: a)Fine structure splittings of D-levels b) shows the lock-in signals of EIT for $46D, 55D$ and $88D$ levels.

Quantum defects of $nS_{\frac{1}{2}}$, $nD_{\frac{3}{2}}$ and $nD_{\frac{5}{2}}$ states are determined by fitting the measured transition frequencies vs 'n' graphs using the equations 3.2 and 2.41. The values of quantum defects are given in the table below.

Previously measured quantum defects are reported in [54, 90–93] The error due to the fluctuations of the coupling laser $\approx$ 600 kHz. Maximum error sources include frequency conversions, peak frequency detection of lock-in detection signals from the fit and fluctuation of the probe laser ($\approx$ 650 kHz).

	δ_0	δ_2
$nS_{1/2}$	3.1311809(12)	0.1786(6)
$nD_{3/2}$	1.3480942(15)	−0.6048(9)
$nD_{5/2}$	1.3464628(14)	−0.5934(8)

Table 3.1: Values of the quantum defects.

3.4 Conclusion

In this experiment, we have measured the transition frequencies of $nS_{\frac{1}{2}}$, $nD_{\frac{3}{2}}$ and $nD_{\frac{5}{2}}$ Rydberg levels of ^{87}Rb atom for a wide range of principal quantum numbers n=45-124. We also determine the quantum defects of these states. We have also calculated the fine-structure splitting of D states and plotted it's variation vs n in Fig.3.4. Our measurements enable us to determine the transition frequencies of individual Rydberg states which is crucial for quantum computing [94] and quantum simulation with Rydberg atoms. Rydberg atoms are the perfect candidates for atom-based sensors as they have long lifetime and high polarizability ($\propto n^7$). The knowledge of the highly excited Rydberg states is useful for performing electrometry as well as [3], microwave detection [15] using Rydberg atoms.

CHAPTER 4

Doppler-Enhanced Quantum-Magnetometry using Rydberg atoms at room-temperature

In this chapter, we present experimental results demonstrating the combined effect of quantum interference and Doppler shift at room temperature to detect weak magnetic fields. We use the quantum interference phenomenon called Electromagnetically Induced Transparency (EIT) in a three-level ladder type system of ^{87}Rb atoms for the measurements. Electromagnetically Induced Transparency is a phenomenon resulting from the destructive quantum interference of the transition probabilities of the two transitions in a three-level system. This occurs due to light-matter interactions that renders an absorptive medium transparent. While in conventional three-level ladder-type setup, it is customary to use the probe and the coupling beams in a counter-propagating configuration to minimize the effect of Doppler shifts, here we show, on the contrary that one can harness the effect of Doppler shifts in copropagating arrangement to create an enhanced response to a magnetic field. In particular, we demonstrate an order-of-magnitude larger Zeeman splitting of EIT spectra in co-propagating configuration as compare to counter-propagating case. We also show that this enhancement is controlled by $\frac{\omega_p}{\omega_c}$ factor, where $\omega_{p(c)}$ is the probe (coupling) frequency. Our results are explained and interpreted through

numerical simulation and theoretical modeling based on Lindblad master Eqn.2.1. These findings offer promising applications in quantum sensing of magnetic fields using thermal Rydberg atoms.

4.1 Interaction with external magnetic fields

The splitting of the atomic energy levels due to the interaction between the magnetic moment of the atomic electron and the external magnetic field (B) is called the Zeeman effect. Depending on the strength of external magnetic field (B) compared to the atom's internal magnetic field, Zeeman effect is divided into three regimes,

a) Weak-field Zeeman effect

b) Intermediate-field Zeeman effect

c) Strong-field Zeeman effect.

4.1.1 Weak-field Zeeman effect of Hyperfine state

If the external magnetic field is less than the internal magnetic field of atom, then the hyperfine quantum number (F) is a good quantum number. The interaction Hamiltonian is given as

$$\hat{H_B} = \mu_B g_F F_z B_z \tag{4.1}$$

B_z is the external magnetic field along z-direction, F_z is the projection of the hyperfine quantum number (F) along the z-direction, μ_B is the Bohr magneton. The hyperfine Lande g-factor g_F is given as [95],

$$g_F = g_J \frac{F(F+1)-I(I+1)+J(J+1)}{2F(F+1)} + g_I \frac{F(F+1)-J(J+1)+I(I+1)}{2F(F+1)}$$

the Lande g-factor is given as, $g_J = g_L \frac{J(J+1)-S(S+1)+L(L+1)}{2J(J+1)} + g_S \frac{J(J+1)-L(L+1)+S(S+1)}{2J(J+1)}$

The Lande g-factor for an orbital is $g_L = 1$ and the Lande g-factor for an electron spin is $g_S \approx 2$.

The splitting can be calculated by using the first-order perturbation theory and it is derived in Eqn. 4.1 as

$$\Delta E_{F,m_F} = g_F \mu_B B_z m_F \tag{4.2}$$

4.1.2 Strong-field Zeeman effect

In this case, the external magnetic field is stronger than the internal magnetic field of the atom. So the hyperfine state (F, m_F) is not a good quantum number under the strong magnetic field as it decouples the interaction between nuclear spin (I) and the total angular momentum (J). The interaction Hamiltonian is expressed as

$$\hat{H_B} = A_{hfs} I_z J_z + B_{hfs} \frac{3(I_Z J_z)^2 + \frac{3}{2} I_z J_z - I(I+1)J(J+1)}{2J(2J-1)I(2I-1)} + \mu_B (g_j J_z + g_I I_z) B_z \tag{4.3}$$

A_{hfs} is the hyperfine constant, B_{hfs} is the electric quadrupole constant. This effect is also known as the Paschen-Back effect.

In this regime, for ^{87}Rb, the energy shift of $nS_{\frac{1}{2}}$ state is calculated as,

$$\Delta E_{Jm_J Im_I} = A_{hfs} m_J I m_I + \mu_B (g_j m_J + g_I m_I) B_z \tag{4.4}$$

the value of $B_{hfs} = 0$([96]) for $nS_{\frac{1}{2}}$

4.1.3 Intermediate-field Zeeman effect

Intermediate-field Zeeman effect arises when the magnetic field is neither too strong nor too low but in the intermediate level. In this regime, it is difficult to find out the good quantum number. For hyperfine state, the total interaction Hamiltonian in this regime is given as

$$\hat{H} = \hat{H_A} + \hat{H_B} \tag{4.5}$$

where $\hat{H_B} = (\mu_B g_J J_z + \mu_B g_I I_z)B_z$ and $\hat{H_A}$ is the atomic Hamiltonian.
The energy splitting in this regime is obtained by numerically diagonalizing the Hamiltonian (4.5 in $|F, m_F\rangle$ ([97]) basis.
In this experiment, the atomic states, the $5S_{\frac{1}{2}}, 5P_{\frac{3}{2}}$ and $nS_{\frac{1}{2}}$ are involved. Hyperfine levels of $5S_{\frac{1}{2}}, 5P_{\frac{3}{2}}$ states will experience weak-field Zeeman effect at a magnetic field of around 30 Gauss. For principal quantum number (n) > 30, the hyperfine interaction of the Rydberg levels is very small compared to the interaction caused by an external magnetic field, so the Rydberg states will be in the Paschen-Back regime.

Here, the Zeeman splittings per unit Gauss magnetic field for $5S_{\frac{1}{2}}$, $5P_{\frac{3}{2}}$ and $35S_{\frac{1}{2}}$ are tabulated in Table 4.1, Table 4.2 and Table 4.3 respectively.
For the $|5S_{\frac{1}{2}}, F = 2\rangle$ state, the Zeeman splittings are calculated using Eq. 4.2 with $g_F = \frac{1}{2}$.

Table 4.1: weak-field Zeeman splitting of $|5S_{\frac{1}{2}}, F = 2\rangle$ per unit Gauss of magnetic field.

state ($\|F, m_F\rangle$)	Splitting(MHz)/Gauss
2,-2	-1.39962
2,-1	-.6998
2,0	0
2,1	.6998
2,2	1.39962

For the $|5P_{\frac{3}{2}}, F = 3\rangle$ state, the weak-field Zeeman splitting is calculated using Eq. 4.2 and the value of g_F is taken as $= \frac{2}{3}$.

In the presence of a strong magnetic field, $|F, m_F\rangle$ is not a good quantum state for Rydberg state $|nS_{\frac{1}{2}}\rangle$. Instead, $|J, m_J, I, m_I\rangle$ is now a good quantum state. This is also called decoupled state. The strong-field Zeeman splittings of this state is calculated using Eq. 4.4.

The value of $A_{hfs} = \frac{37.1}{2n^{*3}}$ GHz is taken from [90], where $n^* = n - \delta$, δ being the quantum defect. For $35S_{\frac{1}{2}}$ state $n^* = 31.8686$, $g_J = 2$.

For ^{87}Rb, the Lande g-factor of Nucleus spin is $g_I = -.00100627$

Table 4.2: Weak-field Zeeman splitting of $|5P_{\frac{3}{2}}, F = 3\rangle$ per unit Gauss of magnetic field

state ($\|F, m_F\rangle$)	Splitting MHz/Gauss
3,-3	-2.79925
3,-2	-1.86617
3,-1	-.93308
3,0	0
3,1	.93308
3,2	1.86617
3,3	2.79925

Table 4.3: Strong-field Zeeman effect of $35S_{\frac{1}{2}}$ state

states($\|m_I, m_J\rangle$)	frequency splitting MHz/Gauss
-3/2,-1/2	-0.9676
-3/2,1/2	0.97189
-1/2,-1/2	-1.25564
-1/2,1/2	1.25704
1/2,-1/2	-1.54361
1/2,1/2	1.54220
3/2,-1/2	-1.83158
3/2,1/2	1.82736

4.2 Experimental Setup

The schematic of the experimental setup is shown in Fig. 4.1. For Rydberg ladder type EIT, we utilize three hyperfine manifolds $\{5S_{\frac{1}{2}}, F = 2\} \rightarrow \{5P_{\frac{3}{2}}, F' = 3\} \rightarrow \{35S_{\frac{1}{2}}, F'' = 2\}$ of ^{87}Rb.

The 780 nm laser is used as a probe for the $\{5S_{\frac{1}{2}}, F = 2\} \rightarrow \{5P_{\frac{3}{2}}, F' = 3\}$ transition and the 480 nm laser is used as a coupling beam for the $\{5P_{\frac{3}{2}}, F' = 3\} \rightarrow \{35S_{\frac{1}{2}}, F'' = 2\}$ transition. The probe beam is drawn from an External Cavity Diode Laser (Toptica DL100) and scanned across the $\{5S_{\frac{1}{2}}, F = 2\} \rightarrow \{5P_{\frac{3}{2}}, F' = 3\}$ transition. The coupling beam is derived from a frequency-doubled ECDL laser (Toptica TA-SHG pro) and tuned to the $\{5P_{\frac{3}{2}}, F' = 3\}$ to $\{35S_{\frac{1}{2}}, F'' = 2\}$ transition at 480 nm by tuning the seed laser at 960 nm.

A commercial wavelength meter based on Fizeau interferometer (WS8-2) is used to monitor the frequency of the coupling laser as it's frequency is fixed to $\{5P_{\frac{3}{2}}, F' = 3\}$ to $\{35S_{\frac{1}{2}}, F'' = 2\}$ transition. The absolute accuracy of the wavelength meter is 2

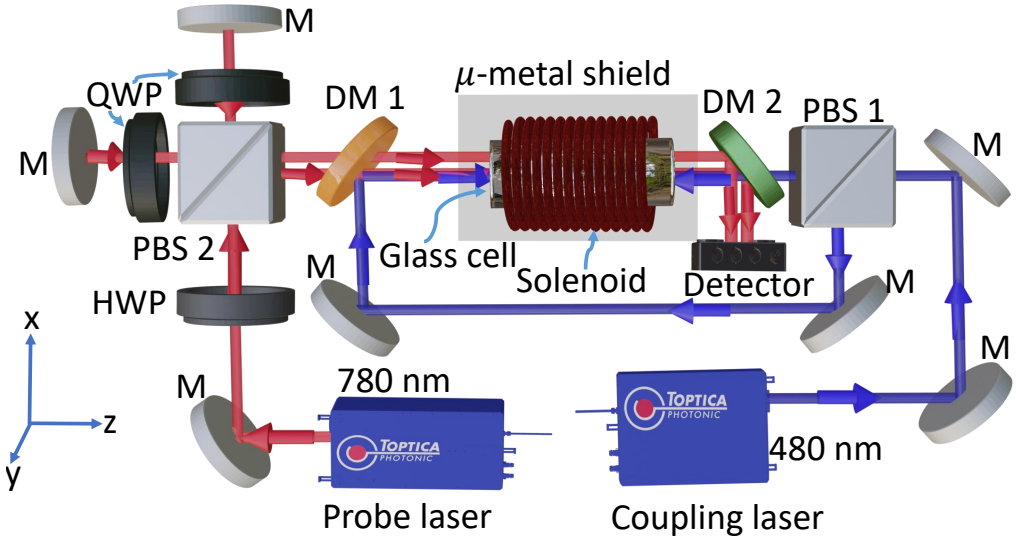


Figure 4.1: Schematic diagram of the Experimental setup. The red colored beam represents the probe beam (780 nm). The blue colored beam (480 nm) represents the coupling beam. PBS: Polarising Beam Splitter; DM: Dichoric Mirror; HWP: Half Wave Plate; QWP: Quarter Wave Plate; M: Mirror

MHz with a resolution of 200 KHz. As illustrated in Fig. 4.1, the probe laser is split into two parts by a polarizing beam splitter (PBS2) with same size and same power: one part is used as a probe beam and the other part is used a reference beam. The reference beam is used to subtract the background of EIT and to record the data on a flat background as the EIT signal resides on the Doppler broadened profile. This is done by setting the same power to the reference and probe beams and collecting the data on a home-built differential photo-detector. Both the probe and the reference beams are collimated with a Gaussian ($\frac{1}{e^2}$) radius of 0.7 mm and aligned through a 75 mm vapor cell. The coupling beam (480 nm) is divided into two parts by a polarizing beam-splitter (PBS1), one part of the coupling beam is aligned in counter-propagating configuration with the probe beam and the other part is aligned in co-propagating configuration with the probe beam. The Gaussian radius of these two beams are 1.2 mm and 0.7 mm, respectively . The reference beam is propagated through the vapor cell without overlapping with any of the coupling beams to provide a Doppler broadened background spectrum for background correction.

A solenoid coil is used to generate a static and uniform magnetic field along its axis (z-axis in Fig. 4.1) with a magnetic field of 33.616 Gauss/Amp. The magnetic

field along it's axis is measured by a Gaussmeter Model 460 3-channel from Lake Shore Cryptonics. The Rb vapor cell of length 75 mm is placed along the axis of the solenoid where the magnetic field is uniform. The vapor cell and the solenoid coil are magnetically shielded by three layers of μ-metal sheets to prevent the influence of ambient stray magnetic fields on the Rydberg EIT signal. The enclosure made of three layers of μ-metal sheets is tested to reduce the external stray magnetic field to below 0.05 Gauss.

Characterization of the Solenoid:

The solenoid coil used in our experiment has a length of 15 cm. We use a Gaussmeter to measure the magnetic field at different coil currents along the axis of the coil.

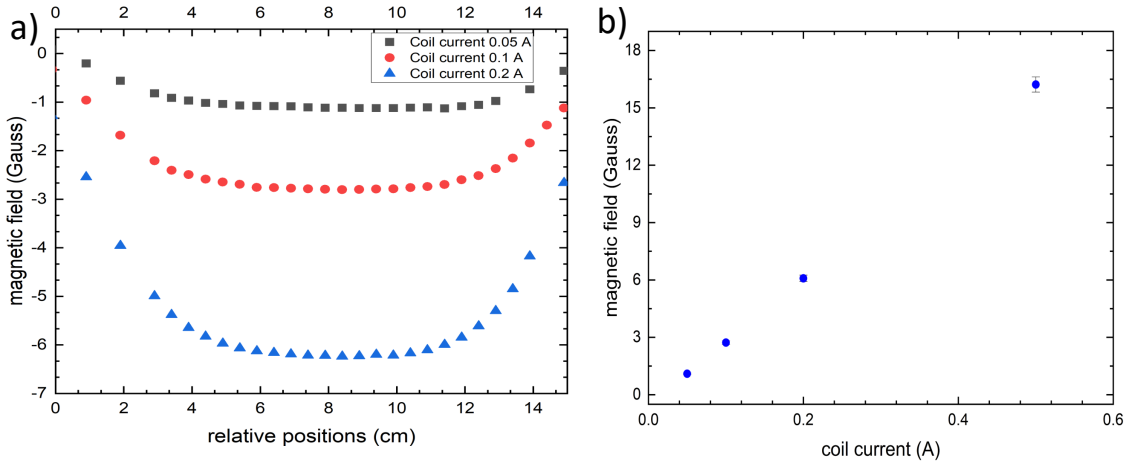


Figure 4.2: a) Shows the magnetic field variation along its axis. The same is measured at different coil currents. The origin (0 point in the graph) started from one side of the coil. b) it shows the average magnetic field vs the coil current (see text).

From figure 4.2a) the average value of the magnetic field is calculated across the uniform region (approximately taken from 3.9 cm to 11.5 cm for our vapor cell of length 7.5 cm, see Fig.4.2a)). The average values are plotted with different coil currents in Fig.4.2b). The magnetic field per unit current is determined by fitting the curve, shown in Fig.4.2, and the magnetic field is measured to be 33.616 Gauss per Ampere. Magnetic fields are varied from 0 to 10 Gauss to record the measurements. The standard deviation of the magnetic field along the axis in the uniform region is

around 0.2 Gauss.

4.3 Theoretical Model

In chapter 2, the zero temperature susceptibility (Eqn.(2.35)) for the three-level ladder system is derived analytically. In this chapter, the experiment conducted in a room-temperature vapor cell is described in detail. So the effect of the temperature needs to be corrected in the analytical expression for the susceptibility. For an atom moving towards the probe beam at a speed of 'v' sees it blue shifted by $\frac{\omega_p v}{c}$ (see Fig.4.3). The same atom sees the coupling frequency red (blue) shifted by $\frac{\omega_c v}{c}$ if it is in counter-propagating (co-propagating) configuration with respect to the probe beam. So the effective susceptibility will be evaluated after thermal averaging

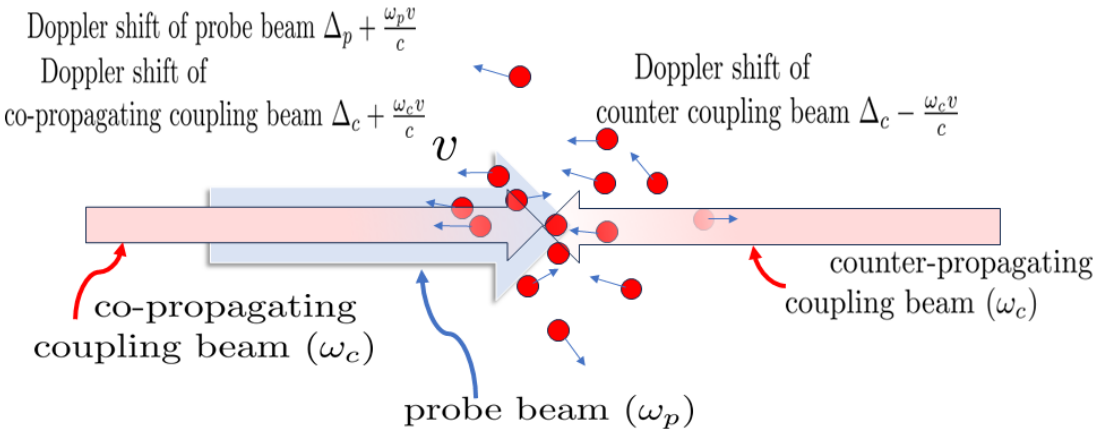


Figure 4.3: Doppler shift of an atom with velocity v with respect probe and coupling beam

the zero temperature susceptibility (Eqn. (2.35)). Hence, the thermally averaged susceptibility over the Boltzmann distribution is given as,

$$\chi = \frac{1}{\sqrt{\pi}} \int_{-\infty}^{+\infty} e^{-u^2} \chi_0(\Delta_p + \Delta_p^T u, \Delta_c \mp \Delta_c^T u)\, du, \tag{4.6}$$

with $u = \frac{v}{v_T}$, $\Delta_{p(c)}^T = \frac{\omega_{p(c)} v_T}{c}$ and $v_T = \sqrt{\frac{2k_B T}{m}}$, m being the mass of ^{87}Rb and k_B being the Boltzmann constant. At room temperature T=300 K, the Doppler shifts $\Delta_{p(c)}^T$ are hundreds of MHz, which has a strong impact on re-scaling the susceptibility.

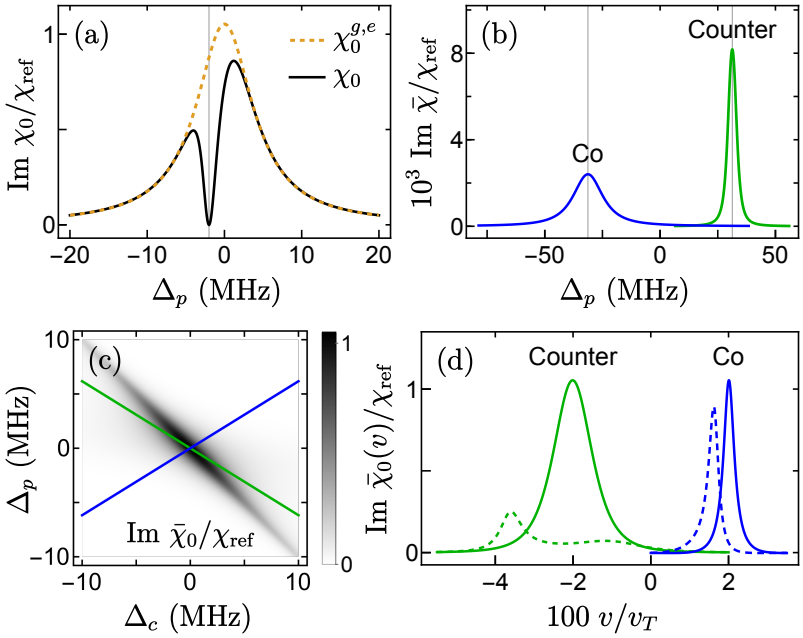


Figure 4.4: a) Black line represents the imaginary part of zero-temperature susceptibility at $\Delta_c = 2MHz$ and $\sigma^+ - \sigma^-$ polarization, dotted curve shows the imaginary part of susceptibility without coupling beam, vertical line represents the two-photon resonance condition for zero-temperature, $\Delta_p = -\Delta_c$, where $\chi_{\rm ref} = 2Nea_0/(\varepsilon_0\mathcal{E}_p) \approx 2\times10^{-4}$. b) Imaginary part of thermally averaged susceptibility $\bar{\chi} = \chi^{g,e} - \chi$, with $\Delta_c = -51$ MHz, vertical lines corresponding to the two-photon resonant condition, $\Delta_p = \mp\Delta^*$, where $\Delta^* = \frac{\omega_p}{\omega_c}\Delta_c$. c) Describes the zero temperature difference susceptibility $\bar{\chi}_0$, corresponding to a narrow EIT window, green (blue) line represents the thermal averaged counter-propagating (co-propagating) peak as $\Delta_p = \mp\Delta^*$. d) Contribution of different velocities to the susceptibility $\chi_0(v) := \chi_0(\Delta_p + \omega_p v/c, \Delta_c \mp \omega_c v/c)$, for $\Delta_c = -10$ MHz at $\Delta_p = \mp\Delta^*$ (solid lines) and at $\Delta_p = \mp\Delta^*/2$

In the experiment, the EIT signal resides on a Doppler-broadened profile. Hence, to clearly observe the signal we subtract the Doppler-broadened profile from the main EIT signal (see Fig.4.1). The background-subtracted susceptibility can be written as $\bar{\chi} = \chi^{ge} - \chi$, χ^{ge} is the two-level susceptibility when the coupling laser beam is absent. Another way to obtain $\bar{\chi}$ is thermal averaging of zero temperature counterpart $\bar{\chi_0} := \chi_0^{ge} - \chi_0$ as in Eqn. (4.6). The imaginary part of the zero-temperature susceptibility χ_0 drops to zero at the two-photon resonance condition, $\Delta_p + \Delta_c = 0$, while $\mathbf{Im}(\chi_0)$ matches the Lorentzian profile of $\mathbf{Im}(\chi_0^{g,e})$ off-resonantly (see Fig.4.4a)). At room temperature, the exact analytical expression of the integral 4.6 is difficult to achieve, so some approximations are needed to determine the approximate form. The integration can also be evaluated numerically by performing

numerical integration using any computation software. In thermally averaging $\bar{\chi_0}$, the effective velocity range of u comes from the two-photon resonance condition limited by the EIT linewidth i.e

$$|\Delta_p + \Delta_c + (\Delta_p^T \mp \Delta_c^T)u^*| = w_{EIT} \tag{4.7}$$

where w_{EIT} is the EIT window. From Eqn. 4.7, the range of effective velocities contributing to the EIT lineshape is obtained as $\Delta u^* = \frac{2w_{EIT}}{\Delta_p^T \mp \Delta_c^T}$. The -(+) sign indicates the counter-propagating (co-propagating) configuration. For two-photon resonance condition,

$$\Delta_p + \Delta_c + (\Delta_p^T \mp \Delta_c^T)u = 0 \tag{4.8}$$

so for any velocity u, coupling detuning Δ_c and probe detuning Δ_p, the EIT peak will be located at $Im(\chi_0^{g,e}(\Delta_p + \Delta_p^T u))$. Using Eq. 4.8, we get

$$\Delta_p + \Delta_p^T u = \frac{(\omega_c \Delta_p \pm \omega_p \Delta_c)}{(\omega_c \mp \omega_p)} \tag{4.9}$$

The integral (4.6) can be approximated as a rectangular integral in the Δu^* velocity range and

$$Im(\bar{\chi}) = \frac{A}{(\omega_c \mp \omega_p)} Im(\bar{\chi_0}^{g,e}(\frac{(\omega_c \Delta_p \pm \omega_p \Delta_c)}{(\omega_c \mp \omega_p)})). \tag{4.10}$$

where A is a slowly-varying function of Δ_p and Δ_c. We also assume that $|\omega_c - \omega_p| \gg \omega_p \frac{w_{EIT}}{w_{ge}}$, w_{ge} being the two-level absorption window (linewidth of $\chi_0^{g,e}$), set by the lifetime of the excited state. The condition for the EIT peak position between Δ_p and Δ_c will be calculated from expression (4.10) as ,

$$\Delta_p = \mp \frac{\omega_p}{\omega_c} \Delta_c \tag{4.11}$$

As $Im(\bar{\chi})$ tends to zero at two-photon resonance condition, $\Delta_p + \Delta_p^T u = 0$.

The '-'(+) sign represents the counter-propagating (co-propagating) configuration. From expression (4.10), we get two distinct features for co-propagating and

counter-propagating EIT. One is that the height varies as $\propto \frac{1}{\omega_c \mp \omega_p}$, and the other is that the linewidth varies as $\propto (1 \mp \frac{\omega_c}{\omega_p}) w_{ge}$. So the counter-propagating EIT signal is narrower and taller than that of the co-propagating EIT signal (see figure 4.4 b)). This is quite visible in figure 4.4 (c) and (d) as a broader range of velocities contribute to the signal, but this range falls off rapidly as one deviates from $\Delta_p = -\frac{\omega_p}{\omega_c}\Delta_c$.

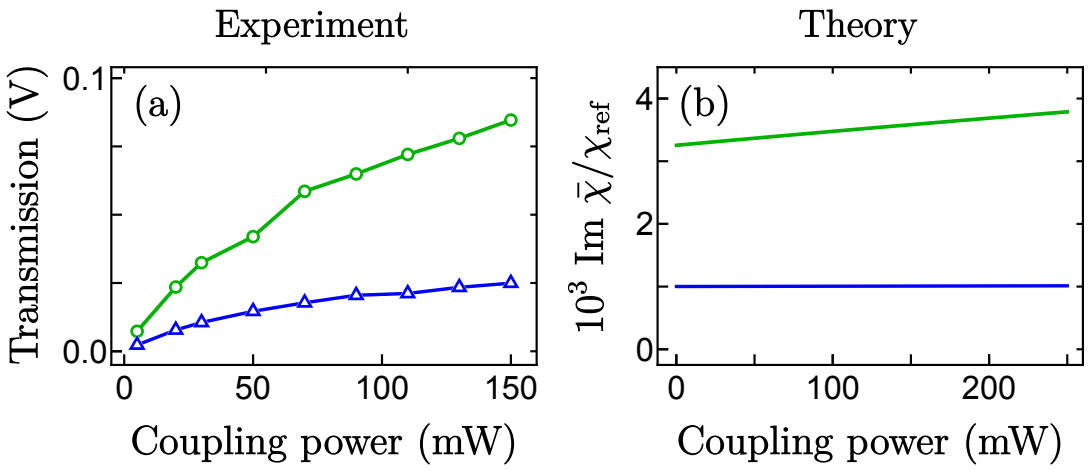


Figure 4.5: Measurements (left) and simulations (right) of the peak strength vs coupling laser power for $x-x$ polarizations. Green color curve represents the counter-propagating and blue color curve represents the co-propagating EIT.

4.4 Results and Discussion

In Fig.4.5, we experimentally measure the peak heights of the EIT signals in both the counter-propagating and co-propagating configurations as a function of coupling beam power and compare these results with simulations. The main difference between the experimental results and simulation is that as the coupling beam power reduces to zero the experimental signals go to zero but steady state susceptibility does not. This can be explained due to various factors such as the relaxation time diverges, dephasing due to the laser linewidth, stochastic resetting [98] due to the atom leaving the probe comes into play.

The dephasing effects, stochastic resetting affect the linewidth and strength of the EIT signal but it does not affect the peak position.

We have also measured the peak positions for both types of EIT configurations

by varying the detuning of the coupling beam (see Fig.4.6). It is observed that the co-propagating EIT peak follows $\Delta_p = +\frac{\omega_p}{\omega_c}\Delta_c$ and the counter-propagating EIT peak follows $\Delta_p = -\frac{\omega_p}{\omega_c}\Delta_c$ as derived in 4.11. It is important to note that the experimental data shows a slight difference in EIT strengths between the co-propagating and the counter-propagating configurations. Since the data for both the configurations is recorded simultaneously, the coupling power is adjusted accordingly to have the corresponding signal strength. For the same reason, the two different types of EIT signals are not visible at $\Delta_c = 0$ coupling detuning. Instead, a single convoluted peak is observed. For clarity, the numerically calculated susceptibility for the co-propagating configuration is multiplied by a factor 3 as the relative signal strength for this case is low (reason is stated in the last paragraph). The data showed in Fig. 4.6 is recorded in the absence of magnetic field ($B = 0$) with polarizations of the probe and the coupling beams kept linear.

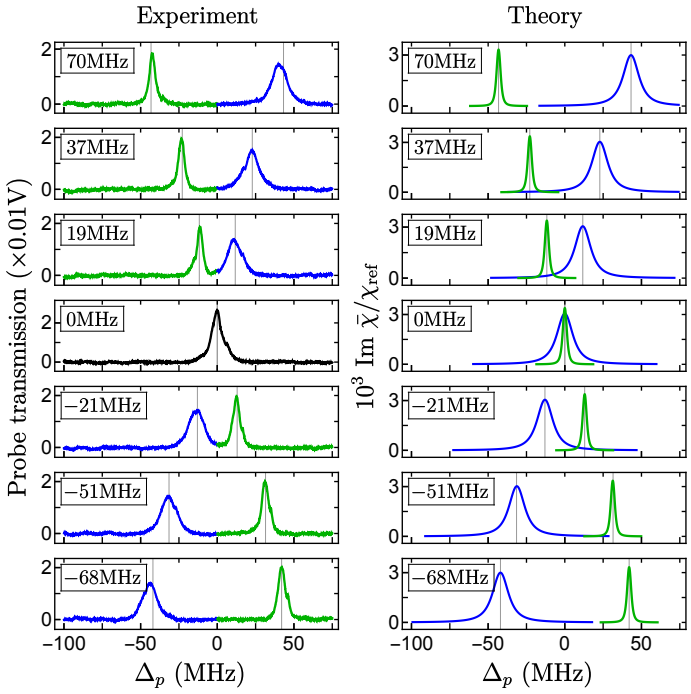


Figure 4.6: Measurements (left) and simulation (right),green curve represents counter configuration EIT and blue curve represents co-propagation configuration EIT.

Effect of the magnetic field:

In the presence of the DC magnetic field, all the states involved in the EIT will

experience Zeeman effect. For this experiment, the effect of the magnetic fields on the atomic energy levels are described in section 4.1. Due to the presence of the magnetic field, the degeneracy of all the energy levels will be lifted, resulting in splitting of the energy levels. The polarizations of the probe and the coupling lasers will determine the characteristics of this splitting.

The ground-state of ^{87}Rb $\{5S_{\frac{1}{2}}, F = 2\}$ has 5 Zeeman sub-levels and the energy level splitting with the magnetic field 'B' is given as,

$$\varepsilon(m_F^g) = g_F^g m_F^g \mu_B B \tag{4.12}$$

The intermediate state $\{5P_{\frac{3}{2}}, F' = 3\}$ has 7 Zeeman sub-levels with energy

$$\varepsilon(m_F^e) = \epsilon_{g,e} + g_F^e m_F^e \mu_B B \tag{4.13}$$

$\varepsilon_{g,e}$ is energy of the intermediate state with respect to the ground state at 'B'=0. μ_B is the Bohr magneton, g_F is the Lande g-factor. However, for the Rydberg state ($n \geq 30$), a magnetic field of approximately 1 G is sufficient to decouple the interaction between the nuclear spin $I = \frac{3}{2}$ and the electron's angular momentum $J = \frac{1}{2}$. In other words, the hyperfine states $F'' = 1$ and $F'' = 2$ are combined to form the $|m_I, m_J\rangle$ state.

This effect is referred to as the 'Paschen-Back' effect. This 'Paschen-Back' effect gives $(2I + 1)(2J + 1) = 8$ sub-levels $|m_I^r, m_J^r\rangle$ with energies (see expression (4.4))

$$\varepsilon(m_I^r, m_J^r) = \varepsilon_{g,r} + A_{\text{hfs}} m_I^r m_J^r + (g_I^r m_I^r + g_J^r m_J^r)\mu_B B \tag{4.14}$$

where $\varepsilon_{g,r}$ is the energy of the Rydberg state with respect to the ground state at 'B'=0. A_{hfs} is the hyperfine interaction energy .

Figure 4.7 shows pictorially the Zeeman splitting of all states, excitation pathways for different circular polarization combination of the probe and the coupling laser beams and the incoherent decay pathways to the ground state.

In this case, the Lindblad master Eq. (2.1) is used to solve the coupling Hamiltonian numerically. The only difference is that instead of a three-level Hamiltonian,

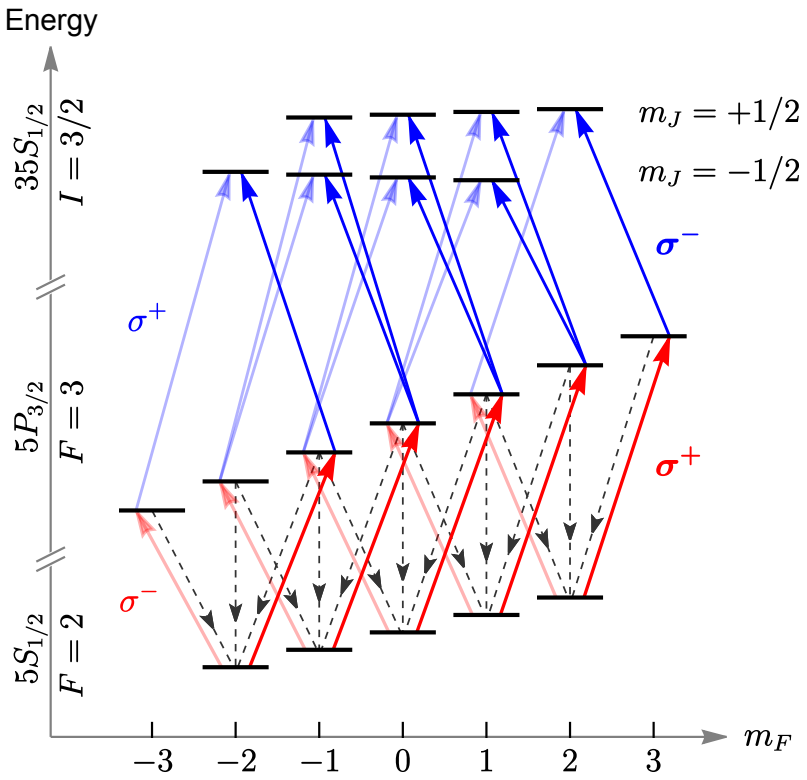


Figure 4.7: Energy-level diagram showing the ground manifold $\{5S_{1/2}, F = 2\}$, the excited manifold $\{5P_{3/2}, F' = 3\}$, and the Rydberg manifold $\{35S_{1/2}, I = 3/2\}$ of ^{87}Rb in the presence of a magnetic field. The red and blue arrows denote coherent pumping by the probe and coupling lasers, respectively, for $\sigma^{\pm}$ polarizations. The dashed lines represent incoherent decay of the excited states back to the ground manifold.

the new Hamiltonian will be a 20×20 matrix (5 sub-levels for the ground state $\{5S_{\frac{1}{2}}, F = 2\}$ with $m_F^g \in \{-2, \ldots, 2\}$, 7 sub-levels for the excited state $\{5P_{\frac{1}{2}}, F = 3\}$ with $m_F^e \in \{-3, \ldots, +3\}$ and 8 sub-levels for the Rydberg states $\{35S_{\frac{1}{2}}\}$ with $m_I \in \{\pm\frac{1}{2}, \pm\frac{3}{2}\}$,$m_J \in \{\pm\frac{1}{2}\}$. So the coefficient matrix M is a 400×400 matrix. The optical drive competes with the spontaneous decay of the excited state to the ground state, which occures on a time scale of approximately 0.1 μs. All the radiative decay channels are shown in figure 4.7. m_F changes by 0 or ± 1 with different branching ratio. All these branching ratios and dipole matrix elements contributing to the Rabi frequencies are calculated using the `ARC` library [99]. Another thing to note is that the Rydberg levels have a lifetime of $\approx 20\mu s$ which does not effect the steady state significantly [61].

In the laser frame (rotating frame), the time-independent Hamiltonian with re-

scaled energies can be written as $\varepsilon_\circ(m_F^g) = \varepsilon(m_F^g)$, $\varepsilon_\circ(m_F^e) = g_F^e m_F^e \mu_B B - \Delta_p$, and $\varepsilon_\circ(m_I^r, m_J^r) = (g_I^r m_I^r + g_J^r m_J^r)\mu_B B + A_{\rm hfs}(m_I^r m_J^r - 3/4) - \Delta_p - \Delta_c$, where $\Delta_p := \hbar\omega_p - \varepsilon_{g,e}$ is the detuning of the probe laser and $\Delta_c := \hbar\omega_c + \varepsilon_{g,e} - \varepsilon_{g,r} - (3/4)A_{\rm hfs}$ is the detuning of the coupling laser, defined with respect to the $F'' = 2$ Rydberg level at $B = 0$.

The value of $A_{\rm hfs} = 2\pi$ 573 kHz [100] for $35S_{\frac{1}{2}}$ state, so $A_{\rm hfs} m_I m_J$ and $\frac{3}{4}A_{\rm hfs}$ are negligible compared to $\mu_B B$ (μ_B=1.399 MHz/G [95]). Due to the Zeeman splitting of all the sublevels, the effective detuning for the probe beam is

$$\Delta_p^{eff} = g_F^g m_F^g B\mu_B + \Delta_p - g_F^e m_F^e B\mu_B \tag{4.15}$$

and the effective detuning for the coupling beam is

$$\Delta_c^{eff} = g_F^e m_F^e B\mu_B + \Delta_c - g_J^r m_J^r B\mu_B. \tag{4.16}$$

As $g_J^r = 2$ and $g_I^r = -.001$ [101], $g_J^r m_J^r \gg g_I^r m_I^r$ so $g_I^r m_I^r$ term is neglected in expression (4.16).

Hence, the condition for the transmission peak is (same as Eq. (4.11)) $\Delta_p^{eff} = \mp\frac{\omega_p}{\omega_c}\Delta_c^{eff}$, which gives

$$\Delta_p(B) = g_F^e m_F^e B\mu_B - g_F^g m_F^g B\mu_B \mp \frac{\omega_p}{\omega_c}(\Delta_c + g_F^e m_F^e B\mu_B - g_J^r m_J^r B\mu_B). \tag{4.17}$$

In general, the peak varies linearly with the magnetic field as

$$\frac{\partial\Delta_p(B)}{\partial(B\mu_B)} = g_F^e m_F^e - g_F^g m_F^g \mp \frac{\omega_p}{\omega_c}(g_F^e m_F^e - g_J^r m_J^r). \tag{4.18}$$

For the probe-coupling $\sigma^+ - \sigma^-$ configuration as in figure 4.7, optical drive and the loss mechanism bring the atoms in the manifold of $|m_F^g = 2\rangle$,$|m_F^e = 3\rangle$ and $|m_I = \frac{3}{2}, m_J = \frac{1}{2}\rangle$, so in the steady state, the effective system reduces to a three-level system. The two-photon condition is now a function of the magnetic field (B) as it is clear from Eq. (4.17) and varies linearly with the magnetic field.

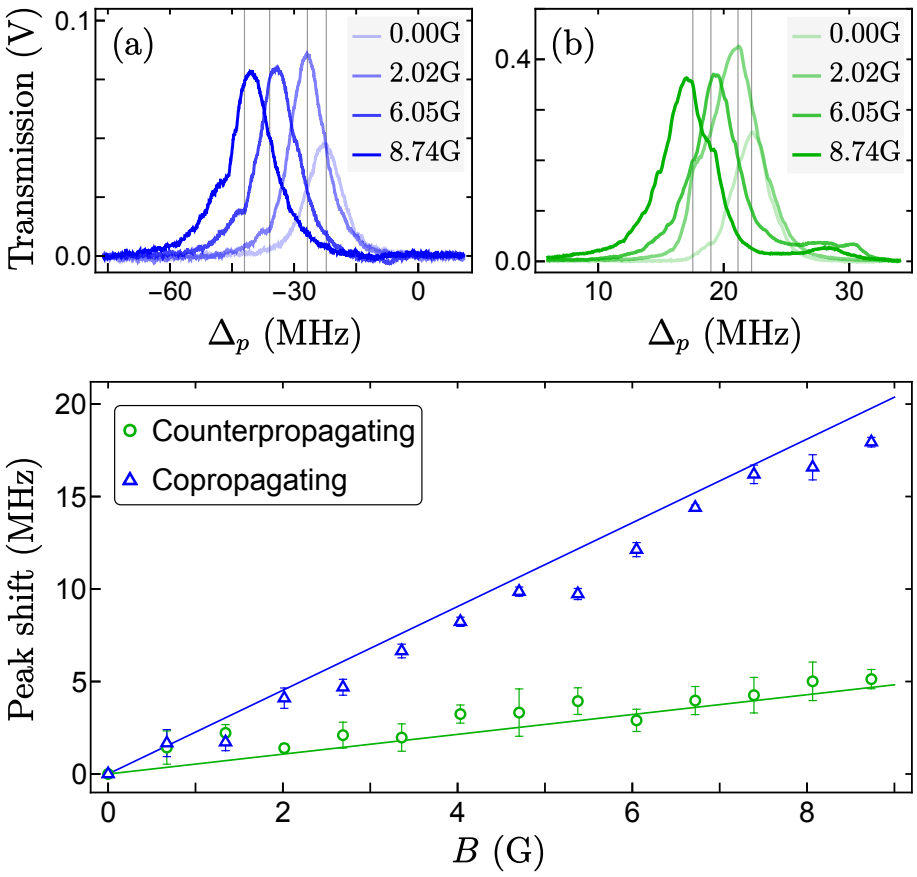


Figure 4.8: Top: Measurements showing the variation of the EIT signal with B for σ^--σ^+ polarizations and $\Delta_c = -36$ MHz for (a) copropagating and (b) counter-propagating lasers. Vertical lines show the predicted peak locations at $\Delta_p(B)$ given by Eq. (4.17). Bottom: Displacement of the fitted peaks with B. Solid lines show theoretical predictions.

So from Eq.(4.17) and Eq. (4.18) we get,

$$\Delta_p(B) = \mp\frac{\omega_p}{\omega_c}\Delta_c + B\mu_B(1 \mp \frac{\omega_c}{\omega_c}) \tag{4.19}$$

and $\frac{\partial\Delta_p(B)}{\partial(B\mu_B)} = (1 \mp \frac{\omega_p}{\omega_c})$.

Similarly, for probe-coupling polarizations $\sigma^- - \sigma^+$, the drive and the loss mechanism bring the atoms in the manifold of $|m_F^g = -2\rangle$, $|m_F^e = -3\rangle$ and $|m_I = -\frac{3}{2}, m_J = -\frac{1}{2}\rangle$. Putting this values in Eq. (4.17) and Eq. (4.18) we get, $\Delta_p(B) = \mp\frac{\omega_p}{\omega_c}\Delta_c - B\mu_B(1 \mp \frac{\omega_c}{\omega_c})$ and $\frac{\partial\Delta_p(B)}{\partial(B\mu_B)} = -(1 \mp \frac{\omega_p}{\omega_c})$. Therefore, as the magnetic field (B) is varied, the peak for the co-propagating case moves faster than that of the counter-propagating case by a factor of $\frac{\omega_p+\omega_c}{\omega_p-\omega_c} \approx 4.2$, as shown in figure 4.8. The top part of the figure shows measurements of the variation of the co-propagating (blue, left-side)

and counter-propagating (green, right-side) EIT signals with the magnetic field for the probe-coupling polarizations of $\sigma^- - \sigma^+$ configuration ($\Delta_c = -36$ MHz). The bottom figure shows the experimental (dotted) observations and theoretical (solid lines) studies of the EIT peak variations with the magnetic field. The main difference between $\sigma^+ - \sigma^-$ and $\sigma^- - \sigma^+$ is that their peaks are shifted in opposite directions under the influence of the magnetic field.

For $\sigma^+ - \sigma^+$ or $\sigma^- - \sigma^-$ polarization configurations of the probe and the coupling beams, there is no EIT peak as the two-photon excitation pathways are not connecting from the ground states to the excited states, as clear from Fig.4.7.

Fig.4.9 shows the case for linear-linear polarizations which are perpendicular to the magnetic field. The polarization perpendicular to the magnetic field can be taken as a linear combination of two opposite circular polarizations. This gives rise to two effective probe-coupling $\sigma^{\pm} - \sigma^{\mp}$ combinations that create two EIT pathways for each type of EIT configuration. So, $\sigma^+ - \sigma^-$ corresponds to the $|m_F^g = 2\rangle$, $|m_F^e = 3\rangle$ and $|m_I = \frac{3}{2}, m_J = \frac{1}{2}\rangle$ manifold, and $\sigma^- - \sigma^+$ corresponds to $|m_F^g = -2\rangle$, $|m_F^e = -3\rangle$ and $|m_I = -\frac{3}{2}, m_J = -\frac{1}{2}\rangle$ manifold. Hence the peak to peak separation given by equation (4.17) is given by

$$\Delta_{pp} = 2(1 \mp \frac{\omega_p}{\omega_c})B\mu_B \tag{4.20}$$

hence, the ratio of the co-propagating to the counter-propagating case peak to peak separation is magnified by $\frac{\omega_p+\omega_c}{\omega_p-\omega_c} \approx 4.2$.

We attribute the slight mismatch between the predicted and the measured peak locations for the counter-propagating case to a slow frequency drift of the lasers. The simulation results for various probe and coupling laser polarizations are presented in appendix C.

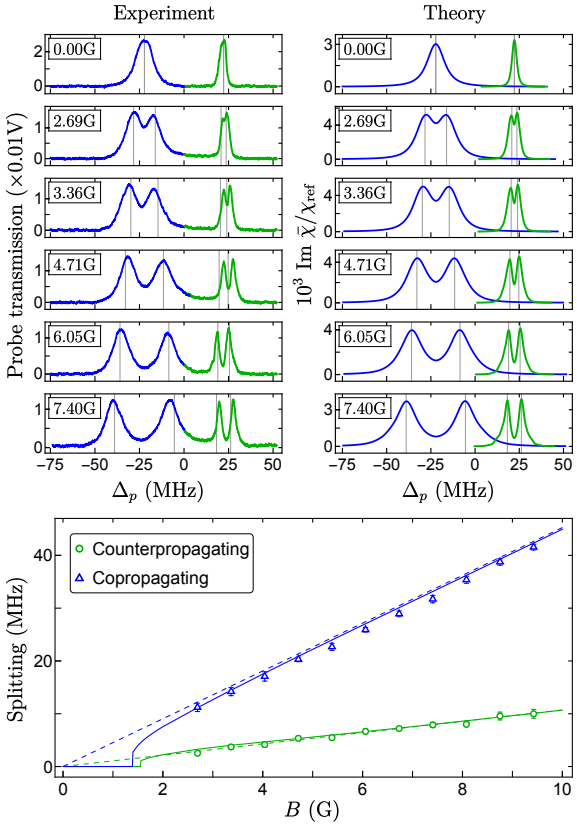


Figure 4.9: Top: Measurements (left) and simulations (right) for increasing B with $\Delta_c = -36$ MHz and x-x polarizations. As before, green and blue curves stand for counter- and copropagating cases. Vertical lines show $\Delta_p(\pm B)$ from Eq. (4.19) . Measurements are averaged over x-x and y-y polarizations to correct for any misalignment of lasers. As in Fig. 4.6, $\bar{\chi}$ for the copropagating case is enlarged by a factor of 3. Bottom: Fitted peak separation as a function of B, showing an enhanced response for copropagating lasers. Solid lines are numerical fits and dashed lines are predicted using Eq. (4.19)

4.5 Conclusion

We have performed Quantum magnetometry with ^{87}Rb atoms using the Rydberg EIT scheme in a ladder-type three-level system. We have shown that in contrast to the existing conventional counter-propagating Rydberg EIT configuration to minimize the Doppler effect, it is possible to leverage the Doppler effect in co-propagating configuration to obtain a greatly enhanced response to the magnetic field. This enhanced response depends on the ratio of their frequencies, which could be varied by targeting different energy levels or different atoms. Our measurements align well with the theoretical modeling derived from the Lindblad master equation. We have used one-dimensional geometry with the magnetic field along the axial direction.

It would be interesting to explore whether varying the relative orientation of the magnetic field with respect to the probe and the coupling directions could lead to any significant effects. One limitation of the current approach is that the peak for the co-propagating case is broader than the counter-propagating case which limits the resolution of the measurement. It would be intriguing to explore the potential methods to reduce the the linewidth of the broadened signal. One of the possibilities would be to use higher order Laguerre-Gaussian coupling beam [102] instead of a pure Gaussian beam. Our results provide strong motivation for the development in quantum sensing [103, 104] and quantum magnetometry with field-deployable Rydberg atoms at room temperature.

CHAPTER 5

Experimental setup for cooling and trapping atoms

The ground-breaking advancements in spectroscopy, cooling and trapping of neutral atoms, and quantum computing began after the invention of Lasers in the 1960s. The first proposal of Laser cooling of neutral atoms, known as Doppler cooling, later known as optical molasses, was developed by Hansch and Schawlow in 1975 [105]. The first experimental achievement of Doppler cooling was demonstrated by Steven Chu in 1985 [106, 107] at Bell Labs. The Doppler cooling mechanism alone was not useful for trapping atoms, so they combined magnetic field and optical molasses to create Magneto-Optical Trap (MOT) [108]. Around the same time, another group led by W. Philips at NBS (later known as NIST) surprisingly discovered a technique named as sub-Doppler cooling [109] where the temperature of the cooled atoms can go well below the Doppler limit. This was done while measuring the temperature of optical molasses by a newly developed technique called the Time of Flight (TOF) technique. Steven Chu, Claude Cohen-Tannoudji, and William D. Phillips were awarded the Nobel Prize in Physics in 1997 [110] for this ground-breaking achievement in cooling and trapping of neutral atoms. This chapter provides an overview of the experimental setup and techniques which are built in our lab, including a comprehensive discussion of the MOT and it's characterization, as well as a discussion

on sub-Doppler cooling and dipole trapping.

5.1 Trapping and cooling of ^{87}Rb atom

In this section, first I will discuss the basic working principal behind the operation of the MOT to cool and trap the atoms with a simple atomic-level structure. Then I will describe our experimental setup and its characterization.

5.1.1 Principle of Magneto-Optical Trap (MOT)

Three-dimensional optical molasses can be turned into a trap by proper choice of laser polarization and inhomogeneous magnetic field. A pair of coils in an anti-Helmholtz configuration is used to generate an inhomogeneous magnetic field, as shown in Fig.5.1. The magnetic field at the center between the coils will be zero. The magnetic field gradient close to the center will be uniform. As result of this, Zeeman effect causes the splitting of the $(F = 1)$ level into $m_F = \pm 1,0$ sub-levels, as shown in Fig.5.1a).

Let us consider the one-dimensional case where the counter-propagating, circularly polarized, red-detuned beams are aligned along the z-axis. For $z > 0$, $\Delta m_F = -1$ transition becomes resonant with the laser beam and the selection rule allows the transition from the σ^- beam. As a result of the absorption, the scattering force pushes the atom towards the trap center i.e at magnetic field (B) = 0. A similar process will happen for the case $z < 0$, but this time absorption from σ^+ laser beam will generate a scattering force (corresponding to $\Delta m_F = +1$) that pushes the atom towards the trap center. The quantization axis is defined along the z-axis, so for the case $z > 0$ the magnetic field has the same direction as the quantization axis. But for $z < 0$ case, the direction of magnetic field is opposite to the quantization axis, that is why the $m_F = -1$ sublevel lies above $m_F = +1$ sublevel. Mathematically, [95, 111], $F_{MOT} = F^{\sigma^+}_{scatt}(\Delta_+) - F^{\sigma^-}_{scatt}(\Delta_-)$, where $\Delta_\pm = \Delta \mp k.v \pm \frac{\mu' B}{\hbar}$, $\mu' = (g^e_F m^e_F - g^g_F m^g_F)\mu_B$. So the resulting force is

$$F_{MOT} = -\beta v - kz \tag{5.1}$$

where the damping coefficient is

$$\beta = \frac{\hbar k^2 \Delta s_0}{\Gamma(1 + s_0 + (\frac{2\Delta}{\Gamma})^2)^2}. \tag{5.2}$$

The spring constant κ is defined as,

$$\kappa = \frac{\mu' \frac{dB}{dz}}{\hbar k} \beta. \tag{5.3}$$

The equation (5.1) is basically an equation for a damped harmonic oscillator, with

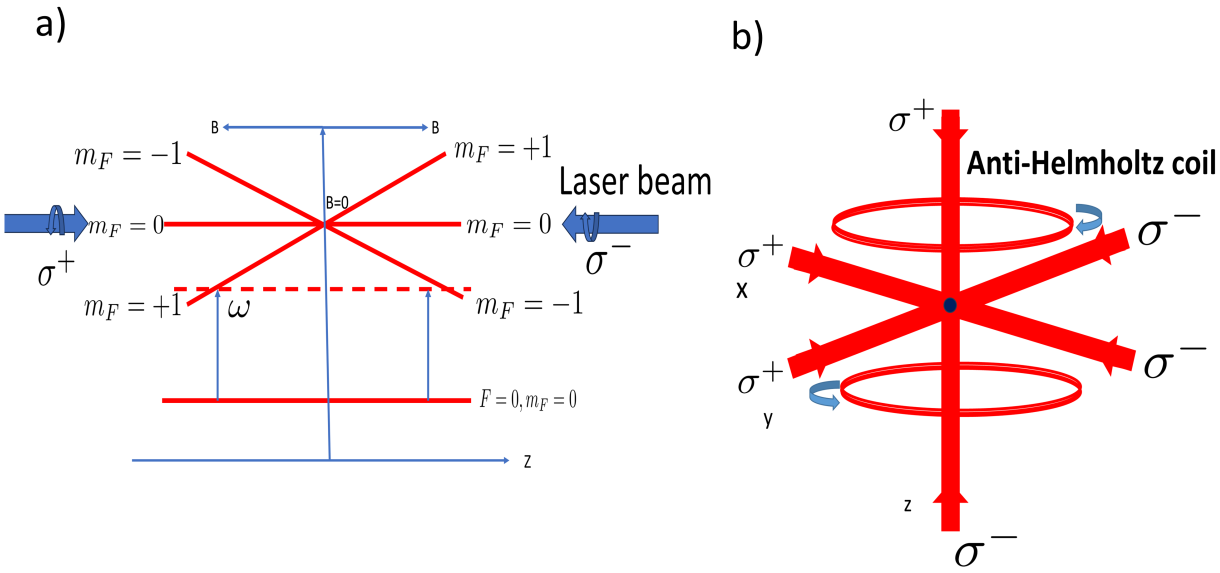


Figure 5.1: a) The Mechanism of the MOT shown for $F = 0$ and $F = 1$ total angular momentum states. The Zeeman splitting of the F levels is also shown. Two counter-propagated circular polarized laser beams of opposite helicity are used create a magnto-optical force for trapping atoms. b) showing the design of the MOT where the three pairs of counter-propagated beams with correct circular polarization are aligned so that they intersect at the center where magnetic field is zero.

the magnetic gradient $\frac{dB}{dZ}$ around 10 G/cm, the oscillating frequency ($\sqrt{\frac{\kappa}{M}}$) is typically few kHz and the damping coefficient ($\sqrt{\frac{\beta}{M}} \approx$ hundreds of kHz) is much larger than the oscillating frequency. So the equation of motion (5.1) becomes over-damped. The above-mentioned idea can be extended to two other orthogonal

directions (x and y) to efficiently cool and trap the atoms.

In this configuration, the axis of the anti-Helmholtz coil is kept along the z-axis while the laser beams are aligned along the x, y and z-directions. The magnetic field of the anti-Helholtz coil near the center is $B(r) = \frac{dB}{dz}(\frac{x}{2}, \frac{y}{2}, -z)$. Because of this magnetic field distribution, the helicity of x and y beams will be opposite to that of the z-direction beam, as shown in the figure. The temperature of the trapped atoms in the MOT is comparable to the temperature attained in the optical molasses. While simple Doppler cooling predicted minimum MOT temperature to be $T_D = \frac{\hbar\Gamma}{2K_B}$, however for multi-level ground states at certain conditions, the temperature of the atoms can be achieved below the given Doppler cooling limit. This process is called sub-Doppler cooling that will be discussed later in this chapter.

5.1.2 Experimental setup of the MOT

The trapping mechanism of the MOT is described in the above section. To realize it experimentally, another important component required is an ultra-high vacuum system to enhance the trap life-time and cooling efficiency.

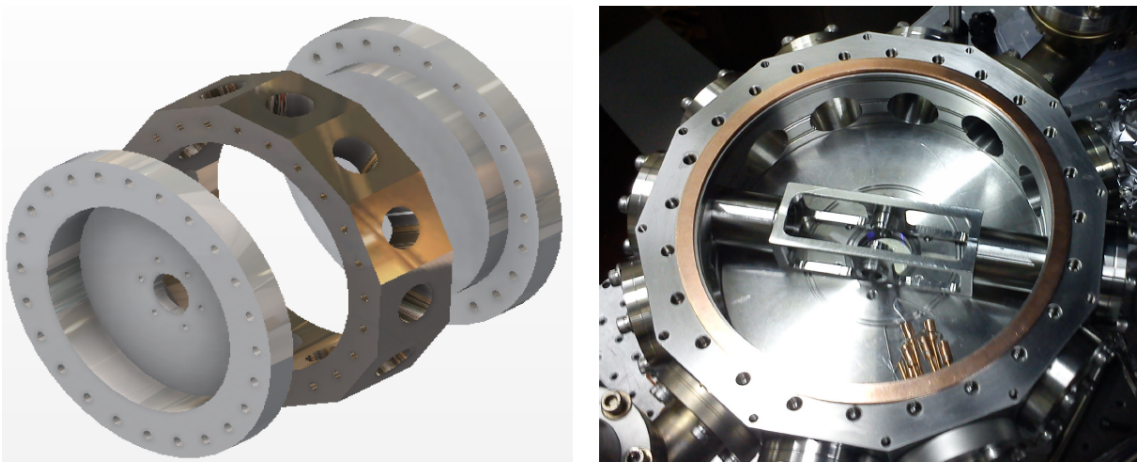


Figure 5.2: Dodecagon vacuum chmaber with twelve view ports, high numerical aperture lens system built inside it.

We have a custom made non-magnetic stainless steel chamber in dodecagon shape with twelve viewports along the circumference, as shown in Fig. 5.3 . Other two viewports are at the top and bottom flanges to accommodate the anti-Helmholtz coil. Our system is designed for single atom trapping and fluorescence detection. For

this purpose, a pair of high numerical aperture lenses are placed inside the vacuum chamber. After the baking process, pressure inside the vacuum chamber is around $\approx 10^{-10}$ mbar. An ion pump from Varian-Diode 9191213 with pumping capacity 40 l/s is connected to the vacuum chamber to maintain this. An ion gauge (Varian-UHV-24) is installed to one of the viewports to measure the vacuum pressure.

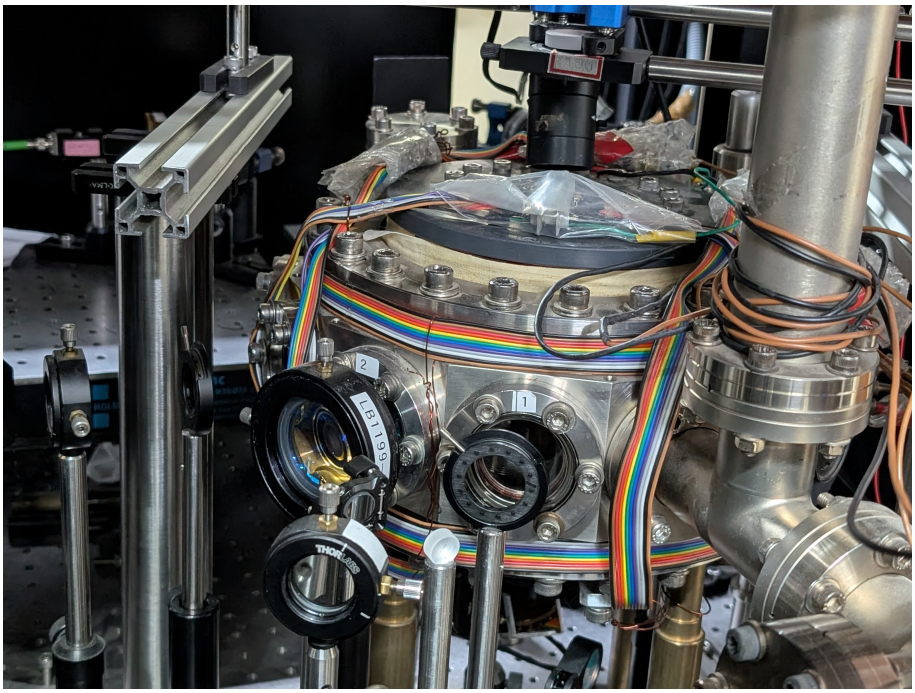


Figure 5.3: Vacuum chamber used for our experiment

Anti-helmholtz coil

The anti-Helmholtz coil used in our setup is made of 18 gauge insulated copper wire. The frame where copper wires are winded has inner radius of 4 cm and outer radius 8.3 cm. Each coil has 26X26 windings along the radial and the axial directions. Each coil has a resistance of 5 ohms and inductance of 30 mH. The switching on and off time of the coils are 2 ms and 400 μs respectively. The anti-Helmholtz coil can generate a magnetic field gradient of 10 G/cm/A.

Compensation coil

Three pairs of coils are used in the Helmholtz configuration along the three perpendicular directions to generate an uniform magnetic field in the trapping region. This

configuration is used to cancel any external residual magnetic field due to a locally induced magnetic field or the Earth's magnetic field. Any one of the pairs can be used to set the direction of the quantization axis for the experiment. These coils are made of standard ribbon strips (see Fig.5.3) with 10 side-by-side wires, which can generate a magnetic field of 1 Gauss at 1 Ampere current near the center of the MOT.

Cooling Laser system for ^{87}Rb MOT

We are using ^{87}Rb [95] atoms for our experiment as it has a simple electronic level structure, relatively high vapor pressure at relatively low temperature and easy availability of lasers for cooling and trapping. The level diagram used in the MOT are shown in Fig.5.4. The cyclic transition is needed for the continuous absorption and emission process to obtain an efficient cooling and trapping. The cooling laser is derived from a Toptica DL100 laser and tuned to the cyclic transition from $\{5S_{\frac{1}{2}}, F = 2\}$ to $\{5P_{\frac{3}{2}}, F' = 3\}$ state. The cooling laser setup is shown in Fig.5.5.

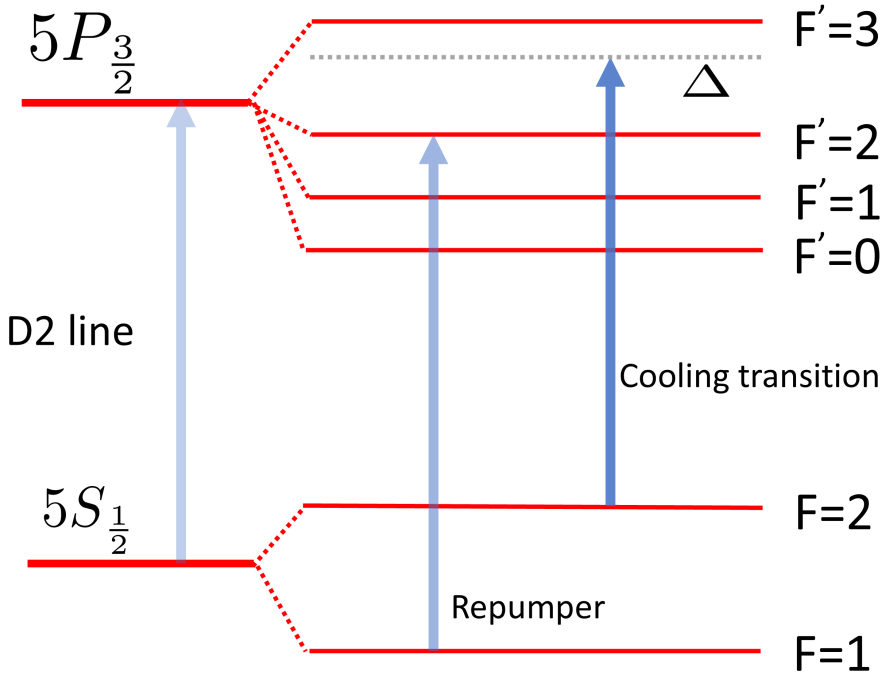


Figure 5.4: Energy level diagram of ^{87}Rb D2 line, $5S_{\frac{1}{2}}$: ground state, $5S_{\frac{3}{2}}$: excited state.

The cooling laser is actively frequency locked to $\{5S_{\frac{1}{2}}, F = 2\}$ to $\{5P_{\frac{3}{2}}, F' = 1 - 3\}$

cross-over of the Saturation absorption Spectroscopy (SAS) signal which is 212 MHz away from the $F' = 3$ cyclic transition. The additional frequency is shifted by an AOM with central frequency of 110 MHz. Typical detuning of the cooling laser is $\approx 2\Gamma$, which is close to 12 MHz (Γ is the natural line width of the $F' = 3$ state). In Fig.5.5, the laser output is taken through the optical isolator, after that the laser is divided into two part by using a HWP ($\frac{\lambda}{2}$ plate) and PBS (Polarizing Beams Splitter). The reflected part is used in the SAS setup for active frequency stabilization, while the transmitted part is sent to the vacuum chamber after passing twice through the AOM where an additional ≈ 200 MHz frequency shift occurs. In double-pass arrangement, at first +1 order diffracted light is sent towards a mirror (M) and is reflected back again towards the AOM by the same mirror (M) for a second pass. At the end of the double pass, the +1 order diffracted light is sent to the experimental table by using a single mode polarization maintaining optical fiber.

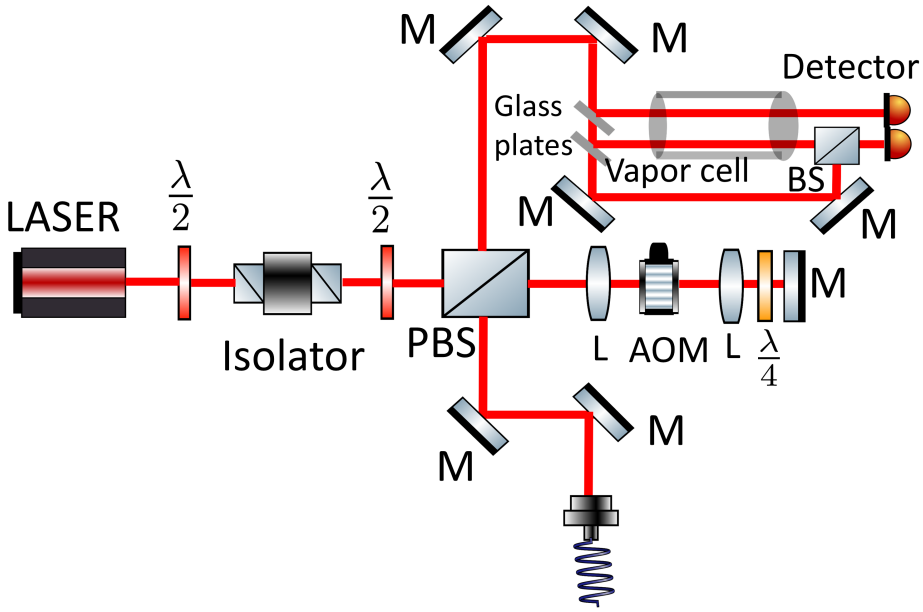


Figure 5.5: Cooling laser setup for the MOT. $\frac{\lambda}{2}$: HWP, $\frac{\lambda}{4}$: QWP, PBS: Polarizing Beam Splitter, M: mirror, BS: Beam Splitter, AOM: Acousto Optic Modulator, L: lens

The QWP ($\frac{\lambda}{4}$ plate in the figure) is used here to control the output power of the double-pass configuration where it is acting as an effective HWP as light passes

twice through it.

Repump laser system

The Repump laser is used to pump the atoms back to the cyclic transition because of various reasons, such as Doppler broadening, and laser linewidth fluctuations, causing the atoms to leak to the $\{5S_{\frac{1}{2}}, F = 1\}$ state. The repump laser is tuned from $\{5S_{\frac{1}{2}}, F = 1\}$ to $\{5SP_{\frac{3}{2}}, F' = 2\}$ transition. The schematic of the repump laser system is shown in Fig.5.6. The laser output is drawn from a Toptica DL100 laser. After the optical isolator, the laser beam is split into two parts with the help of a HWP (Half wave plate) and a PBS. The reflected part is sent to the SAS setup for frequency stabilization, and the transmitted part is sent to an AOM (Brimrose) with 80 MHz central frequency. With the SAS frequency stabilization technique, the repump laser is locked from $\{5S_{\frac{1}{2}}, F = 1\}$ to $\{5P_{\frac{3}{2}}, F' = 1-2\}$ cross-over transition, and additional 72 MHz frequency is shifted by the AOM (acousto optic modulator)

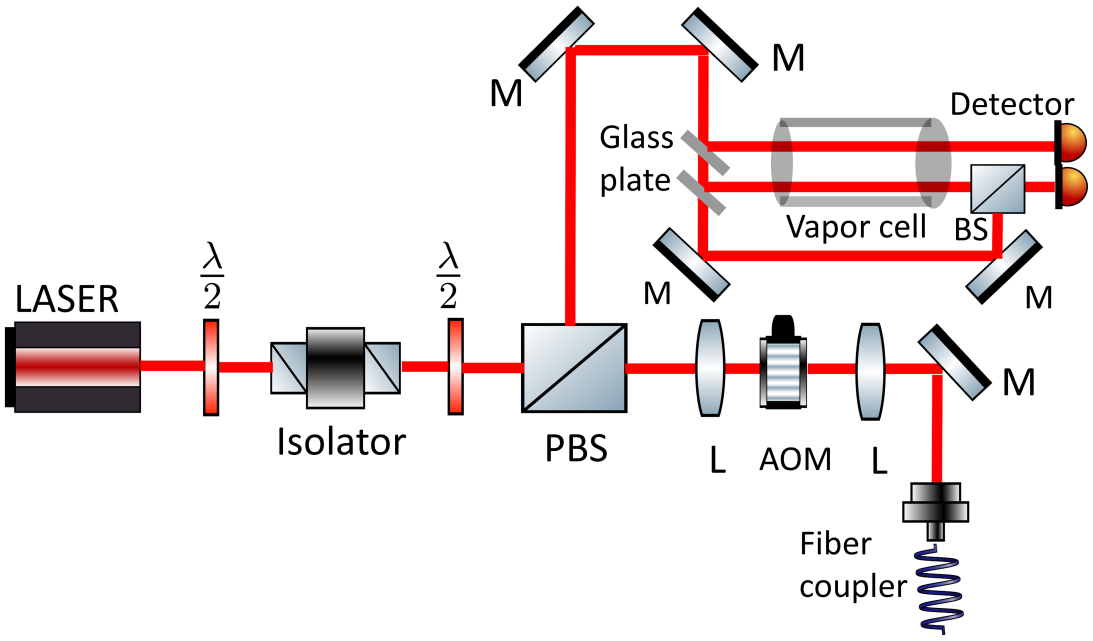


Figure 5.6: Repump laser system for the MOT. $\frac{\lambda}{2}$: HWP, PBS: Polarizing Beam Splitter, BS: Beam Splitter, M: mirror, AOM : Acousto Optic Modulator.

in a single-pass arrangement. The +1 diffracted order is sent to the experimental table through a single mode polarization maintaining fiber. The cooling and the re-pumper SAS signals are shown in Appendix B

5.1.3 Fluorescence Detection setup

Once the atoms are trapped in a MOT, it is important to quantitatively measure the size, temperature, and density of the atomic cloud for further studies in various research areas of atomic physics. The detection setup also helps us to probe different measurements such as atom-atom interactions, excitation dynamics etc. We are using two kinds of fluorescence detection setup as shown in Fig.5.7. One technique uses fluorescence imaging of the MOT cloud using an EMCCD camera, while the other one employs measurements based on an Avalanche Photo Diode (APD). I shall discuss these techniques in the following sections.

Fluorescence imaging setup

We are using fluorescence imaging setup to measure the size, density and temperature of the MOT with the same cooling beams which are used for the cooling and trapping of the atoms in the MOT.

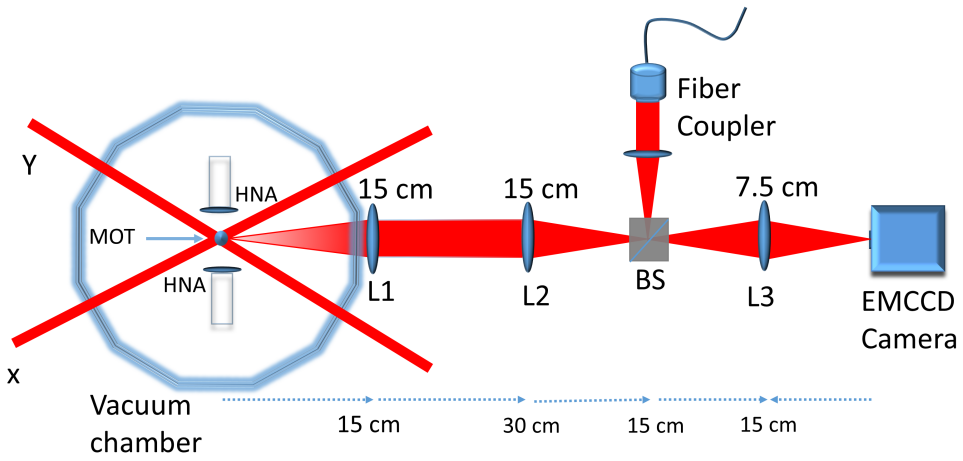


Figure 5.7: Fluorescence imaging setup, L1: lens with focal length 15 cm, L2: lens with focal length 15 cm, L3: lens with focal length 7.5 cm. x,y represent the MOT cooling beams

Since the principal of the MOT is based on absorption and spontaneous emission,

the trapped atom emits photons in the 4π steradian solid-angle. The lens (L1), with a focal length of 15 cm, is placed at 15 cm from the MOT center to collect and collimate the small portion of the fluorescence from the MOT. Another lens (L2), with the same focal length is kept at 30 cm from the L1 lens, focusing the collimated rays onto its focal plane to form an inverted image of the MOT. The lens L3, with a focal length of 7.5 cm, is used in the 2f-2f imaging configuration to image the MOT onto the EMCCD camera. We are using a Photon-MAX 512 EMCCD camera from Princeton Instruments to image the atomic cloud.

APD based detection setup

APD based detection system is used to measure the fluorescence for the experiment discussed in chapter 6. A BS (beam splitter) or a flipper mirror is used in the imaging path (see Fig.5.7) to divert the fluorescence to the fiber coupler. The output of the fiber coupler is sent to an APD (Avalanche photodiode) through a single mode optical fiber. The APD from Excelitas Technologies (SPCM-AQ4C) is used for our detection setup.

5.1.4 Characterization of the MOT

Atom number, density of the MOT

I have discussed about the fluorescence imaging setup in Fig.5.7, we are using this setup to measure the number of atoms, density and temperature of the MOT. The number of atoms in the MOT is calculated by the following formula,

$$N_{atom} = \frac{N_{pixel}}{G\eta R_{scatt}\Omega T\tau_{exp}} \tag{5.4}$$

Where, N_{pixel} is the total pixel counts of the MOT image taken by the EMCCD camera. G is the gain of the EMCCD camera, R_{scatt} is the scattering rate (per second) of the atoms, Ω is solid angle created by the imaging lens (lens L1 in Fig.5.7), the coefficient of transmission T of the imaging system, τ_{exp} is the camera

exposure time. The formula for the photon scattering rate (R_{scatt}) is given as [95],

$$R_{scatt} = \frac{\Gamma}{2} \frac{\frac{I}{I_{sat}}}{1 + \frac{I}{I_{sat}} + 4(\Delta/\Gamma)^2} \tag{5.5}$$

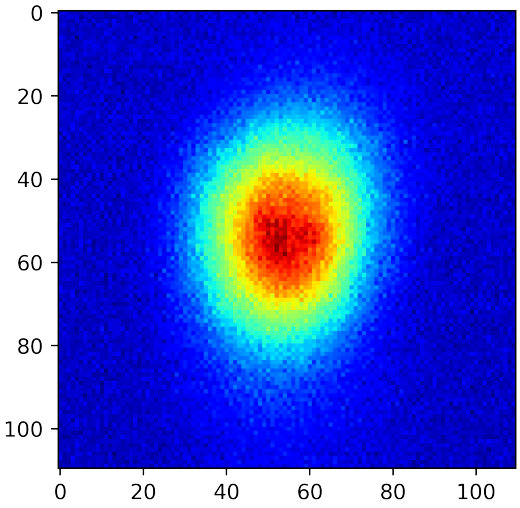


Figure 5.8: Typical image of the atomic cloud in the MOT recorded with an EMCCD camera. The values along the x and y axes are pixel numbers of the EMCCD camera.

The number density of MOT can be estimated by assuming that it has a Gaussian distribution along three perpendicular directions i.e $n(r) = n_0 e^{-x^2/2\sigma_x^2} e^{-y^2/2\sigma_y^2} e^{-z^2/2\sigma_z^2}$. σ_x and σ_y are the $\frac{1}{e}$ radii of the MOT image, which are calculated by fitting the MOT image (see Fig.5.8) from the EMCCD camera. The peak atomic density (n_0) is given as,

$$n_0 = \frac{N_{atom}}{(2\pi)^{3/2}\sigma_x\sigma_y\sigma_z} \tag{5.6}$$

or approximately it can be expressed as

$$n_0 = \frac{N_{atom}}{(2\pi)^{3/2}\sigma^3} \tag{5.7}$$

σ is mean radius of MOT. N_{atom} is the number of atoms in the MOT which is calculated using Eqn.(5.4). The number of atoms and peak atom number density in our MOT are estimated to be approximately 0.75×10^5 and 0.2×10^9 $atoms/cm^3$,

respectively.

The diameters of the MOT along the x and y axes are estimated to be approximately 520 μm and 720 μm, respectively. For density calculation, the MOT diameter along the z-axis is considered to be the average of the diameters along the x and y axes.

Temperature measurement of the MOT

The temperature of cold atomic cloud in the MOT is not defined on the basis of strict thermodynamical sense as MOT is not in equilibrium with its surroundings, rather it is a kinematic temperature, estimated from the velocity distribution of the atoms trapped and cooled in the MOT. There are different ways to measure the MOT temperature, few of them are the release and capture [112] method, time of flight (TOF) method [110, 113] and forced oscillation method [114]. We use an extension of the TOF method called the Ballistic expansion method. In this method, the magneto-optically trapped atoms are allowed to expand freely after switching off the MOT cooling beams and the magnetic field. In the absence of the trap, the evolution of the Gaussian profile of the atom cloud depends on the initial temperature of the MOT. The Gaussian cloud size varies as following,

$$\sigma^2(\tau) = \sigma^2(0) + \frac{k_B T}{M}\tau^2 \tag{5.8}$$

$\sigma(0)$ is the initial MOT atom cloud size. τ=0 is defined as the time when the trap is switched off. τ is the time delay after $\tau = 0$. M is the mass of ^{87}Rb atom. T is the initial MOT atom cloud temperature. We use the fluorescence detection system (see Fig.5.7) and the same cooling beam pairs to record the MOT image at different time delays. The variaton of the $\sigma^2(\tau)$ vs τ^2 is shown in Fig.5.9. Each point in Fig.5.9 is averaged over five images to enhance the signal-to-noise ratio. The MOT temperature is determined by fitting Eqn.(5.8) (red line) in graph 5.9. The MOT atom cloud temperature is estimated to be approximately 120 μK.

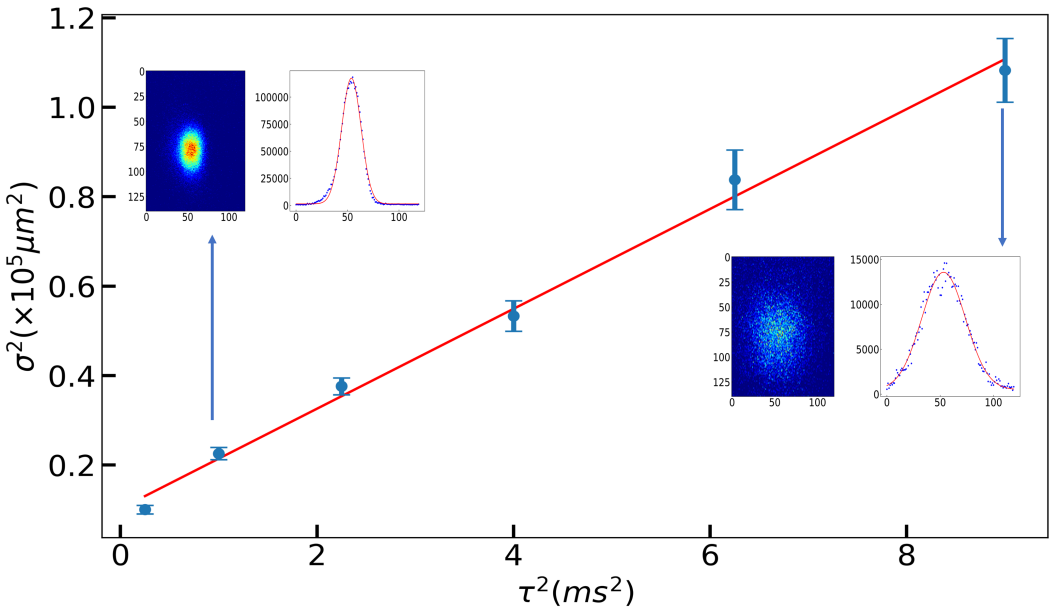


Figure 5.9: σ^2 vs τ^2 plot to determine the MOT atom cloud temperature.

5.1.5 Sub-Doppler cooling

Two years after the first measurement of the molasses temperature that confirmed the Doppler cooling theory, scientists led by Paul D. Lett at NBS [115] measured the molasses temperature below the Doppler limit using the Time-of-Flight method (TOF) after nullifying stray magnetic fields at the center of the molasses. As a new result of the temperature measurement, modifications to the Doppler cooling theory was needed, which then led to the discovery of sub-Doppler cooling. These new mechanisms confirm one common factor that ground state must have degenerate Zeeman sub-levels to allow optical pumping. Other two important factors are the polarization gradients of the cooling laser and light shifts of the Zeeman sub-levels.

Optical pumping

Optical pumping is a process [116] in which the population of the atoms is redistributed over it's Zeeman sub-levels in the presence of local polarized light fields. To understand with a simple example [117], let us consider a multilevel atom with ground state $F_g = 1$ and excited state $F_e = 2$. The Zeeman sub-levels are shown in Fig. 5.10.

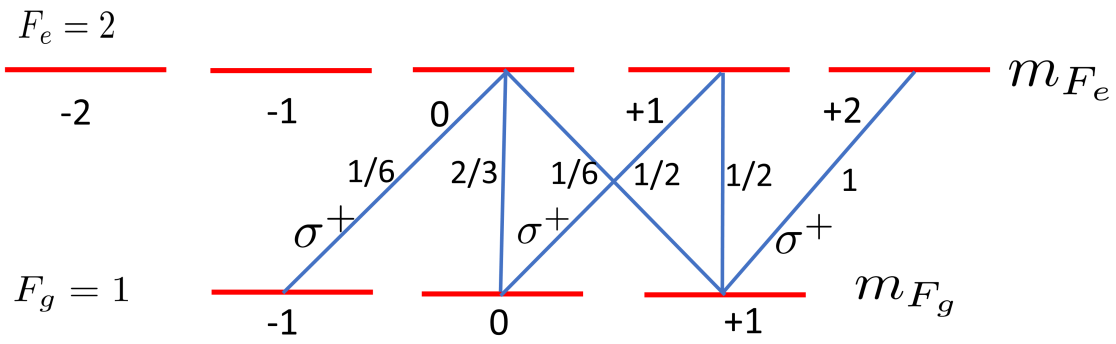


Figure 5.10: Optical pumping in the presence of σ^+ polarized light

With the absorption of σ^+ polarized light, the angular momentum of the atom increases by $+\hbar$. During the following spontaneous emission, the angular momentum changes by $+\hbar$, 0 and $-\hbar$. After a few cycles of absorption and emission, the atom will be pumped to the $m_{g_e} = +1$ state. So the average time taken by the atom to reach this steady state is the called optical pumping time (τ_p), where $\tau_p \approx 1/R_{scatt}$. It is an important parameter in sub-Doppler cooling. We can also estimate the minimum temperature attainable from the Heisenberg uncertainty principle. From this principle, $\Delta E \tau_p \geq \hbar/2$. If T_{min} is the minimum temperature then, $k_B T_{min} \geq R_{scatt}\hbar/2$. For Doppler cooling $\tau = 1/\Gamma$, Γ is natural decay rate of the excited state. τ_p is two orders of magnitude larger than τ. So from the uncertainty principle, it is clear that the temperature achievable in sub-Doppler cooling is lower than what can be achievable in Doppler cooling.

Polarization gradient

Polarization gradient is another important factor in sub-Doppler cooling [117–119]. If two or more plane waves with different wave vectors interfere, then the resultant polarization of the standing wave may change depending on the position, this is called polarization gradient. Here, I shall describe four configurations of plane-wave interference, three out of four patterns are useful for sub-Doppler cooling.

1) **Linear parallel-parallel polarization**: In this case, two counter-propagating plane waves linear polarized along the same direction are interfered.

$$\vec{\epsilon} = \epsilon_0 cos(kz - \omega t)\hat{x} + \epsilon_0 cos(kz + \omega t)\hat{x}$$

$$\vec{\epsilon} = 2\epsilon_0 cos(kz)cos(\omega t)\hat{x} \tag{5.9}$$

2) **Orthogonal or parallel-perpendicular (Sisyphus)**: In this configuration, two counter-propagating plane waves with orthogonal polarization interfere to generate a standing wave.

$$\vec{\epsilon} = \epsilon_0 cos(kz - \omega t)\hat{y} + \epsilon_0 cos(kz + \omega t)\hat{x}$$

$$\vec{\epsilon} = \epsilon_0[(\hat{x} + \hat{y})cos(kz)cos(\omega t) - (\hat{x} - \hat{y})sin(kz)sin(\omega t)] \tag{5.10}$$

3) $\sigma^+ - \sigma^+$ **configuration:** When two plane waves of same circular polarization interfere in a counter-propagating configuration.

$$\vec{\epsilon} = \frac{\epsilon_0}{\sqrt{2}}[\hat{x}cos(kz - \omega t) - \hat{y}sin(kz - \omega t)] + \frac{\epsilon_0}{\sqrt{2}}[\hat{x}cos(kz + wt) + \hat{y}sin(kz + \omega t)]$$

$$\vec{\epsilon} = \frac{\epsilon_0}{\sqrt{2}}cos(kz)[\hat{x}cos(\omega t) + \hat{y}sin(\omega t)] \tag{5.11}$$

4) **Corkscrew cooling or $\sigma^+ - \sigma^-$ configuration**: In this case, two opposite circularly polarized plane waves [119] interfere in a counter-propagating configuration.

$$\vec{\epsilon} = \frac{\epsilon_0}{\sqrt{2}}[\hat{x}cos(kz - \omega t) - \hat{y}sin(kz - \omega t)] + \frac{\epsilon_0}{\sqrt{2}}[\hat{x}cos(kz + wt) - \hat{y}sin(kz + \omega t)]$$

$$\vec{\epsilon} = \frac{\epsilon_0}{\sqrt{2}}[\hat{x}cos(kz) - \hat{y}sin(kz)] \tag{5.12}$$

The configurations in Eqn.(5.10) and (5.12) have polarization gradient that varies on $\approx \frac{\lambda}{4}$ scale, see Fig.5.11. The configuration in (5.11) gives rise to another cooling mechanism called the Magnetically Assisted Sisyphus Effect (MASE) [120]. However, I will discuss about two sub-Doppler cooling mechanisms: Sisyphus cooling and Corkscrew cooling in this thesis.

Light shift

Consider a simple two-level system with an unperturbed ground state and excited state. When an external AC field is applied to the atom, the energy levels experience

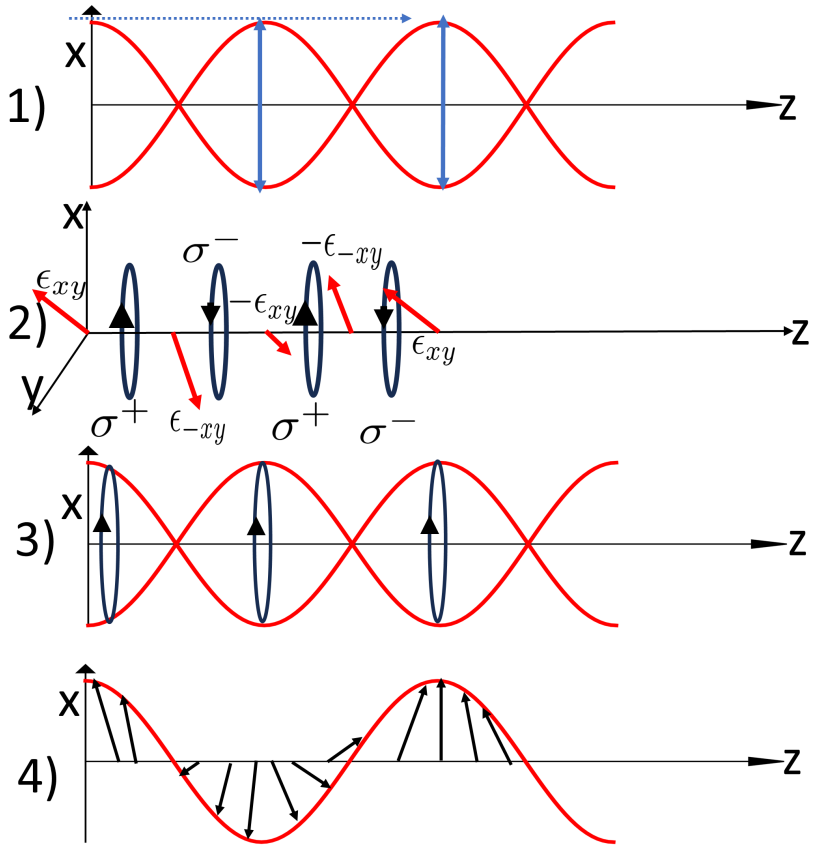


Figure 5.11: 1) standing wave for linear parallel-parallel polarization, (see Eqn.(5.9)). 2) Polarization gradient for Sisyphus cooling, see(Eqn.(5.10)). 3) Standing wave for MASE cooling, see Eqn.(5.11). 4) Polarization gradient for corkscrew cooling mechanism, see Eqn.(5.12)

some energy shift, this is called the light shift or AC stark shift. For detuning, $\Delta \gg \Omega$, the light shifts for the ground and the excited states are approximated by $\Delta E = \pm\frac{\hbar\Omega^2}{4\Delta}$, '+' ('-') sign is indicated for the ground state (excited state). There are two important features of the ground-state light shift: it is negative for red-detuned light, inversely proportional to the detuning, and the shift is proportional to square of the coupling strength.

Sisyphus cooling

Sisyphus cooling is the combined effect of optical pumping, polarization gradient, and light shift. Since the light shift is proportional to the square of the coupling strength (Ω), then the atom with multiple ground state sub-levels will have different

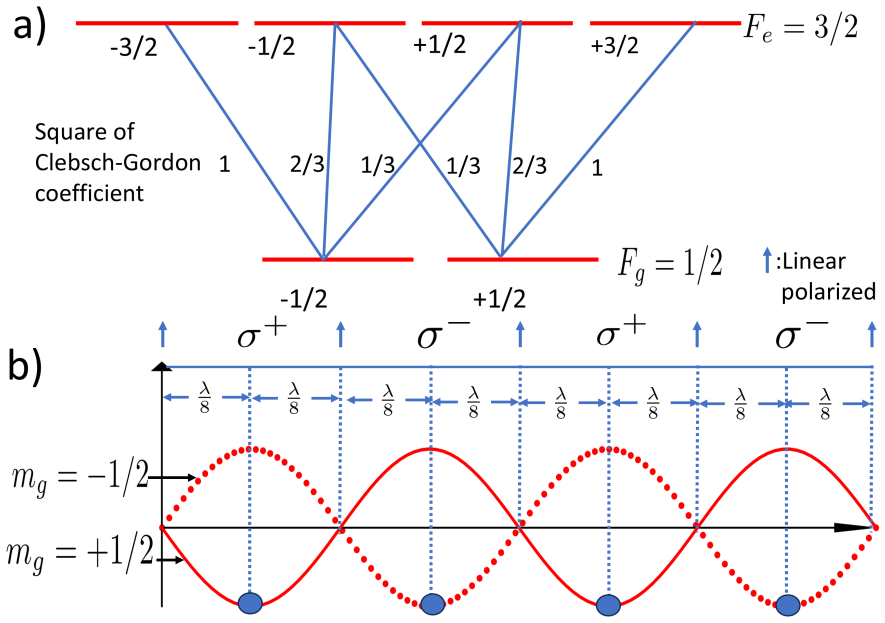


Figure 5.12: a) Zeeman sub-level structure of an atom with ground state $F_g = 1/2$ and excited state $F_e = 3/2$, coupling strength proportional to the square of the Clebsh-Gordon coefficient of that transition. b) Light shifts of ground states due to the polarization gradient. The polarization gradient is set as it is mentioned in 5.112).

shifts in the presence of local polarization gradient.

Let's consider a simple scenario of an atom with a ground state $F_g = 1/2$ and excited state $F_e = 3/2$, where all the Zeeman sub-levels are shown in Fig.5.12a). Polarization gradient is created using two orthogonal linear polarized light with wavelength λ in a counterpropagating configuration (see Fig.5.11)2). The polarization gradient is shown in Fig.5.12a). The two ground states ($m_g = \pm 1/2$) have the same light shifts at the positions where the light is linearly polarized. However, the light shift for $m_g = +1/2$ sub-level at locations where the light is σ^+ polarized is three times higher than that of $m_g = -1/2$ state (see the Clebsh-Gordon coefficients in Fig.5.12a)). For similar reason, the light shift is three times more for the $m_g = -1/2$ state than that of the $m_g = +1/2$ state at locations where the light is σ^- polarized. Optical pumping distributes the atoms among the Zeeman sublevels in τ_p time. In this case, because of the σ^+ (σ^-) polarized light, the atom will be pumped to the $m_g = +1/2$ ($m_g = -1/2$) state. Let us consider an atom with velocity v_p such that $v_p\tau_p = \lambda/4$. If the atom starts moving from $z = \lambda/8$

along the +z direction, the initial state is $m_g = +1/2$, then the atom uses its kinetic energy to climb the potential hill and reaches the location of the polarization σ^- (situated at $2\lambda/8$) in time τ_p. In this process, the kinetic energy is reduced in terms of gaining the potential energy. The atom, at this location with state $m_g = +1/2$ is optically pumped to the $m_g = -1/2$ state due to the presence of σ^- polarization. This way the atom releases its gained potential energy to the light field, effectively transferring its reduced kinetic energy to the light field and the atom prepares for a new cycle. The temperature reached in this process is

$$k_B T = \frac{D_p}{\beta} = \frac{\hbar\Omega^2}{8\Delta} \tag{5.13}$$

[117], D_p [121] is the Sisyphus diffusion coefficient and β is the Sisyphus friction coefficient. The velocity 'v_p' is called the capture velocity and it is directly proportional to the intensity of light. The Sisyphus friction coefficient 'β' is independent of the intensity of the laser. One thing to note is that in Doppler cooling theory the condition reverses i.e Doppler friction coefficient becomes directly proportional to the light intensity and the capture velocity remains independent of the intensity. From Eqn.(5.13), the achieved temperature is proportional to the intensity and inversely proportional to the detuning of the laser.

Corkscrew cooling

This cooling mechanism [117] is different from the Sisyphus cooling, it is the unbalanced scattering force that is responsible for this type of cooling rather than the dipole force that is responsible for Sisyphus cooling. The Fig.5.11 4) illustrates this configuration, where the opposite circular polarized light beams are counter-propagated to produce a standing wave. The polarization configuration of this wave is rotated in a x-y plane with respect to the propagation axis of the original light beams.

However, the amplitude of the standing wave remains the same. As a result, no polarization gradient is formed in this configuration. Even if there is no polarization gradient, the atomic ground states will still have constant light shifts, see Clebsh-

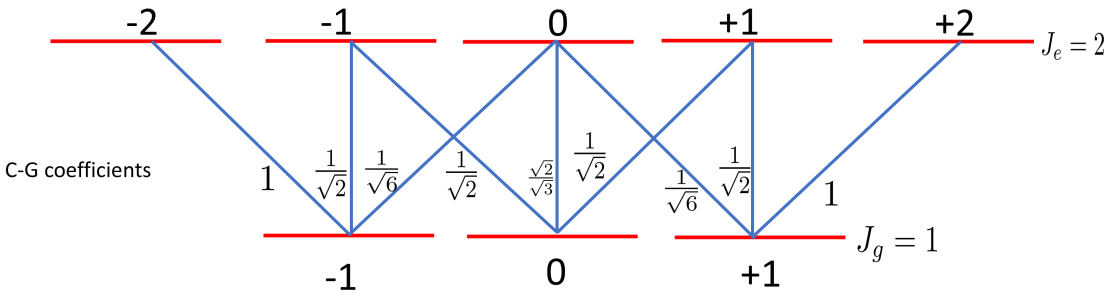


Figure 5.13: Clebsh-Gordon coefficients and transition pathways for $J_g = 1$ and $J_e = 2$

Gordon coefficients in Fig.(5.13). The energy shift in the ground state is $\Delta'_0 = \frac{4}{3}\Delta'_1$. I will explain this effect with an example of an atom in a ground state $J_g = 1$ and an excited state $J_e = 2$. When the atom rests at z=0, let us consider the polarization of the light along the $\hat{y}$ axis, and so the quantization axis. As a result of optical pumping due to π polarization, the ground eigenstates ($|mg_{\pm 1}\rangle_y$) of J_y angular momentum are symmetrically populated with respect to the $|mg_0\rangle_y$ state. If the atom starts moving with velocity v, then $z = vt$. The atom in its rest frame can see the polarization rotating in the x-y plane with an angular speed of kv. After transforming to a frame rotating at the same angular speed, the atom can observe a fixed polarization along the $\hat{y}$ axis. As a result of this moving rotating frame transformation, the atom will experience an additional inertial force apart from the transformed electric field along the $\hat{y}$ direction. The inertial force acts like a fictitious magnetic field along the z direction with Larmor frequency kv. The inertial term contributes to the Hamiltonian as $V_{rot} = kvJ_z$, J_z being the angular momentum along the z-direction. Under certain conditions, $R_{scatt} \ll |\Delta'|$ and $kv \ll |\Delta'|$, the effect of the inertial term can be treated in a perturbative approach. As a result of this perturbation, the population of the new eigen states ($\overline{|mg_{\pm 1,0}\rangle_y}$) will remain the same. However, in the new eigen states, $\overline{|mg_{\pm 1,0}\rangle_y}$, the populations of $|mg_{+1}\rangle_z$ and $|mg_{-1}\rangle_z$, the eigen states of J_z, will not be the same. Therefore, the expected value of J_z in the new perturbed states ($\overline{|mg_{\pm 1,0}\rangle_y}$) will not be zero, this $\langle J_z \rangle$ is called the motion-induced orientation. In simple words, when an atom moves in a rotating polarization field along the z-direction, the states $|mg_{\pm 1}\rangle_z$, the eigen states

of J_z have population imbalance which leads to the unbalanced scattering forces. The detailed calculations of this mechanism are given in this Ref [117]. For large detuning $\Delta \gg \Gamma$, the equilibrium temperature in this cooling mechanism is similar to the temperature that can be achieved in Sisyphus cooling (see Eqn.5.13).

The two sub-Doppler cooling mechanisms discussed above are particular to certain polarization combinations in one-dimensional case. However, in a MOT both kinds of sub-Doppler cooling mechanisms are possible [122].

Experimental results of sub-Doppler cooling:

We have achieved sub-Doppler [123] cooling of atoms in a Magneto-optical trap. The time sequence of the sub-Doppler cooling is shown in Fig.5.14. The imaging system is the same as it is mentioned in Fig.5.7. The temperature also depends on the duration of the sub-Doppler cooling phase [124]. We have found that efficient cooling is happens with sub-Doppler cooling time of around 3 ms. Initially, atoms are loaded in the MOT for 15 seconds, and then they undergo a sub-Doppler cooling phase lasting 3.1 milliseconds. From the Eqn. 5.13, it is clear that lower temperature achievable in sub-Doppler cooling depends on the intensity as well as the detuning of the cooling laser. So the cooling beam intensity has to be reduced and the corresponding detuning of the cooling beam from the atomic transition frequency has to be increased in order to achieve the same. The sub-Doppler cooling phase consists of two stages: in the first stage (called 'S' stage), the detuning of the cooling laser is reduced in one step while maintaining a constant cooling intensity. In the second stage (called the 'R' stage), the detuning remains the same but the cooling intensity is adiabatically ramped down. The 'S' stage lasts for 2.5 ms, while the 'R' stage lasts for 0.6 ms. The intensity is reduced in 15 steps during the 'R' phase. The repumper intensity (I) was kept constant during the sub-Doppler cooling phase. The magnetic field is switched off during the sub-Doppler cooling. The temperature attained in the sub-Doppler cooling is measured using the ballistic expansion technique mentioned in this section. The EMCCD camera and the imaging beam are switched on for 100 μS. We use the same cooling beams (red detuned, -2Γ) and the repumper beam for the imaging beam.

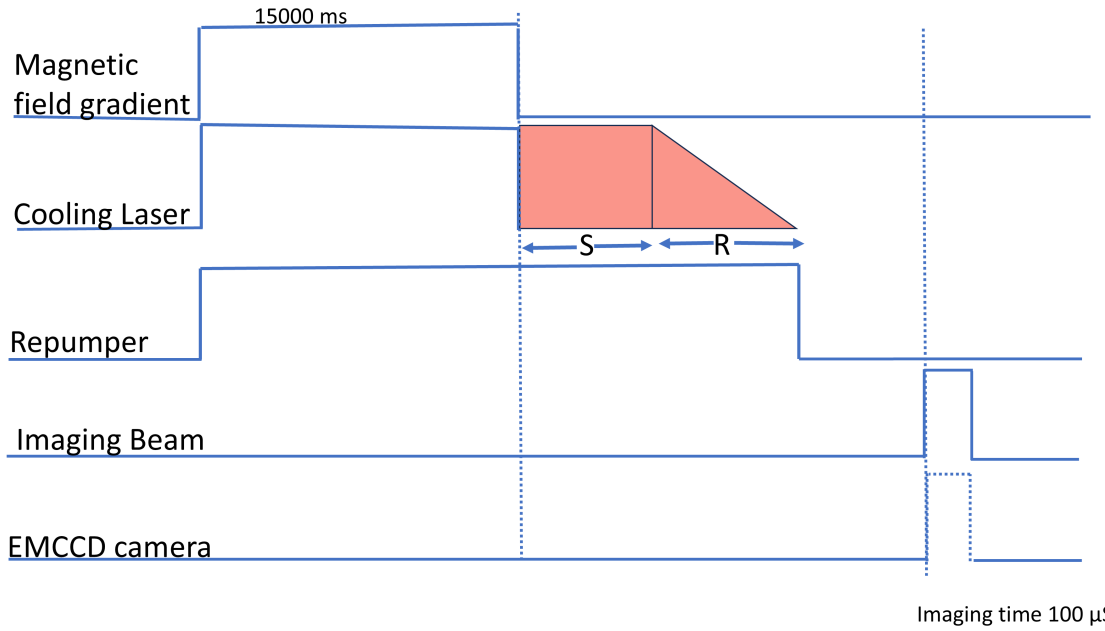


Figure 5.14: Time sequence of sub-Doppler cooling: the 'S' denotes that detuning reduced in one step, the 'R' denotes that the intensity is reduced step by step. In the 'S' stage, cooling intensity remains the same and in the 'R' stage cooling detuning remains the same.

Fig.5.15 shows the temperature variation of the atomic cloud as a function of the cooling beam detuning during the sub-Doppler cooling phase. It shows that the temperature of the atoms reduces from 120 μK to 50μK rapidly when the cooling beam detuning is changed from -2Γ to -5Γ. After that the temperature fluctuates around the steady state value of 40 μK with a detuning upto $= -8\Gamma$. Each data point in the graph is averaged over five repeated measurements.

Fig.5.16 shows σ^2 vs τ^2 graph at the end of the sub-Doppler cooling stage. In this case, the detuning of the cooling beam is reduced to -6.38Γ in the 'S' stage and maintained at the same value in the 'R' stage. The initial intensity at the begining of 'R' stage is approximately 55 I_{sat}. The cooling intensity at the end of the 'R' stage or at the end of the sub-Doppler stage is kept at $9I_{sat}$. At a cooling intensity of $9I_{sat}$ and a detuning of -6.38Γ, we observe that the temperature of the MOT reaches 26 μK. One possible reason that the temperature doesn't reach the minimum value around the cooling intensity of I_{sat} is that the six beams have different intensities and their overlap is not optimal at the MOT center.

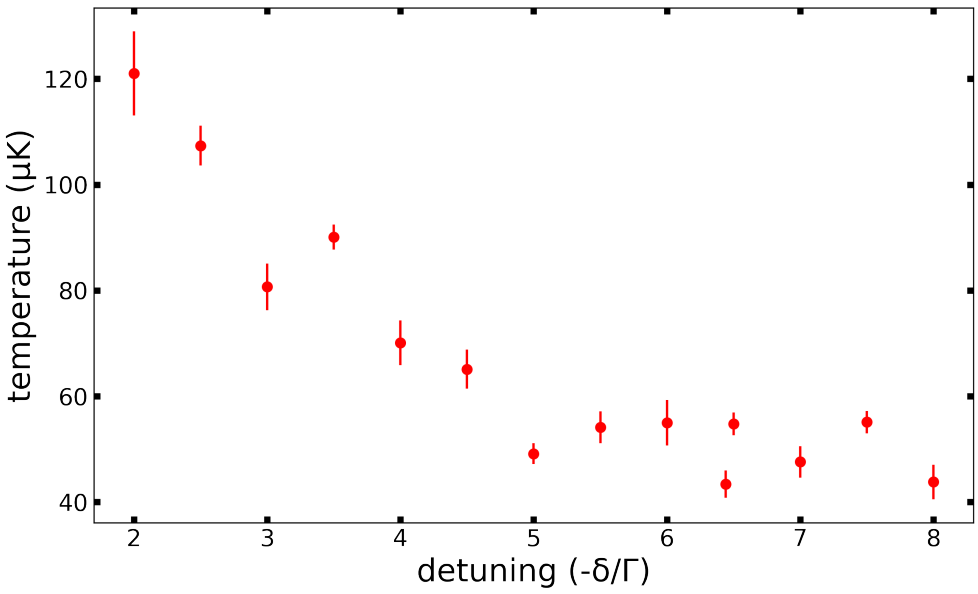


Figure 5.15: Temperature of the atoms vs detuning $(-\delta/\Gamma)$ of the cooling beams during the sub-Doppler cooling phase. The detuning is changed in one step in the 'S' stage and is kept at the same value during the 'R' state. The detuning in the MOT loading phase is kept at -2Γ.

5.2 Far-off resonance Dipole Trap

Optical Dipole trapping is based on the interaction of the atomic dipole with a far-detuned light field. It was first suggested by Ashkin [125] (1970) and later Steven Chu [126] used this technique to trap the neutral atoms (1986). Classically, an atom can be treated as an oscillator and the light can be treated as a continuous wave. The interaction of the atom with light can be analyzed using a forced vibration model. The electric field 'E' of the light will induce a temporary dipole moment $p = \bar{\alpha}E$, $\bar{\alpha}$ is the complex polarizability. Then the induced dipole interacts with the light, and the resultant interaction energy is $-p.E$. The real part of the interaction is the dipole potential, and it is expressed as $V_{dip} = -\frac{Re(\alpha)}{2\epsilon_0 c}I$, I is the intensity of the light, where $I = \frac{\epsilon_0 c E^2}{2}$. The imaginary part of the interaction term contributes to the absorption and scattering process. The scattering process plays a crucial role to influence the performance of the dipole trap. However, the problem with the classical model is that it fails to explain the saturation effects i.e at high intensity the population in the atomic state tends to saturate.

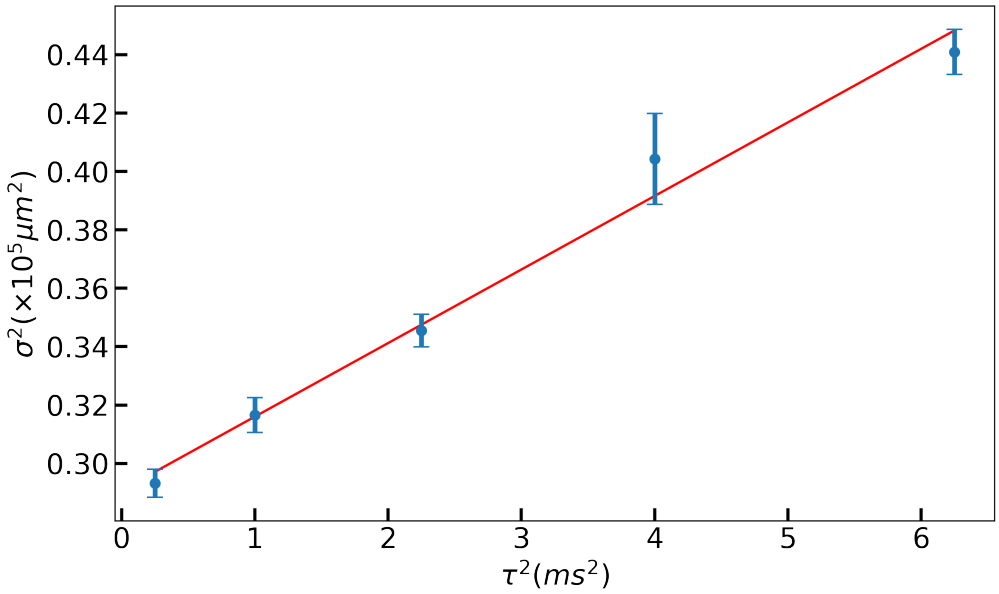


Figure 5.16: σ^2 vs τ^2 plot at sub-Doppler cooling stage.

In the semi-classical approach, atoms are treated quantum mechanically as a simple two-level system and the light is treated as a continuous radiation field. The interaction Hamiltonian is $H_I = -\hat{\mu}E$, $\hat{\mu} = e\hat{r}$, $\hat{\mu}$ is called the dipole operator. The effect of the interaction can be described by a time-independent second-order perturbation theory in the laser frame. The light shift and the scattering rate from the second-order perturbation theory are calculated [21] in terms of the intensity I(r) and the decay rate Γ,

$$\Delta E = \pm \frac{|\langle g|\hat{\mu}.E|e\rangle|^2}{\delta}$$

$$\Delta E = \pm \frac{3\pi c^2}{2\omega_0^3} \frac{\Gamma}{\delta} I(r) \tag{5.14}$$

$$\Gamma_{sc} = \frac{3\pi c^2 \Gamma^2}{2\hbar\omega_0^3 \delta^2} I(r) \tag{5.15}$$

where $\frac{1}{\delta} = \frac{1}{\omega-\omega_0} + \frac{1}{\omega+\omega_0}$

'+' ('-') sign refers to the the ground state (excited state) light-shift. From Eqn.5.14, if $\Delta \ll \omega_0$, then using the rotating wave approximation, $\delta \approx \Delta$. If Δ is red-detuned then from Eqn.5.14 the light-shift will be negative for the ground state

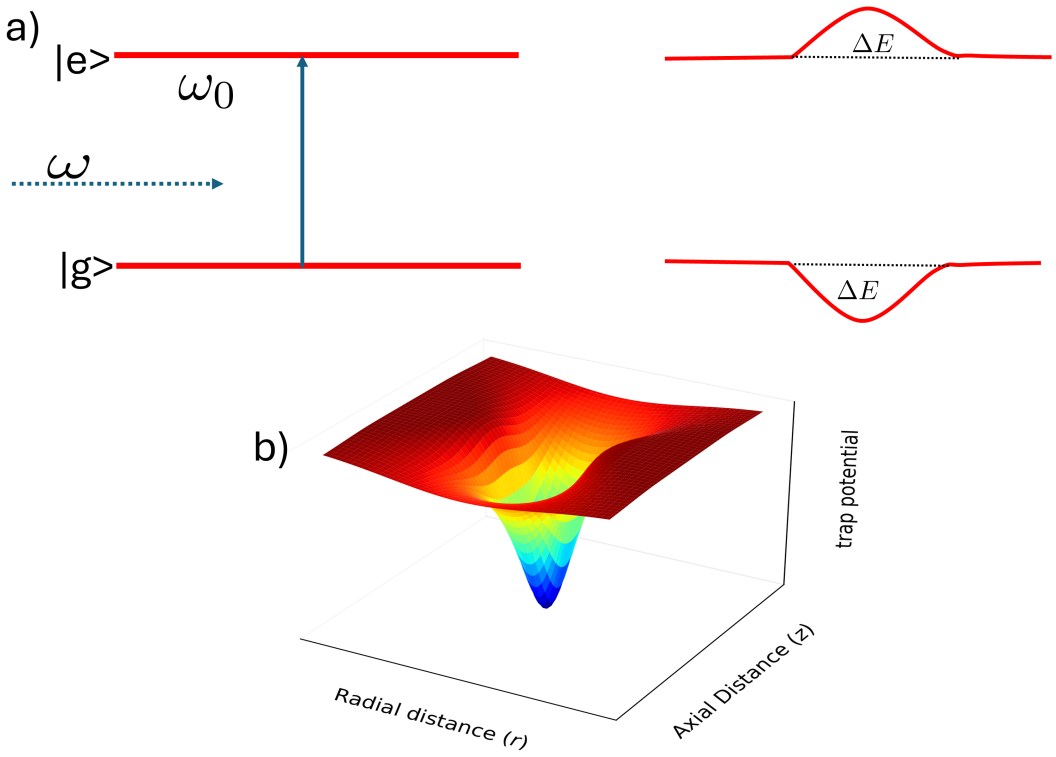


Figure 5.17: a) light-shift for two level system b) 3D visualization of dipole potential.

and positive for the excited state, as shown in Fig.5.17a). The estimated negative light-shift of the ground state (for $\Delta < 0$) is exactly the dipole potential used for trapping the atoms. Another important factor from Eqn.5.15 and Eqn.5.14 is that the dipole potential is scaled as $\propto \frac{I(r)}{\Delta}$, and the scattering rate scaled as $\propto \frac{I(r)}{\Delta^2}$. As the Δ is red-detuned far away from the resonance, the scattering rate reduces by the inverse square of Δ^2 and potential depth increases with decreasing Δ. This is an important factor for the trapping of the atoms, as the scattering rate causes the heating of the trapped atoms and effectively reduces their lifetimes.

Single atom optical dipole trap

We use red-detuned 852 nm (far away from the D1 and D2 transitions of ^{87}Rb) focused Gaussian beam for the single atom trapping. As it is clear from Eqn.5.14 that the dipole potential will be minimum at the maximum intensity, so the atom will be trapped at the focal point. The intensity distribution of the focused Gaussian

beam propagating along the z-axis is given by,

$$I(r,z) = \frac{2P_0}{\pi\omega(z)^2}\exp\left(-\frac{2r^2}{\omega(z)^2}\right) \tag{5.16}$$

where $\omega(z) = \omega_0\sqrt{1+z^2/z_r^2}$, P_0 is the power of the trapping light, ω_0 is the beam waist size at the focus, $z_r = \frac{\pi\omega_0^2}{\lambda}$ is the Rayleigh range, and r is the radial co-ordinate. Since the Rayleigh range is larger than the beam waist at the focal point, the dipole potential will be steeper along the radial direction than along the propagation (z-axis) direction. From Eqn.5.14 and Eqn.5.16, the dipole potential can be approximated [21] (in the region $z < z_r$) as,

$$U(r,z) = -U_0(1 - \frac{2}{\omega_0^2}r^2 - \frac{z^2}{z_r^2}) \tag{5.17}$$

U_0 is the trap depth. In Fig.5.17b), a typical visual representation of a dipole trap is shown in a 3D plot.

Fig.5.18 illustrates the trap depth (U_0) as a function of laser power [127], beam waist (ω_0) is taken as 2 μm. The angular trap frequencies are defined as $\omega_z = 2\pi\nu_z = \sqrt{\frac{2U_0}{mz_r^2}}$ and $\omega_r = 2\pi\nu_r = \sqrt{\frac{4U_0}{m\omega_0^2}}$.

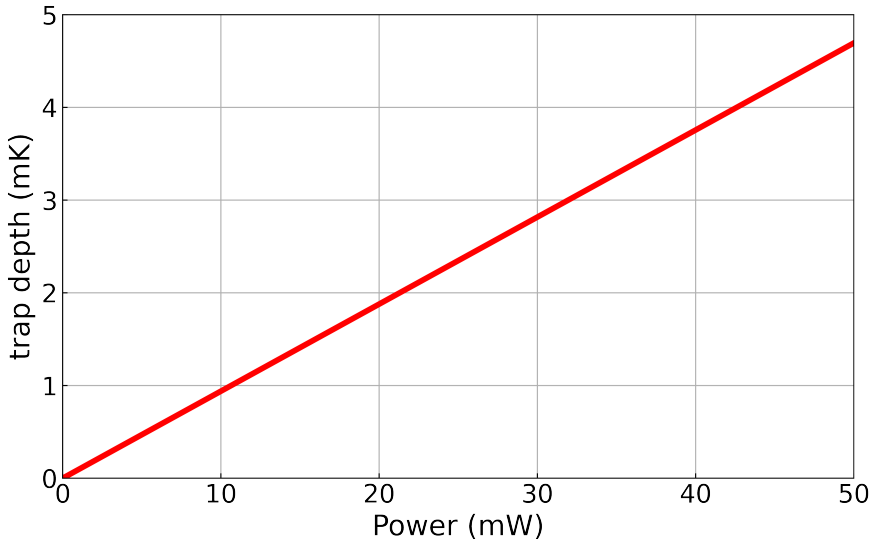


Figure 5.18: Trap depth of the optical dipole trap as a function of the trapping laser power

The number of atoms loaded into the optical dipole trap can be expressed as,

$$\frac{dN}{dt} = R - \gamma N - \beta' N(N-1) \tag{5.18}$$

where, R is the loading rate, γ is the one-body loss coefficient i.e loss due to the collisions with the background room-temperature atoms, β' is responsible for the two-body inelastic collisions inside the trap which varies inversly with the trapping volume. It is shown in [128] that in a small trapping volume i.e trap size (ω_0) less than $4\mu m$ and small loading rate R (upto 100 atoms/s) the two-body collision mechanism becomes the dominant feature, and it locks the average atom number in the trap to $< N >= 0.5$. So either no atom or one atom will be present in the trap. This mechanism is called collisional blockade.

Setup for single atom dipole trapping

In our experimental setup, two High Numerical Aperture (HNA) lenses with $NA \approx 0.5$ are placed inside the vacuum chamber.

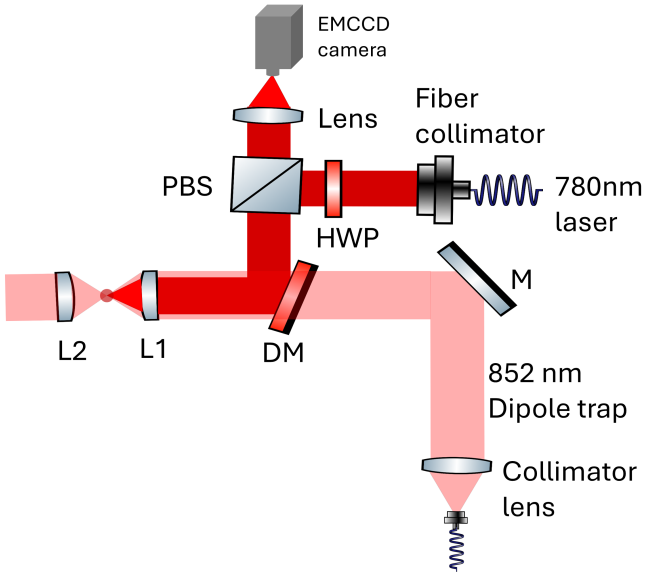


Figure 5.19: Schematic of the setup for single atom trapping. L1 and L2: HNA lenses placed inside the vacuum chamber, DM: Dichroic mirror, M: Mirror, HWP: Half Wave Plate, PBS: Polarizing Beam Splitter,

Because of the large NA, it can focus the dipole trap beam (852 nm) to one micron

focal spot size which is ideal for single atom trapping [128–130] in the collisional blockade regime. The lens system is from Thorlabs (C240TME-B), and it is placed symmetrically with respect to the MOT centre. The focal length and the diameter of each lens is $\approx 8mm$. The distance between the two lenses is around 1.1 cm. The experimental setup of the optical dipole trap is shown in the Fig.5.19. We use a 852 nm laser from Toptica (DL100) for the optical dipole trap. The typical output power of the laser is around 70 mW. The output of the laser is coupled to the input of the optical amplifier BoosTA (Toptica). The output of the optical amplifier is around 400 mW. The output is coupled to a single mode polarization maintaining optical fiber with an efficiency of 40%. The output of the fiber is collimated using a collimating lens (60FC-T-4-M-60) of 60 mm focal length. We use a 780 nm (D2 transition) laser beam as a reference to align the 852 nm on the MOT center. There is a shift of $\Delta f \approx 31\ \mu m$ between the focal points of 780 nm and 850 nm light beams due to the variation of the refractive index with wavelength. The shift Δf is being reduced almost to zero by changing the convergence of the trapping beam (852 nm). The distance between the collimator lens and the fiber output is adjusted by a xyz piezo mechanical stage.

For the imaging of the single atom, we are using the same HNA lens that is used to focus the trapping beam, as shown in Fig.5.19. With diameter and focal length of 8 mm, the lens has 6% fluorescence collection efficiency (ratio of solid angle formed by the HNA lens to 4π). A dichroic mirror is used to separate the fluorescence from the trapping beam.

The lifetime [21, 22] of a single atom in a dipole trap depends on many factors like intensity fluctuations [131], beam pointing fluctuations, background pressure, scattering rate etc. Theoretically, it has been demonstrated that the lifetime [131] of an atom in a trap is dependent on the trap parameters. We have measured the intensity fluctuation noise or technical noise of the dipole trap laser to estimate the lifetime of the atom in the optical dipole trap. The intensity fluctuation of the trap laser gives rise to the fluctuation of the trap depth. As a result of this, the atom's average energy will be increased exponentially over time. Let us consider an example of a simple harmonic trap potential. The total energy of an atom with

intensity fluctuations in the dipole trap is,

$$E = \frac{p^2}{2m_{Rb}} + \frac{1}{2}m_{Rb}\omega_{tr}^2(1+\epsilon(t))z^2 \tag{5.19}$$

$\epsilon(t)$ is the fractional intensity fluctuation, m_{Rb} is the mass of Rb atom, p is the momentum of the atom. With intensity fluctuation $\epsilon(t) = 0$, the total energy transforms into that of a simple harmonic Hamiltonian. The term $\frac{1}{2}m_{Rb}\omega_{tr}^2\epsilon(t)z^2$ acts as a time-dependent perturbation to the quantum states ($|n\rangle$) of the atom in the dipole potential. Since, the time-dependent perturbation term is proportional to the square of the distances ($\propto z^2$), the proper transition will be among the $|n\rangle \Leftrightarrow |n \pm 2\rangle$ states. As a result of these transitions, the average energy of the atom grows as $\langle E\rangle = E_0 e^{\Gamma_\epsilon t}$, as calculated in [131]. The term 'Γ_ϵ' is called the heating rate constant and is given by $\Gamma_\epsilon = \pi^2\nu_{tr}^2 S(2\nu_{tr})$. $\omega_{tr} = 2\pi\nu_{tr}$ is the angular trap frequency, $S(2\nu_{tr})$ is the power spectral density of the fractional intensity fluctuation at twice the trap frequency.

Fig.5.20 shows the relative intensity noise (RIN) of the dipole trap (852 nm) laser. The noise is measured using a spectrum analyzer (Anritsu MS2721B) and a amplified photodiode (bandwidth 10 MHz). To convert to the RIN, the measured noise (in units of Volt/$\sqrt{Hz}$) is divided by the DC voltage of the detector.

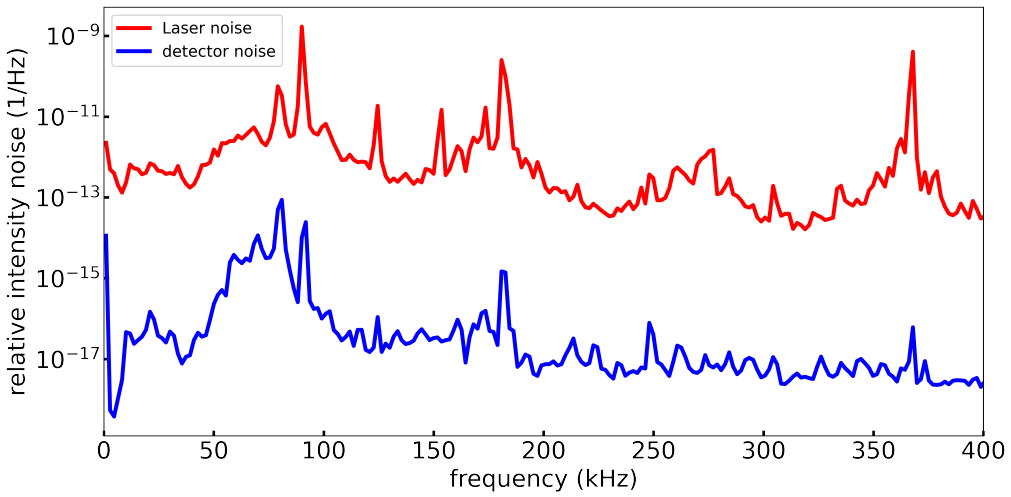


Figure 5.20: The red colored line shows the relative intensity noise of the dipole trap. The detector noise is represented by the blue colored line.

The lifetime due to the RIN is expressed as [22]

$$\tau_{noise} = \frac{m\omega_0^2}{U_0 S(2\nu_{tr})} ln(\frac{U_0}{E_0}) \tag{5.20}$$

where E_0 is the initial temperature of the atom. It is clear from equation 5.20 that lifetime of the atom in a dipole trap depends on the trap parameters such as trap size, trap depth and the power spectral density $S(2\nu_{tr})$. Fig.5.21 shows the simulated lifetime of the trapped atom as a function of the initial energy (E_0). The beam waist is taken as 2 μm. As the initial energy of an atom increases, its lifetime decreases. We also simulate the lifetime at different trap depths (0.75 mK and 1.5 mK). Intuitively, one may expect that as the trap depth increases the lifetime of the atom should be increased. However, as trap depth is increased, the trap frequency is also increased and hence the heating rate constant (Γ_ϵ) which is quadratically increased.

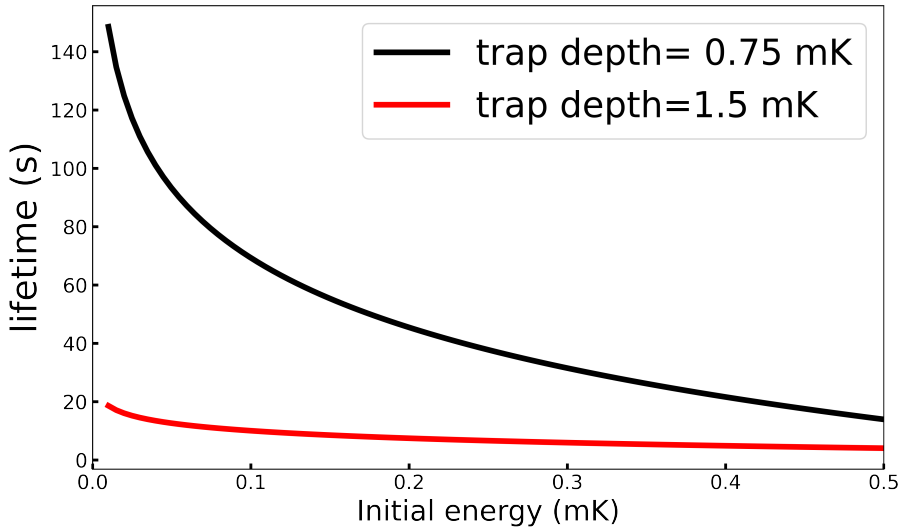


Figure 5.21: lifetime as a function initial energy. Beam waist is kept at 2 μm.

The typical parameters for the graph (Fig.5.21) : for $U_0 = 0.75\ mK$, $\nu_z \approx 5.01\ kHz$, $\nu_r = 52.25\ kHz$, $S(2 \times 52.25) \approx 1.08 \times 10^{-12}\ 1/Hz$, and for $U_0 = 1.5\ mK$, $\nu_z \approx 7\ KHz$, $\nu_r \approx 74\ kHz$, $S(2 \times 74) \approx 5 \times 10^{-13}\ 1/Hz$. Here ν_z is the trap frequency along the z-axis and ν_r is the trap frequency along the radial direction (see Eqn.5.17).

5.3 Conclusion

In this chapter, I have provided a theoretical description to elucidate the principles of MOT operation. Thereafter, I have shown our experimental setup used for cooling and trapping of atoms in the MOT. The realization of sub-Doppler cooling of atoms is also described. After the sub-Doppler cooling, the temperature of the MOT reduces from $150\mu K$ to below $30\mu K$. Further optimization of other parameters such as cancellation of stray magnetic fields, repumping beam power are needed to reduce the temperature futher. The limitation for further reduction of the temperature of the atoms is that the detuning of the cooling laser beams cannot be increased more than -7Γ since for larger detuning, the total MOT cooling beam intensity reduces below the saturation intensity, which causes heating of atoms instead of cooling. Sub-Doppler cooling is crucial for loading atoms into the dipole trap and for increasing the atom's lifetime in the dipole trap. I have also presented a detailed description of the atom trapping mechanism in the optical dipole trap and the process of loading of a single atom in the trap. Once the single atom is loaded in the dipole trap, it's life time depends on several factors like the relative intensity noise (RIN) of the dipole trap laser, beam pointing fluctuations at the trap center and the collisions due to presence of room-temperature atoms in the background. We have measured the RIN of the optical dipole trap and have estimated the lifetime of the atoms in the trap (see Fig.5.21).

CHAPTER 6

Probing of Rydberg interaction using Autler-Townes splitting

In this chapter, we study the effect of inter-atomic interaction between Rydberg atoms in a cold atomic ensemble. We probe the interaction using the Autler-Townes splitting of the $\{5S_{\frac{1}{2},F=2}\} \rightarrow \{5P_{\frac{3}{2}}, F' = 3\}$ transition in cold ^{87}Rb atoms in a magneto-optical trap (MOT). The cooling laser beams of the MOT with high intensity causes the Autler-Townes splitting of the energy levels corresponding to the cooling transition ($\{5S\frac{1}{2}, F = 2\} \rightarrow \{5P_{\frac{3}{2}}, F' = 3\}$) at 780 nm wavelength into dressed states. The Autler-Townes splitting is then measured using a weak probe beam (480 nm), which couples the intermediate state ($5P_{3/2}, F' = 3$) of the three-level system to the highly excited Rydberg states. As the probe beam couples the atoms from the dressed states to the Rydberg states, the atoms move out of the MOT cooling cycle and are eventually lost from the trap. This is called the trap loss spectroscopy [132]. We measure the Autler-Townes spectra using this trap loss spectroscopy technique. The Autler-Townes spectra is recorded by scanning the probe frequency around the Rydberg state. The transition frequencies to the highly excited Rydberg states were measured in our experiment as demonstrated in the chapter 3.

The Van der Waals interaction between two Rydberg atoms varies as $\propto n^{11}$. The

Van der Waals interaction-induced dephasing causes the broadening of the Autler-Townes splitting [133, 134]. We record the Autler-Townes spectra by varying the principal quantum number 'n' to demonstrate the broadening in the Autler-Townes splitting signal due to the Van der Waals interaction between Rydberg atoms [133].

6.1 Experimental setup

Fig.6.1(a) demonstrates the schematic of the experimental setup used in the measurements. A comprehensive description of our cold atom experimental setup can be found in Chapter 5. The cooling beams are red-detuned by 2Γ to the cooling transition of the MOT ($\{5S_{\frac{1}{2}}, F = 2\} \rightarrow \{5P_{\frac{3}{2}}, F' = 3\}$).

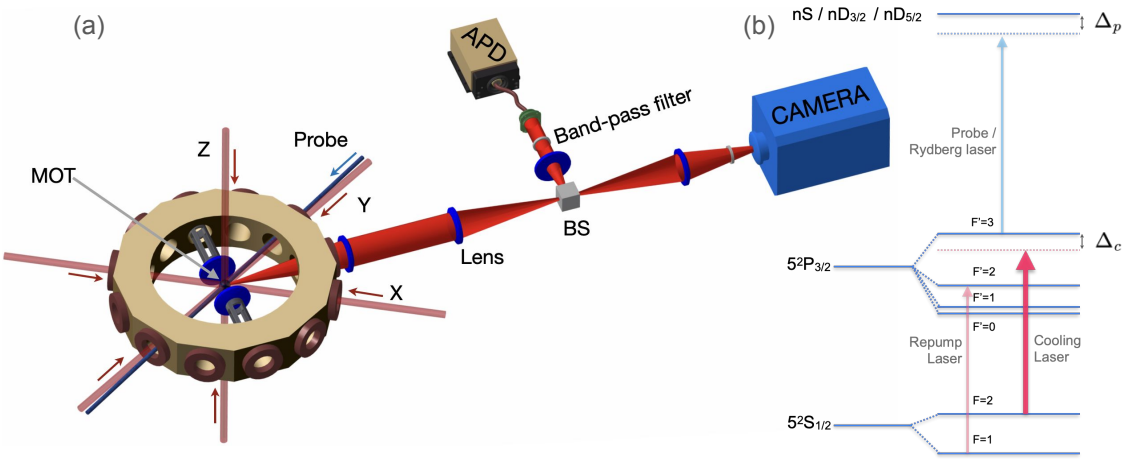


Figure 6.1: a) Experimental setup used to probe the inter-atomic interaction between Rydberg atoms using trap-loss spectroscopy. b) Energy-level diagram for the measurement of Autler-Townes spectra.

The repumping laser is locked to the $\{5S_{\frac{1}{2}}, F = 1\} \rightarrow \{5P_{\frac{3}{2}}, F' = 2\}$ transition. The X,Y,Z beams in Fig.6.1(a) represent the cooling beams and the repumping beam is coincided with the Z-cooling beam. The size (Gaussian diameter) of the cold atomic cloud in the MOT is $\approx 700\ \mu m$. The temperature of the MOT is $\approx 200\ \mu K$, and it is measured using the time-of-flight (TOF) method (see chapter5).

Fig.6.1b) shows the energy diagram for the Autler-Townes splitting used in this experiment. The strong cooling laser with intensity $\approx 15\ I_{sat}$ is used as a coupling laser to create the splitting into dressed states. The probe (480 nm) laser is derived from a Toptica TA-SHG pro laser system, and it is aligned along with the Y-cooling

beam though they are not parallel. The Gaussian diameter of the probe laser beam is measured to be around 1.5 mm. The frequency of the probe laser is monitored by a wavelength meter (WS8-2 from HighFinesse). To align the probe laser on to the MOT, first the probe laser frequency is kept at resonance to any Rydberg transition. Then the trap loss is maximized at low probe power by slightly adjusting the probe beam with the mirrors. We monitor the trap loss by observing the fluorescence from the MOT cloud using an EMCCD camera and an APD (SPCM-AQ4C from Excelitas), as shown in Fig.6.1(a). The fluorescence detection setup is discussed in

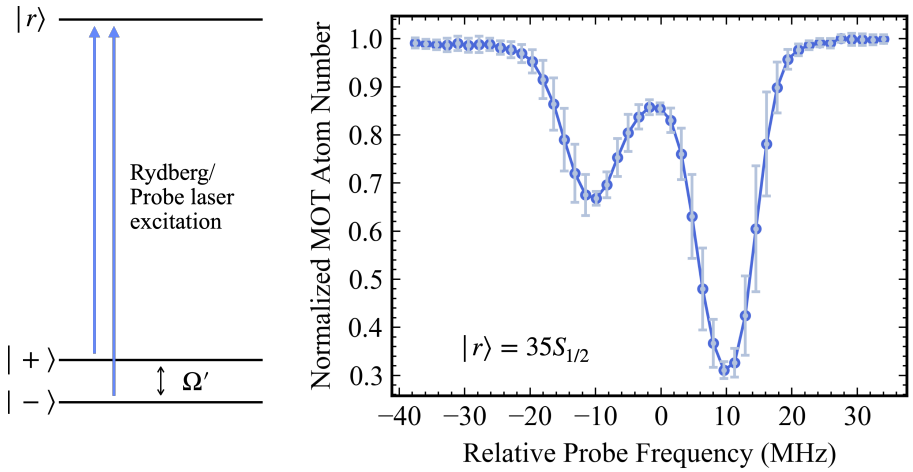


Figure 6.2: Autler-Townes spectra of $\{35S_{\frac{1}{2}}\}$ Rydberg state, Ω' is generalized Rabi frequency. Y-scale defined as normalized atom number in the MOT. Two dips in Autler-Townes spectra corresponding to $|+\rangle$ and $|-\rangle$ dressed states. The generalized Rabi frequency is set around $\Omega' = 2\pi \times 21$ MHz.

chapter 5. We capture the Autler-Townes spectra with the APD while scanning the probe frequency The probe frequency is recorded using the wavelength meter simultaneously to later convert the Autler-Townes spectra to a frequency scale. The frequency scanning rate of the probe laser is below 5 MHz/second and the time bin for APD is set to 0.5 seconds.

6.2 Results and discussion

Fig.6.2 shows the typical Autler-Townes spectra corresponding to the $35S_{\frac{1}{2}}$ Rydberg state. The generalized Rabi frequency is written as $\Omega' = \sqrt{\Omega_c^2 + \Delta_c^2}$, where Ω_c is the Rabi frequency of the cooling beam and Δ_c is the detuning of the cooling beam.

The two dips that arise in the Autler-Townes [135] spectra correspond to the $|-\rangle$ and $|+\rangle$ dressed states. The asymmetry between the two Autler-Townes dips is due to the detuning of the cooling laser which acts as the coupling beam.

Fig.6.3a) represents experimentally observed Autler-Townes spectra for the states $nS_{\frac{1}{2}}$, where n = 67,77,87,97,107,117. In this measurement, we record the Autler-Townes spectra by keeping the same generalized Rabi frequency ($\Omega' = 2\pi \times 23.71$ MHz) and same cooling beam detuning Δ_c of 1.67Γ, where $\Gamma = 2\pi \times 6.01$ MHz. The Rabi frequency of the probe beam is also kept constant at $2\pi \times 5.20$ kHz for all the principal quantum numbers mentioned above.

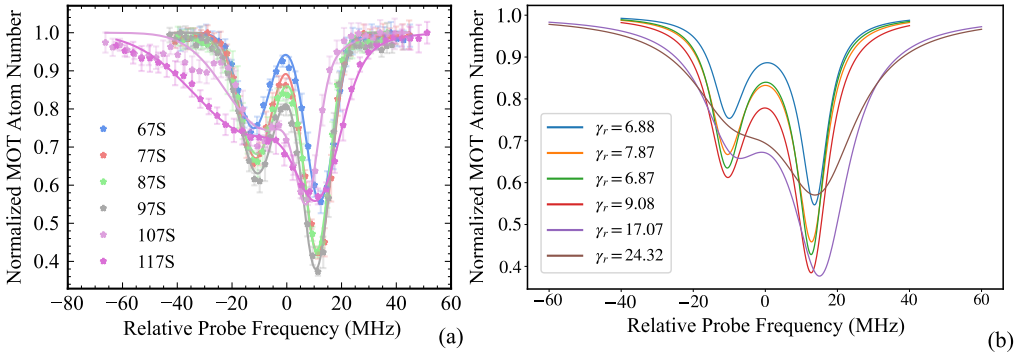


Figure 6.3: a) Experimental measurements of the Autler-Townes splitting for various principal quantum numbers. b) Theoretically estimated Autler-Townes spectra for the same set of principal quantum numbers.

The Van der Waals interaction between the two Rydberg atoms scales as $\propto n^{11}$, this interaction induces dephasing which causes broadening in the Autler-Townes spectra. We can observe the broadening effect at the principal quantum number starting from n = 97. As the principal quantum number 'n' increases, the Van der Waals interaction is also enhanced, resulting in a larger broadening of the Autler-Townes spectra.

We use an effective single-atom model to describe the above phenomena. First, we start with the Lindblad master equation 2.1, which is mentioned in chapter 2. The time-independent Hamiltonian in a rotating frame for a single atom is given as,

$$H = \begin{bmatrix} 0 & \Omega_c & 0 \\ \Omega_c & -2\Delta_c & \Omega_p \\ 0 & \Omega_p & -2(\Delta_c + \Delta_p) \end{bmatrix}$$

The decay and the dephasing matrix L_{decay} is written as,

$$L_{decay} = \begin{bmatrix} \Gamma_{eg}\rho_{22} & -\frac{1}{2}\Gamma_{eg}\rho_{ge} & -\frac{1}{2}\gamma_3\rho_{gr} \\ -\frac{1}{2}\Gamma_{eg}\rho_{eg} & -\Gamma_{eg}\rho_{ee} + \Gamma_{re}\rho_{rr} & -\frac{1}{2}(\Gamma_{eg} + \gamma_3)\rho_{er} \\ -\frac{1}{2}\gamma_3\rho_{rg} & -\frac{1}{2}(\Gamma_{eg} + \gamma_3)\rho_{re} & -\Gamma_{re}\rho_{rr} \end{bmatrix}$$

Γ_{ij} are the spontaneous decay terms from the state $|i\rangle$ to $|j\rangle$, $\gamma_3 = \gamma_r + \Gamma_{re}$ is the dephasing of the Rydberg state $|r\rangle$, where γ_r is introduced here as a Van der Waals interaction-induced dephasing [136].

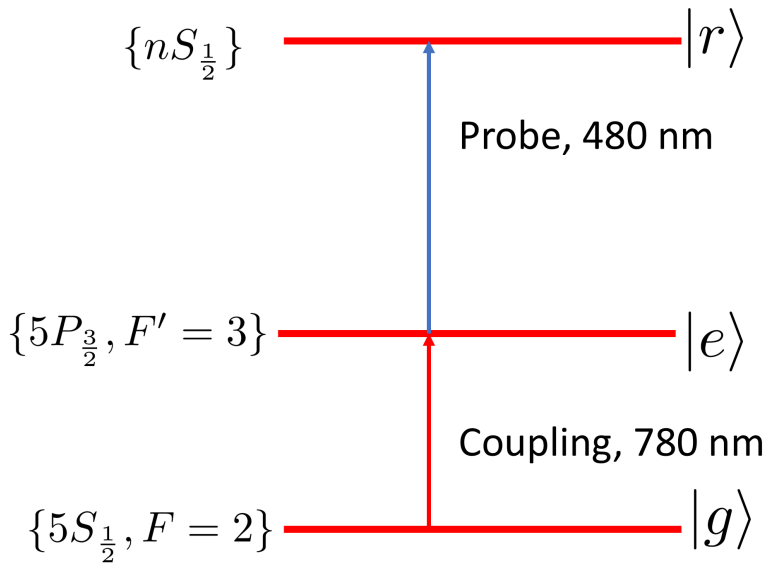


Figure 6.4: Energy diagram for the Autler-Townes splitting of ^{87}Rb

Given that our measurement time is in the range of a few milliseconds, we consider the steady-state solution of the Lindblad master equation. From the steady-state solution, $f_R = \rho_{rr}$ is the fraction of atoms excited to the Rydberg state. For our experiment, we are measuring the number of atoms in the MOT by observing the fluorescence, so 1 - f_R is the fraction of atoms remain in the trap after Rydberg excitation. The term $\alpha(1 - f_R)$ is fitted to the experimental data as a function of the probe detuning Δ_p. γ_r and Δ_c are used as free parameters for the fitting. Δ_c is taken as a free parameter as effect of the interaction is to shift the cooling beam detuning [137]. We put the value of α externally to match the fraction of atoms with the experimental data.

The values of γ_r and the shift in the detuning Δ_c are determined by minimizing the Binary Cross-Entropy loss function. The Binary Cross-Entropy loss function is defined as,

$$L = -\frac{1}{N}\sum[y_i^{exp} log y_i^{theo} + (1 - y_i^{exp}) log(1 - y_i^{theo})] \tag{6.1}$$

where N is the number of sample, y_i^{exp} is the fraction of atoms remaining in the MOT. The term y_i^{theo} indicates the theoretical values of $1 - f_R$ at the specific probe detuning where the experimental data is collected.

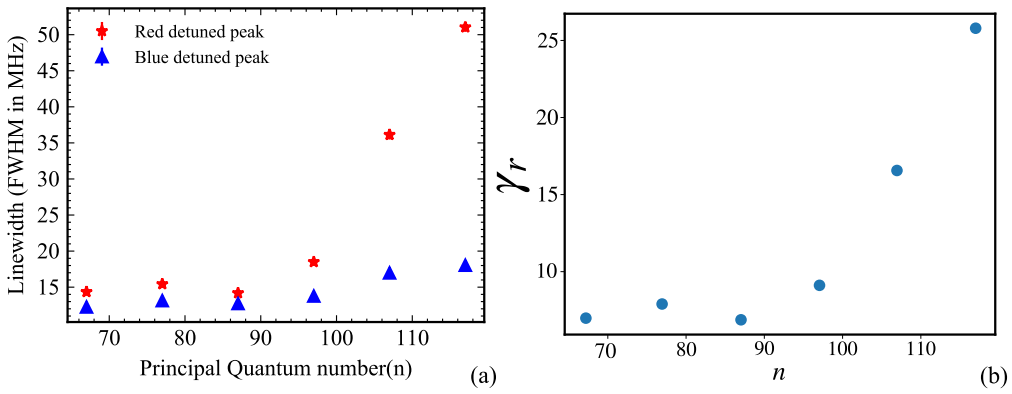


Figure 6.5: (a) Linewidth of the red-detuned and blue-detuned peaks of the Autler-Townes spectra vs n. (b) Dephasing rate vs n, obtained by optimizing Binary Cross-Entropy loss function.

Fig.6.5(b) shows the variation of the dephasing rate as a function of 'n', determined by the aforementioned optimization method.

6.3 Summary

We measure the Autler-Townes spectra for a range of principal quantum numbers. We observe that the Autler-Townes peaks are separated by the generalized Rabi frequency (Ω'). The Van der Waals interaction between the Rydberg atoms induces the dephasing in the Rydberg states, which causes the broadening of the Autler-Townes spectra. We observe an asymmetry in the Autler-Townes spectra, with the red-detuned peak (left peak in Fig.6.3(a)) being more affected due to the inter-atomic Van der Waals interactions. We investigate this phenomenon using theoretical modelling and numerical simulation.

CHAPTER 7

Rydberg-excitation mediated trap-loss spectroscopy

This chapter presents the experimental results of the Rydberg excitation of trapped atoms (^{87}Rb) in the Magneto-optical trap (MOT). We use two-photon excitation scheme to realize Rydberg atoms in the MOT. Our scheme involves the excitation pathway for the three-level ladder-type system: $\{5S_{\frac{1}{2}}F = 2\} \rightarrow \{5P_{\frac{3}{2}}F' = 3\} \rightarrow \{nS_{\frac{1}{2}}\}$. First, the atom is excited from the $\{5S_{\frac{1}{2}}, F = 2\}$ state to the intermediate state $\{5P_{\frac{3}{2}}, F' = 3\}$ using a far-detuned 780 nm laser beam. Finally, the excitation to the Rydberg state is performed using a 480 nm laser beam. Two-photon excitation in a three-level system using two resonant or near-resonant light fields can realize coherent processes such as Electromagnetically Induced transparency and Autler-Townes splitting [138]. Once the atoms are in the Rydberg state, they will be out of the laser cooling cycle in the MOT and eventually would get lost from the trap. This is called trap-loss spectroscopy. Trap loss spectroscopy is a useful technique for measuring Autler-Townes spectra, probing interatomic interactions, and the detection of Rydberg atoms. The effect of Rydberg excitation is as follows

$$\frac{dN}{dt} = R - (\gamma + \gamma_{Ryd})N + \beta N(N-1) \tag{7.1}$$

where, N is number of atoms in the MOT, R is the loading rate of the MOT, γ is the loss rate of a single body, γ_{Ryd} is the decay rate due to Rydberg excitation, and β is the loss rate due to two-body collisions. Neglecting β, at steady state, the ratio of the number of atoms with Rydberg excitation to the number of atoms without excitation is expressed as follows,

$$\frac{\langle N \rangle_{Ryd}}{\langle N \rangle_0} = \frac{\gamma}{(\gamma + \gamma_{Ryd})} \tag{7.2}$$

Assuming the loading rate (R) is the same for both cases, it can be observed from Eqn.7.2 that the number of atoms is reduced by a factor of $\frac{1}{1+\frac{\gamma_{Ryd}}{\gamma}}$.

In this chapter, I describe our measurement of the trap-loss spectra for Rydberg states with various principal quantum numbers states (n = 48, 68, 78) for the same set of Rabi frequencies of the excitation beams and the excitation times. We demonstrate that the fractional number of atoms lost from the trap increases with the principal quantum number (n) of the Rydberg state when the Rabi frequency and the excitation times are kept at fixed values.

7.1 Experimental setup

In this chapter, we perform experiments on cold atoms trapped in a magneto-optical trap (MOT). The experimental setup for the MOT is discussed in chapter 5. We use far-detuned 780 nm and 480 nm laser beams to excite the atoms from the ground state $\{5S_{\frac{1}{2}}, F = 2\}$ to the Rydberg state $\{nS_{\frac{1}{2}}, F'' = 2\}$. The 780 nm laser is blue-detuned relative to the $\{5S_{\frac{1}{2}}, F = 2\} \rightarrow \{5P_{\frac{3}{2}}, F' = 3\}$ transition by 482 MHz and the 480 nm laser is red-detuned by the same amount relative to the $\{5P_{\frac{3}{2}}, F' = 3\} \rightarrow \{nS_{\frac{1}{2}}, F'' = 2\}$ transition, to achieve the two-photon transition resonant from the ground state to the Rydberg state.

7.1.1 Excitation laser

Fig.7.1 illustrates the schematic used for shifting the frequency of the 780 nm laser. The laser output is taken from a Toptica DL100 ECDL (External Cavity Diode

Laser). After the optical isolator, the laser power is divided into two parts by using a polarizing beam splitter (PBS1 in Fig.7.1) and a Half Wave Plate (HWP2) plate: one part is directed to the saturation absorption spectroscopy (SAS) setup used for frequency stabilization of the laser, and the other part is directed to a frequency shifting setup, where the laser frequency is shifted using a double pass through an AOM (acousto-optic modulator). We use an AOM with carrier frequency 250 MHz from AA Opto-Electronic (model: MT250-B100A0.5-800) for the same.

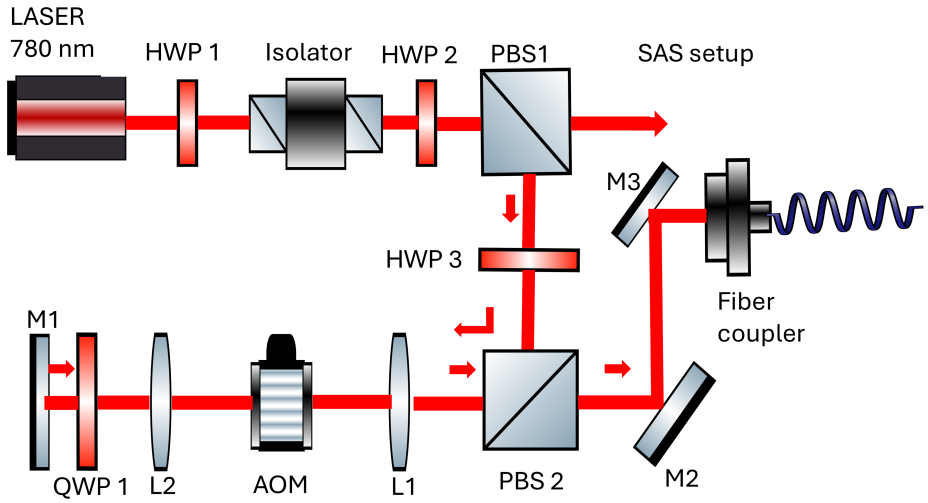


Figure 7.1: Schematic for frequency shifting of the 780 nm laser. HWP1, HWP2, HWP3: Half wave plate, QWP1: Quarter wave plate, AOM: Acousto Optic Modulator, PBS1, PBS2: Polarizing Beam Splitter, M1, M2, M3: mirror, SAS: Saturation Absorption Spectroscopy, L1 and L2: Lens

The AOM is placed at the focus of the telescopic lens system (L1 and L2) with focal length of 10 cm each to improve the efficiency of the AOM double pass. We use the mirror (M1) to reflect the +1 order of the first-pass diffraction pattern back into the AOM for the second pass. The Quarter Wave plate (QWP) is used to control the power of the +1 diffraction order of the 2nd pass at the polarizing beam splitter (PBS2) output. The output is then coupled to a polarization maintaining single mode optical fiber. The center frequency of the AOM is set at 241 MHz, so the total frequency shift of the laser is +482 MHz after the double pass. The laser frequency is locked to $\{5S_{\frac{1}{2}}, F = 2 \rightarrow 5P_{\frac{3}{2}}, F' = 3\}$ transition using Saturation Absorption Spectroscopy (SAS). After the AOM double pass, the 780 nm laser frequency is

blue-detuned by 482 MHz to the $\{5S_{\frac{1}{2}}, F = 2 \rightarrow 5P_{\frac{3}{2}}, F' = 3\}$ transition.

Fig.7.2 illustrates the schematic for shifting the frequency of the 480 nm laser. The laser output is split into two parts using a half-wave plate (HWP2) and a polarizing beam splitter (PBS1) as shown in Fig.7.2): one part is directed to the vapor cell experiment setup which is discussed in chapters 3 and 4, and the other part is directed to the cold atom experimental setup.

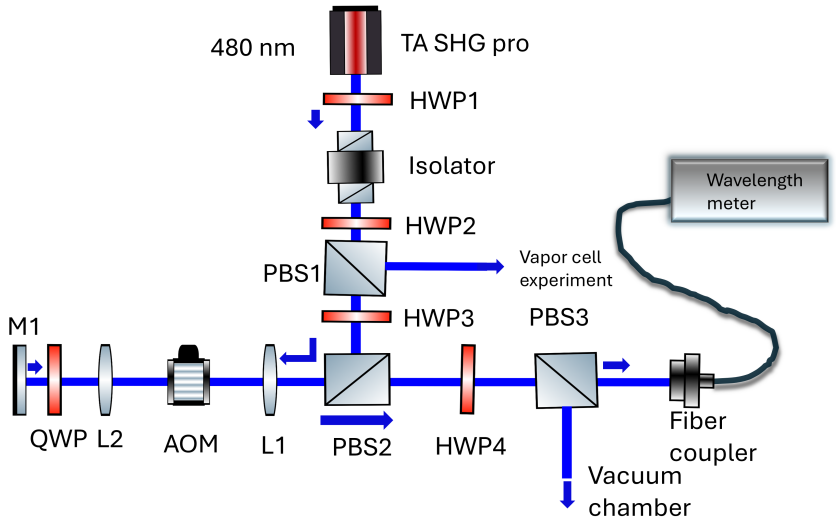


Figure 7.2: Schematic of the 480 nm laser utilized for frequency shifting and switching on/off of the laser. HWP1, HWP2, HWP3 : Half Wave Plate, QWP: Quarter Wave Plate. PBS1, PBS2, PBS3: Polarizing Beam Splitter. L1 and L1: lens with focal length 10 cm. AOM: Acousto Optic Modulator.

We use an AOM from AA Opto-Electronic (model: MT250-B100A0.5-400) for frequency shifting in a double-pass arrangement, and we utilize the -1 diffraction order for the same.

Since the 780 nm laser is blue-detuned by 482 MHz, the 480 nm laser is red-detuned by the same amount for the Rydberg excitation from the ground state ($\{5S_{\frac{1}{2}}, F' = 3\}$) to the Rydberg state ($\{5P_{\frac{3}{2}}, F'' = 2\}$). A small portion of the light is fed to the wavelength meter (from HighFineese, WS8-2) by using a PBS (PBS3) and a HWP (HWP4) to monitor the laser frequency during the experiment. The transition frequencies of Rydberg states are measured and reported in chapter 3, we tune the frequencies corresponding to the Rydberg states from these measurements. The lenses (L1 and L2, focal length 10 cm) in telescopic configuration are used to

improve the efficiency of diffraction to the -1 order. The mirror M1 is used to reflect back the -1 order of the diffraction back into the AOM for the second-pass. The QWP (Quarter Wave Plate) is used to maximize the power at the PBS2 output.

Fig.7.3 shows the typical energy diagram of the two-photon excitation. The detuning is $\Delta_e = +482$ MHz. The laser power to the experiment is controlled by a HWP (HWP4).

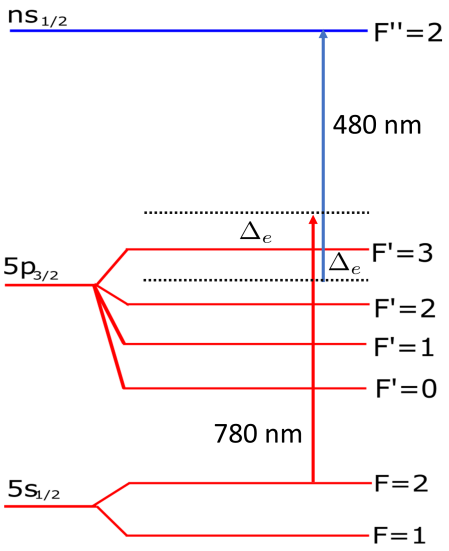


Figure 7.3: Two-photon excitation scheme, Δ_e is detuning of the laser from the transition to the intermediate state $\{5P_{\frac{3}{2}}, F' = 3\}$.

Fig.7.4 shows the experimental setup including the imaging setup used for the experiments described in this chapter. The imaging setup is discussed in chapter 5. The same EMCCD camera (PhotonMax-512 from Princeton Instruments) is used to record the images of the atoms using fluorescence imaging. A beam spliiter (BS) is used to divide the MOT fluorescence into two parts: one part is sent to the EMCCD camera, while the other part is sent to the fiber coupler and then connected to the Avalanche Photo Diode (APD). We use the APDs to confirm the trap loss by two-photon excitation as we scan the 480 nm laser frequency, which is monitored by the wavelength meter (see Fig.7.2).

The 480 nm laser is focused to the MOT center by using an A-coated lens of 30 cm focal length. The beam waist is measured by a scanning-slit beam profiler (from Thorlabs) outside the vacuum chamber keeping the same distance as it is from the

lens (L3) to the MOT center. The beam waist of the 480 nm laser beam is 250μm. On the other hand, the 780 nm laser beam is collimated and aligned through the MOT. The beam diameter of the 780 nm laser beam is measured to be around 1.2 mm. As the 780 nm laser is blue-detuned, it will not interact (without the 480 nm laser) with the atoms in the MOT. Hence, to align the excitation lasers (780 nm and 480 nm) on the MOT, we use another laser (called probe laser) with frequency tuned to the MOT cooling transition frequency ($\{5S_{\frac{1}{2}}, F = 2 \rightarrow 5P_{\frac{3}{2}}, F' = 3\}$) and has the same beam diameter as the excitation 780 nm laser. First, the probe beam is symmetrically aligned with the MOT by observing the fluorescence in the vacuum chamber. This is achieved using two standard CCTV cameras positioned perpendicularly to each other. When the probe laser is aligned with the MOT, the trapped atoms will experience the radiation force due to the probe laser and will be lost from the MOT. After that the fine alignment is done by reducing the probe power and adjusting the horizontal and vertical adjustment screws of the mirrors. For our case, we observe that the trap-loss occurs at minimum 14 μW of probe power. Then the excitation lasers are aligned by coinciding their Gaussian centers with the probe laser.

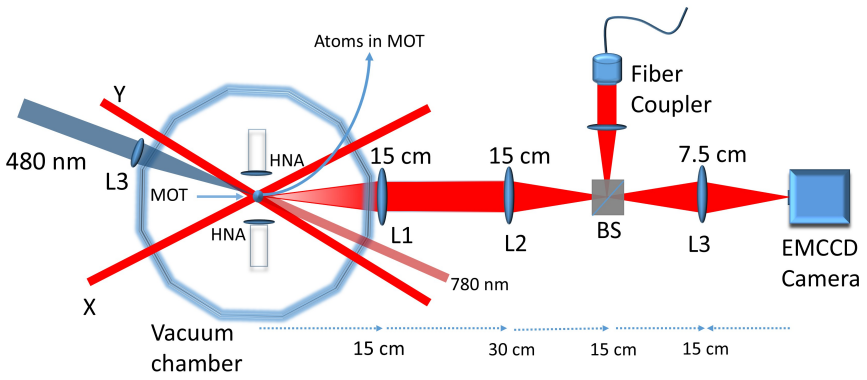


Figure 7.4: Schematic of the setup used for Rydberg excitation. For imaging setup: see chapter 2. L3: A-coated lens used for focusing the 480 nm laser. X,Y: MOT cooling beam (Z MOT beam is not shown in the figure.)

Further optimization of the alignment is done with the help of mirrors (not shown

in the figure) and simultaneously monitoring the trap-loss in the APD signals at the two-photon resonance condition.

Both of the excitation lasers (780 nm and 480 nm) are aligned in counter-propagating direction to reduce the Doppler shift.

Switching circuit

All the instruments used in the experiment are controlled by the LabVIEW software, which is interfaced with an NI PCIe-6363 card, it is capable of generating pulses as short as 1 μs. AOM's are switched on and off by SPDT switches (ZX80-DR230-S+) from Mini-Circuits. It has a switching time of 1 μs. We utilize an IGBT (Insulated Gate Bipolar Transistor) circuit to control the magnetic field for switching on and off. The switching-off time of the IGBT circuit is measured to be around 400 μs. The fast switching-off time of the magnetic field is important in the sub-Doppler cooling stage. The details of the IGBT circuit is discussed in appendix A

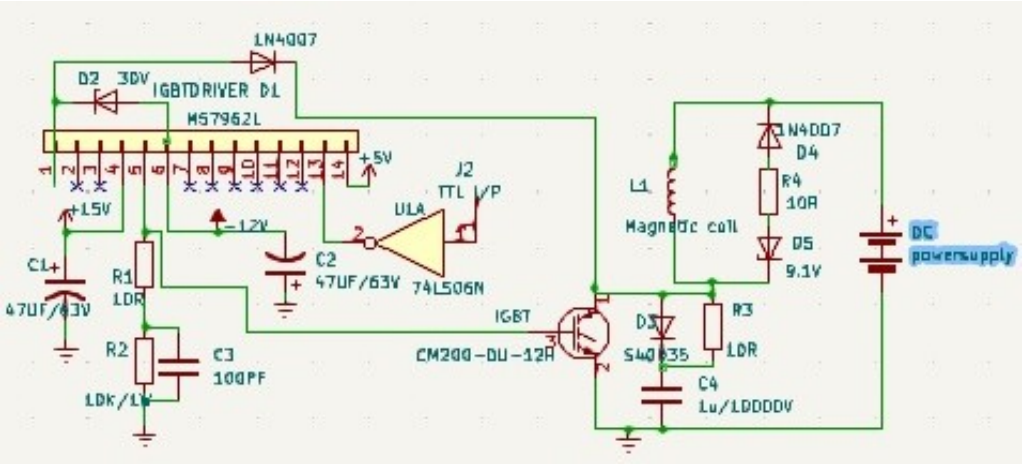


Figure 7.5: IGBT switching circuit

7.2 Results

Fig.7.6 demonstrates the time sequence of the Rydberg excitation used in the MOT. The MOT is loaded for 15 seconds. Hence, the cooling beams, repumping beam and the MOT anti-Helmholtz coil are switched-on for 15 seconds. The duration of the excitation pulse (780 nm and 480 nm) is τ ms.

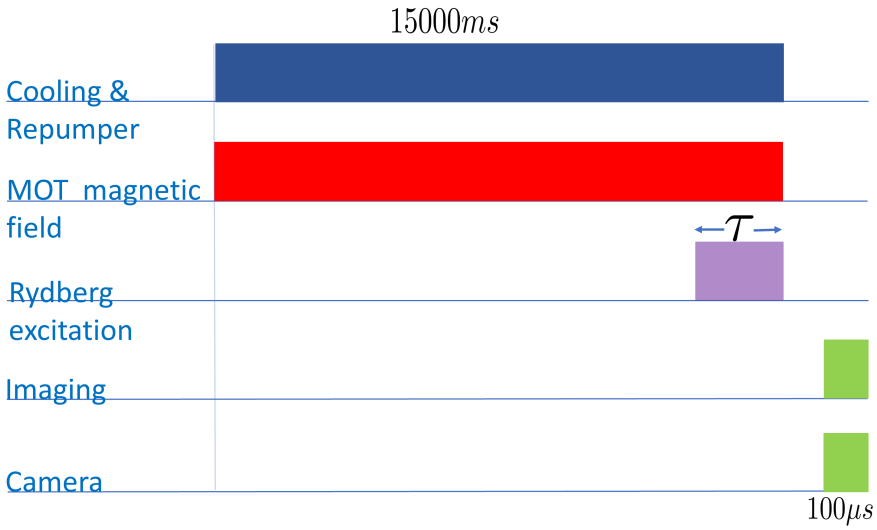


Figure 7.6: Time sequence of the Rydberg excitation using LabVIEW.

The camera exposure time is set to 100 μs. We are using the same cooling and the repumping beams as imaging beams which are switched-on simultaneously with the camera i.e the pulse duration of the imaging beams is synchronized with the camera's exposure time. To calculate the fractional number of atoms lost from the trap due to the Rydberg excitation, we first run the time sequence (Fig.7.6) without switching on the Rydberg excitation beams and calculate the number of atoms (N_0) in the MOT from the image taken by the EMCCD camera (PhotonMax-512). Next, we run the time sequence with Rydberg excitation and determine the number of atoms (N_R) remaining in the trap due to Rydberg excitation, using the image taken by the camera. The fractional number of atoms remaining in the MOT is calculated as $\frac{N_R}{N_0}$, so the fractional number of atoms lost from the MOT is $1-\frac{N_R}{N_0}$. Since, we are calculating the fractional number of atoms remaining in the MOT due to Rydberg excitation, we use the ratio $\frac{N_R}{N_0} = \frac{C_R}{C_o}$, where C_0 and C_R represent the pixel counts of the images without and with Rydberg excitation, respectively. The delay between

the MOT switching off and the imaging time is set to 0.5 ms, as the blooming effect of the camera cannot be reduced below this delay. We notice that the blooming effect is arising due to the saturation of the pixels in the EMCCD camera as the photons are collected from a dense MOT, it only vanishes once the density of the atoms reduces below a certain value in the time of flight process. So the delay time (0.5 ms) is set accordingly. We are also switching off the MOT to make sure that no additional atoms are loaded into the MOT after the Rydberg excitation.

7.2.1 Trap loss versus excitation time

In this measurement, the trap loss due to the Rydberg excitation is measured vs various excitation times while keeping the effective Rabi frequency constant at three different values. The same measurement is repeated for three different Rydberg states $48S_{\frac{1}{2}}, 68S_{\frac{1}{2}}$ and $78S_{\frac{1}{2}}$. The excitation times are varied from 1 ms to 600 ms. Although, we can observe the Rydberg excitation within a time scale of a few tens of microseconds, the blooming effect of the camera limits us to quantify certain measurements.

Fig.7.7 a) illustrates the fractional trap loss due to Rydberg excitation across various excitation times at a two-photon effective Rabi frequency of $2\pi \times 11.75$ KHz. It is clear from Fig.7.7a) that for observable trap loss, a higher excitation time is necessary for low principal quantum number 'n'. For $n = 48$, the trap loss can be observed around an excitation time of 200 ms. In comparison, for the $n = 68$ and $n = 78$ states, trap loss occurs at a shorter excitation time of approximately 50 ms.

Fig.7.7b) presents the same measurements, but this time the Rabi frequency is increased to $2\pi \times 20.36$ KHz, as a result, the trap loss is observable at a shorter excitation time (100 ms for $n = 48$ and 1 ms for $n = 78$). At longer excitation times, the trap loss for higher Rydberg states saturates to maximum value of 90%.

Fig.7.7c) demonstrates the at higher effective two-photon Rabi frequency as compared to the earlier two cases. In this case, the Rabi frequency is set at $2\pi \times 31.11$ KHz. In this case, the detectable trap loss can be observed at 1 ms excitation time for $n = 48, 68$ and 78. At longer excitation time (> 500 ms), the fractional trap loss

for $n = 68$ and $n = 78$ saturates to 90%.

From the above measurement, it is clear that the fractional trap loss due to the Rydberg excitation grows exponentially with the excitation time and saturates to certain values. Another interesting thing to note is that for a given excitation time such as 300ms in Fig.7.7a), the fractional trap loss increases with the principal quantum number ('n') of the Rydberg state. I will discuss this effect in the later part of this section.

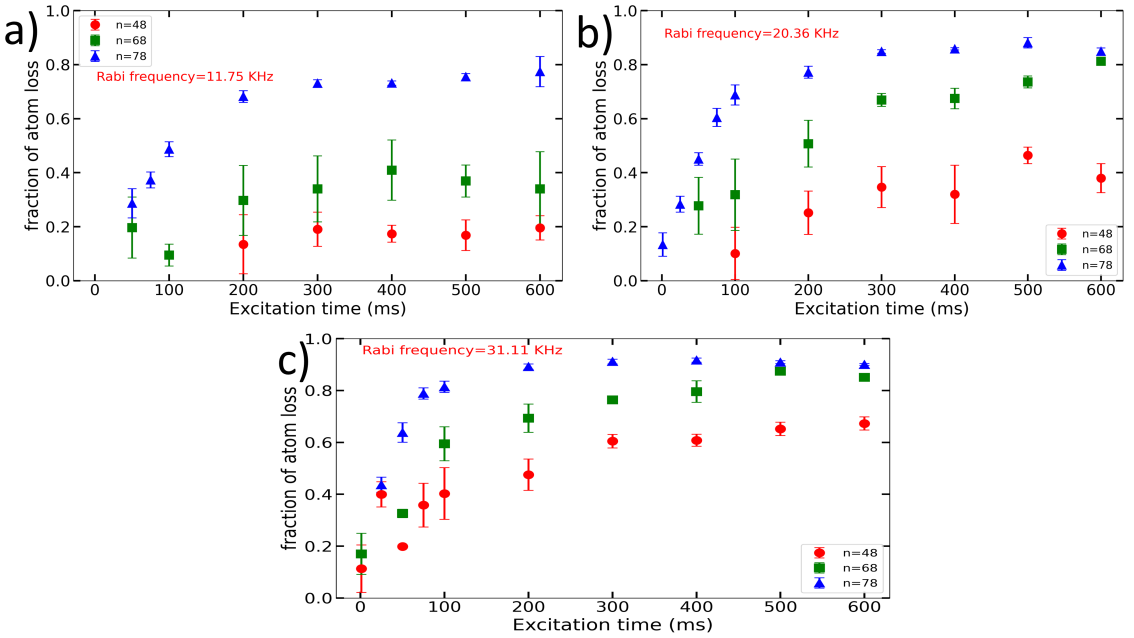


Figure 7.7: Fraction of atom loss vs excitation time. Excitation times are varied from 1 ms to 600 ms. a)effective Rabi frequency fixed at $2\pi \times 11.75$ kHz. b)Rabi frequency of $2\pi \times 20.36$ kHz. c)Rabi frequency of $2\pi \times 31.11$ kHz. The measurements are shown for $n = 48S$, $n = 68S$ and $n = 78S$ Rydberg states represented by the solid red-colored circles, the solid green-colored rectangles, and the solid green-colored triangles, respectively.

7.2.2 Trap loss versus Rabi frequency

In this type of measurement, trap loss is recorded at various Rabi frequencies, with the excitation time held constant for the same set of Rydberg levels as mentioned in the previous section.

Fig.7.8 a) depicts the trap loss across various Rabi frequencies at excitation time of 100 ms for the $48S, 68S$ and $78S$ Rydberg states.

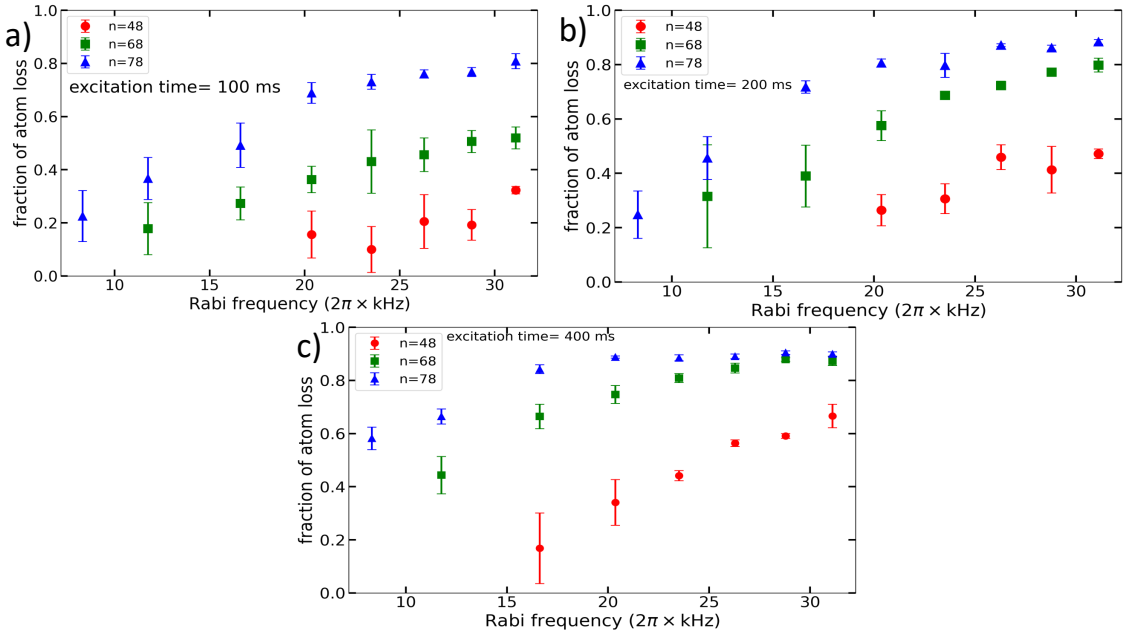


Figure 7.8: Fraction of trap loss at various Rabi frequencies. a) at excitation time of 100 ms. b)excitation time of 200 ms. c) at excitation time of 400 ms. The measurements for $n = 48$, $n = 68$ and $n = 78$ Rydberg states are represented by the solid red-colored circles, the solid green-colored rectangles, and the solid green-colored triangles, respectively.

The values of the two-photon effective Rabi frequencies are varied from $2\pi \times 8.31$ kHz to $2\pi \times 31.11$ kHz. We observe that the detectable amount of trap loss for $48S$ state begins at $2\pi \times 20$ kHz. In comparison, trap loss for $68S$ and $78S$ occurs at lower Rabi frequency of $2\pi \times 8.31$ kHz.

Fig.7.8 b) and c) represent the trap loss vs Rabi frequency for excitation times of 200 ms and 400 ms, respectively. It is evident that even if the excitation times are extended from 100 ms (in Fig.7.8a)) to 400 ms, the trap loss of $48S$ does not saturate like it does at higher Rabi frequencies for high Rydberg states of $68S$ and $78S$. The important thing is that if the Rabi frequency and excitation time are kept at fixed values for all principal quantum number 'n', the trap loss is dependent on 'n', and it is obvious from Fig.7.8 that the trap loss increases with 'n'. Additionally, it is also clear that the fractional trap loss increases exponentially with the Rabi frequency.

7.2.3 Trap loss versus detuning

Fig.7.9 demonstrates the trap loss at various detunings of the two-photon transition frequency.

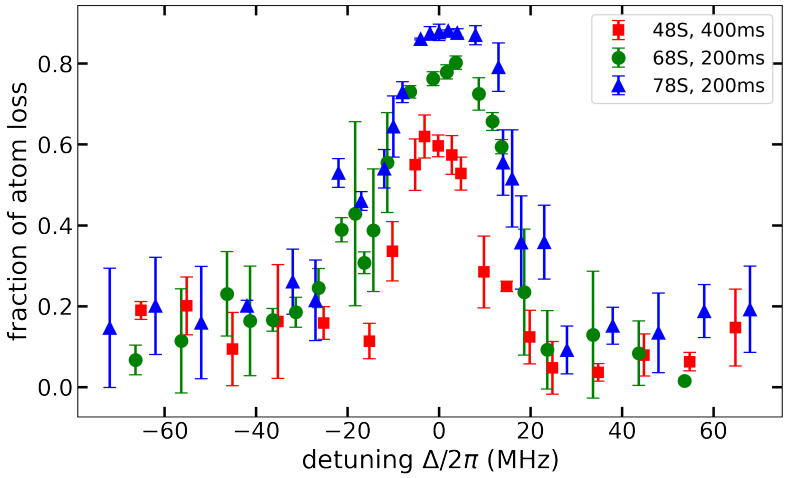


Figure 7.9: Trap loss vs two photon detuning: the solid red-colored points represent the data for $48S$, the solid green-colored circles represent data for $68S$ state and the blue-colored triangles represent $78S$ state.

The detuning of the 480 nm light is varied across the two-photon resonance and monitored using a wavelength meter, as shown in Fig.7.2. The effective two-photon Rabi frequency is kept at $2\pi \times 31.11$ kHz for all the three measurements. Another point to note is that while comparing the trap loss at various detunings for different 'n' values in Fig.7.9, we maintain the excitation at 400 ms for $48S$ state, while keeping the excitation time at 200 ms for $68S$ and $78S$ states. This is because the trap loss versus detuning at excitation time of 200 ms is observed to be very noisy. The linewidths of the trap loss are determined by fitting the Gaussian function and for $48S$ state, the linewidth is approximately $2\pi \times 10$ MHz, while for $68S$ and $78S$ the linwidths are determined to be $2\pi \times 16$ MHz and $2\pi \times 17$ MHz, respectively.

7.2.4 Discussion and Summary

The density of atoms in our MOT is $\approx 10^9$ $atoms/cm^3$. The average distance between the atoms ≈ 10 μm. The interaction between typical cold atoms in the

MOT at this distance is weak. However, Rydberg atoms possess a very high dipole moment ($\propto n^2$) ([34,35]), so the interaction between Rydberg atoms at this distance is strong enough to be observable. Because of the strong dipole moment, two types of inter-atomic interactions are possible: one is resonant dipole-dipole interaction ([59, 60]) and the other is off-resonant Van der Waals interaction (see chapter 2 for details). For a typical MOT size of 500 μm and a MOT temperature of 200 μK, the created Rydberg atoms generally take on an average a few ms to leave the MOT region. Hence, setting the excitation time in ms time scale for studying trap loss is intuitively understandable. Another important reason for the trap loss is possibly the creation of ions in the trap as the excitation beam is switched on more than three order of magnitude times the life time of the Rydberg atoms. Black-Body Radiation (BBR) at 300 K plays an important role for direct photo-ionization [139–141] of Rydberg atoms or redistribution [142] of atoms to other Rydberg states. However, BBR induced ionization can only affect [141] the states with $n < 40$. For $n > 50$, the resonant dipole-dipole and off-resonant Van der Waals interactions are crucial factors in the creation of ions and plasmas in the MOT. It is shown in reference [143] that attractive dipole-dipole interactions can lead to the inter-atomic collisions to create hot atoms and ions, ions then evolve into plasma. A similar role of attractive long-range Van der Waals interactions is evident in the production of ions [144]. In the same reference, it is also demonstrated that repulsive Van der Waals interactions play a significant role in producing ions over much longer time periods compared to the attractive interactions. The reason may be that BBR redistributes the atoms from repulsive potentials to attractive potentials. Here I have shown in Fig.7.10, that trap loss increases with 'n' for the same Rabi frequency of $2\pi \times 11.75$ kHz and the same excitation time of 400 ms. A possible reason could be the effect of Van der Waals interactions creating ions, which enhances the losses with increasing 'n'. Another possible reason may be the direct creation of ions due to the long exposure of 480 nm light during the two-photon excitation process. Another improvement in the experiment would be to install a micro-channel plate detector (MCP) inside the vacuum chamber to directly measure the ions.

A recent study performed by Saakyan et al. [145] shows that the presence of

ions can be detected indirectly by measuring the frequency shift due to the Rydberg excitation at different excitation times. In our experiment, the measurement of fre-

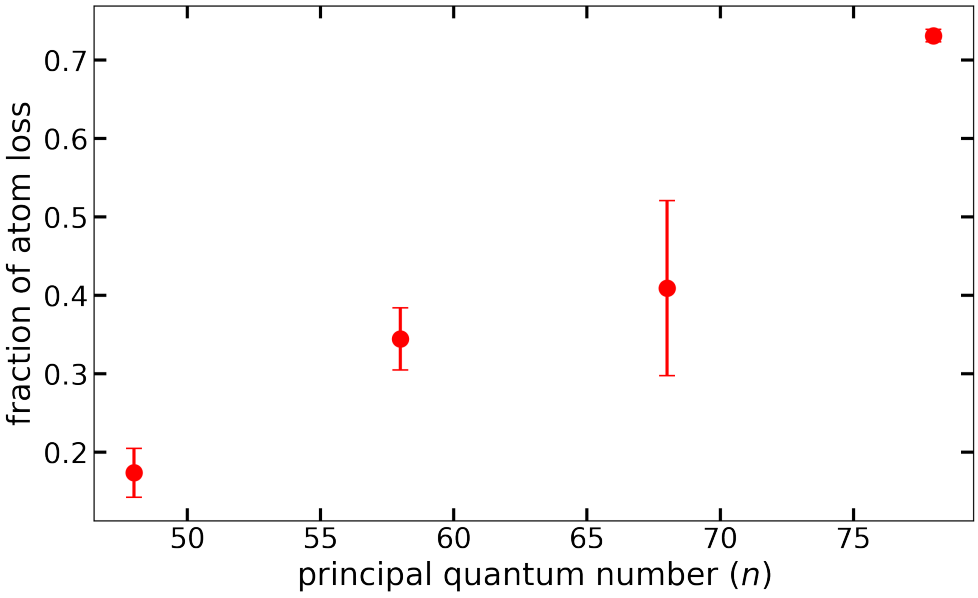


Figure 7.10: Trap loss versus principal quantum number 'n' of the Rydberg state. The two-photon effective Rabi frequency is fixed at $2\pi \times 11.75$ kHz and excitation time is kept at 400 ms.

quency shift at longer excitation times can be performed. We are currently working on locking the 480 nm laser to an ultra-stable cavity from Stable Laser System. In future, we may revisit the same measurement after achieving the cavity lock. We are also in the process of developing the theory regarding the aforementioned behavior of trap loss.

In summary, we have performed the trap loss of ^{87}Rb in a MOT. We measure the trap loss versus the excitation time as well as the two-photon effective Rabi frequency. The same measurement is repeated for different Rydberg states of $48S$, $68S$ and $78S$. Then I finally show that the trap loss increases with 'n' for fixed Rabi frequeny and fixed excitation time.

CHAPTER 8

Summary and future Perspective

8.1 Summary

In this section, I will provide a concise summary of all the work described in the various chapters of this thesis.

This thesis is started by introducing basic theoretical descriptions of atom-photon interaction that results in coherent phenomena such as Electromagnetically Induced Transparency (EIT) and Autler-Townes Splitting (ATS) effects. The Lindblad master equation can be used to investigate both the phenomena. Then, I introduce the properties of Rydberg atoms such as large dipole moments, long lifetimes, and different types Rydberg interactions which leads to the phenomenon known as the Rydberg Blockade.

We use EIT spectroscopy to measure the transition frequencies of highly excited Rydberg states. From this measurement, we determine the the quantum defects of S and D orbitals. The transition frequencies are measured with respect to the $\{5P_{\frac{3}{2}}, F' = 3\}$ hyperfine state with an accuracy $\leq$ 2 MHz. We employ lock-in detection technique to improve the signal to noise ratio of the Rydberg EIT signal. This measurement provides us an accurate knowledge of the Rydberg levels, which is

essential due to the various applications of Rydberg atoms in Quantum technology. All the experimental details are explained in chapter 3.

In chapter 3 we have used EIT spectroscopy of a three ladder level type system in a counter-propagation configuration to measure the transition frequencies of Rydberg levels. This configuration is used so as to reduce the effect of Doppler shift on the EIT signal. However, we perform quantum magnetometry in both counter-propagating and co-propagating configurations. We compare the effect of Doppler shift on Rydberg EIT in both the configurations. We observe that the co-propagating Rydberg EIT signal is broader than that of the counter-propagating one. The ratio of their linewidths is $|\frac{\omega_p+\omega_c}{\omega_p-\omega_c}| \approx 4.2$. The Doppler shift also reflects on the Zeeman splitting of the Rydberg EIT signals in the presence of magnetic field. We report that the Rydberg EIT signal in the co-propagating configuration shows an enhanced response to the magnetic field as compared to that in the counter-propagating configuration. The ratio of their response to the same magnetic field is $|\frac{\omega_p+\omega_c}{\omega_p-\omega_c}|$. The experimental measurements as well as the results of the theoretical modelling are provided in chapter 4.

Chapter 5 provides the details of the experimental set for cooling and trapping atoms in a Magneto-optical trap (MOT) and optical dipole trap. I have also discussed the experimental technique to measure the temperature of the cold atoms. We perform sub-Doppler cooling of cold atoms trapped in MOT. The temperature of the cold atoms after the sub-Doppler cooling is measured to be around 25 μK. We are in the process of optimizing it further to reduce the temperature to lower values as it will improve the lifetime of atoms in the dipole trap. I have discussed the process of trapping single atoms in the dipole trap as one of our future objectives in our experiment is to trap single atoms in a array of optical tweezers.

Rydberg atoms have high dipole moments and hence they have strong dipole-dipole and Van der Waals interactions. We record the Autler-Townes splitting (ATS) of different Rydberg states by varying the principal quantum numbers of the Rydberg states. The Van der Waals interaction between Rydberg atoms varies as $\propto n^{11}$, 'n' being the principal quantum number. We observe that the recorded ATS spectra show broadening effects as the principal quantum number is increased. We

investigate theoretically that the broadening is happening as a result of increasing dephasing rates of the Rydberg states due to the enhanced Van der Waals interaction between Rydberg atoms. The measurements are described in chapter 6.

Chapter 7 provides the study of Rydberg excitation mediated trap loss spectra in cold atoms. In this chapter, we use two-photon excitation scheme for exciting the atoms to the Rydberg states. OThe Rydberg excitation causes loss of atoms from the trap. We record the trap loss by varying effective two-photon Rabi frequency (keeping the excitation time at constant value) and varying the excitation time (keeping the effective two-photon Rabi frequency at constant value). We repeat the same experiment at different principal quantum numbers and show that the trap loss increases with the principal quantum numbers when effective two-photon Rabi frequency and excitation time are kept at fixed values. The possible reasons for this behavior have been discussed in chapter 7.

8.2 Future perspective

This section is dedicated to the future plans and novel experiments to be performed in our experimental setup. We have performed quantum sensing of magnetic field on room-temperature atoms using a three-level ladder-type system in a co-propagating and counter-propagating configurations. We observe that the Rydberg EIT in the co-propagating configurarion has enhanced response to the magnetic field as compared to the Rydberg EIT in counter-propagating configuration. However, one disadvantage is that the linewidth of the co-propagating EIT signal is 4.2 times more than that of the counter-propagating EIT. An improvement in this direction will be to reduce the linewidth of the Rydberg EIT signal in the co-propagating configurarion to improve the measurement of the magnetic field by incorporating different coupling beams with Laguerre-Gaussian modes [146].

In this thesis, cold atom experiments are performed in a Magneto-optical trap (MOT). Our subsequent plan is to trap the cold atoms in a dipole trap or optical tweezers. We will use far-off resonant trap (FORT) with the trapping laser having a wavelength of 852 nm. Our vacuum chamber is equipped with a pair of HNA

(high numerical aperture) lenses to focus the far-off resonant laser beam to sub-micron size and the atoms will be trapped in a maximum light shift region which is corresponding to the maximum intensity. We have also achieved sub-Doppler cooling of atoms in the MOT. We aim to load the atoms in the dipole trap after the sub-Doppler cooling stage. Our first goal is to trap atoms in a dipole trap before going to single atom trapping in an optical tweezer. We recently procured a Spatial Light Modulator (SLM) from Meadowlark Optics (XY phase series, 8 bit) for this purpose. SLM works by using liquid crystal technology, where refractive index of the individual pixels (liquid crystal) can be controlled by applying voltage. In the near future, we plan to use the SLM [147] to generate an array of optical tweezers for trapping single atoms. This will help us to implement high fidelity quantum gates for quantum information processing and computing. Single atoms in an array of optical tweezers is a great platform to simulate [148, 149] real-world complex systems [41, 46].

APPENDIX A

Switching circuit for MOT coils

A.1 IGBT switching circuit

IGBT switching circuit is based on a IGBT (Insulated Gated Bipolar Transistor) transistor, the transistor is used for high speed switching.

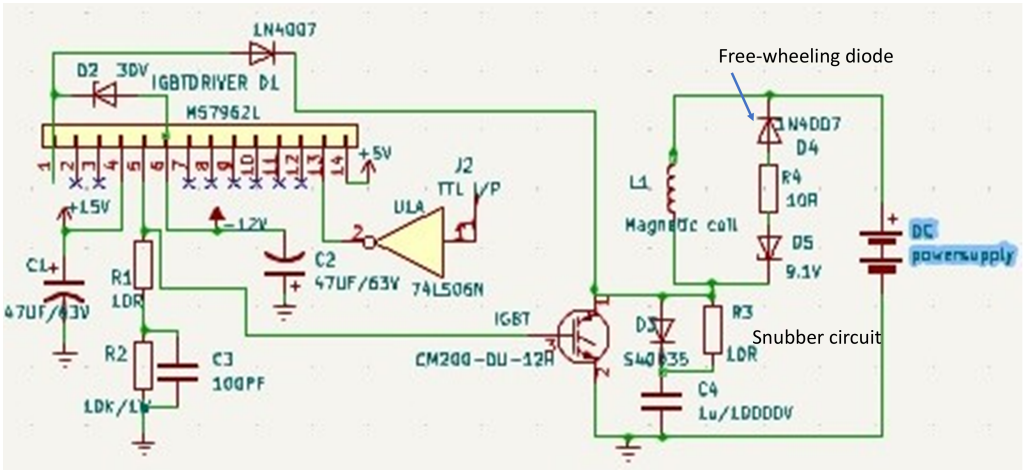


Figure A.1: IGBT switching circuit

The switching circuit consists of mainly two modules: one is IGBT transistor (Mitsubishi CM200-DU-12F) and another is IGBT driver (M57962L). IGBT driver is used to convert logic input signals (0 volt: low, +5 volt: high) into optimal

voltages (-12 volt and +15 volt, respectively) to drive the IGBT module. The IGBT module is switched on if the output voltage of the IGBT driver is +12 volt. Another function of the IGBT driver is to isolate the input signals from the driver with the help of fast optocouplers which have 15000 V/ms common mode transient immunity.

Different types of surge voltages are appeared when the IGBT is switched off suddenly.

- Back EMF

  Each of our magnetic coils has 26 layers and 26 turns in each layer. The total resistance and inductance of each coil are 5 ohms and 30 mH, respectively. The back emf is generated due to the sudden switch off of the circuit is $e = -L\frac{di}{dt}$. We use a fast switching diode and low resistance (which also has low inductance) in series across the coil to suppress the back emf. The diode is also called free-wheeling diode, and it is used in reverse bias.

- Surge voltage across the IGBT

  There is another possibility of generation of high voltage across the IGBT because of its parasitic inductance (L_b). In a similar way, the surge voltage is proportional to $-L_b\frac{di}{dt}$. A RCD (resistor-capacitor-diode) snubber circuit is used to suppress thesudden voltage spikes.

APPENDIX B

Cooling and Repumper SAS

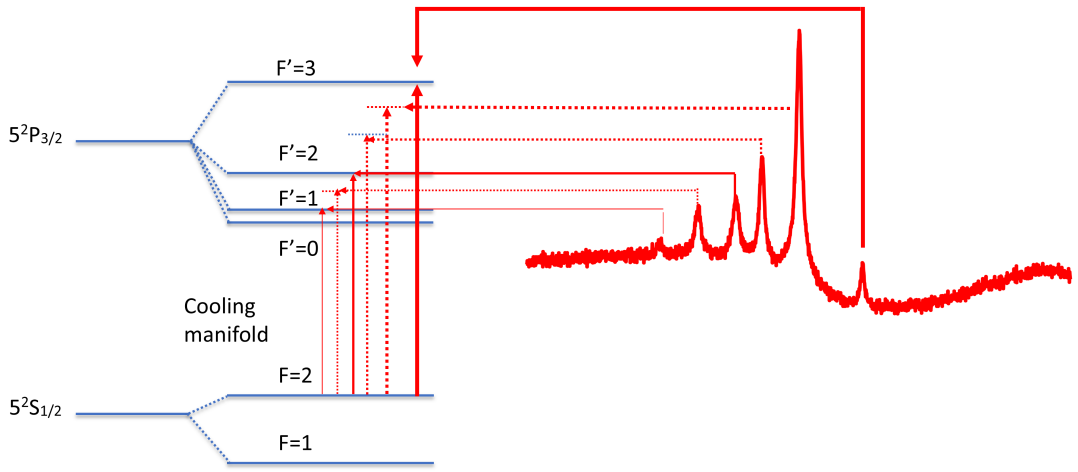


Figure B.1: Cooling manifold of ^{87}Rb atom, dotted arrows are cross-over transitions.

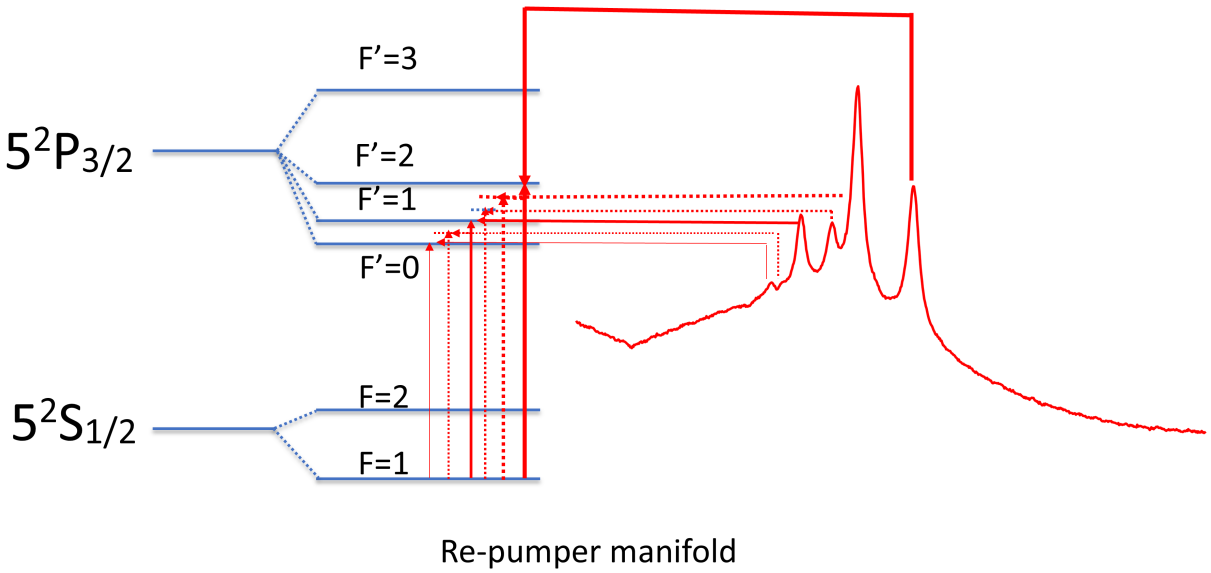


Figure B.2: Repump manifold of ^{87}Rb, dotted arrows are used to indicate cross-over transitions.

APPENDIX C

Simulation for other polarizations of probe and coupling laser

In Fig. C.1 we show the response for the σ^+-x and x-σ^+ polarizations. For the former, the steady state is almost identical to that of the σ^+-σ^- case discussed in the main text. Hence, both counter- and copropagating configurations exhibit a single peak given by Eq. (4.19). For the latter, the steady state is close to that of the σ^--σ^+ case, so we see a single dominant peak in both configurations; however, we can also discern a satellite peak for the counterpropagating case resulting from other two-photon resonances. Note that such a peak was observed in the experiment for the σ^--σ^+ setting [see Fig. 4.8(b)], which we attribute to an imperfect alignment of the lasers.

Figure C.2 shows when the probe is π polarized (parallel to the magnetic field) and the coupling laser is linearly polarized, the counterpropagating arrangement produces multiple peaks whereas the copropagating case exhibits only two shallow peaks. Now the dominant contribution comes from paths with $m_F^g = 0$, $m_F^e = 0$ and $m_J^r = \pm 1/2$ (cf. Fig. 4.7), hence from Eq. (4.18) the central peak separation is comparable in the two cases. This example illustrates the response can be sensitive to the polarizations.

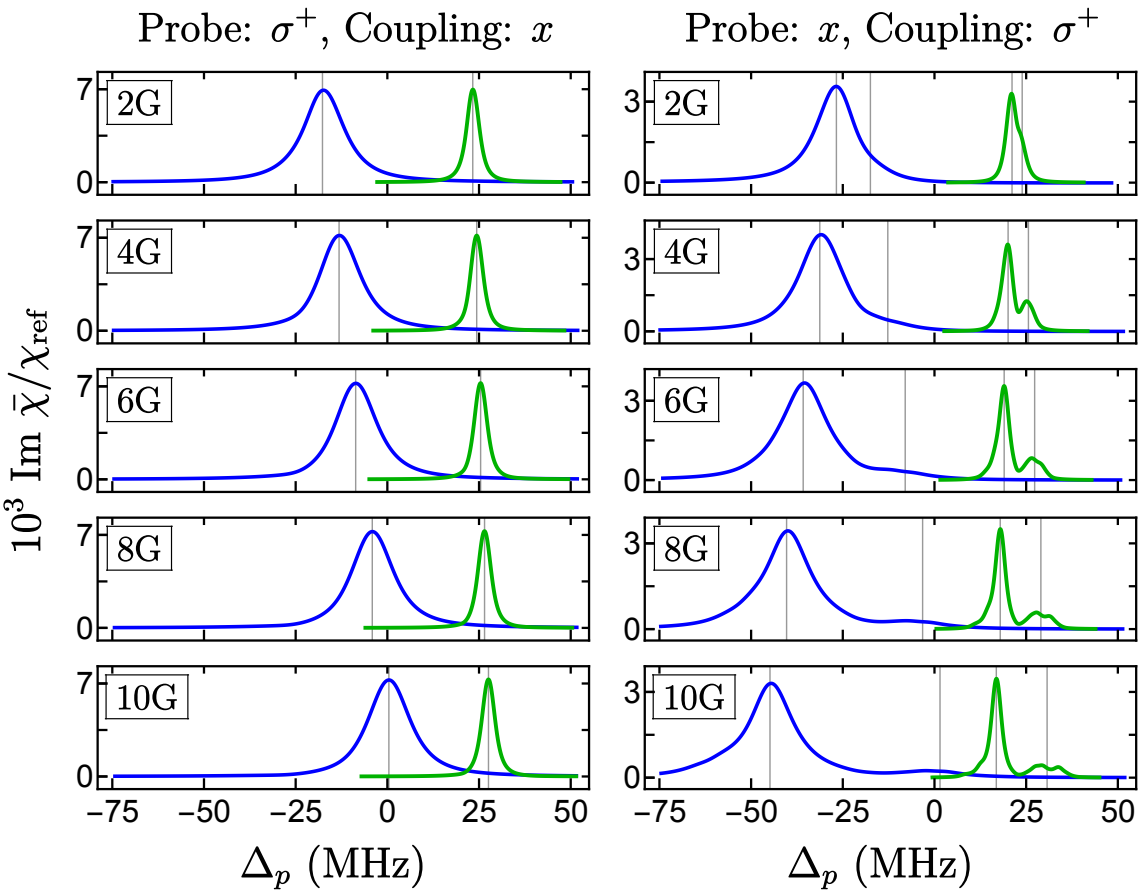


Figure C.1: Steady-state difference susceptibility with $\Delta_c = -36$ MHz for σ^+-x (left) and x-σ^+ (right) polarizations. For σ^+-x the peak follows $\Delta_p(B)$ from Eq. (4.19). For x-σ^+ the dominant peak follows $\Delta_p(-B)$; the other line is obtained from Eq. (4.18) with $(m_F^g, m_F^e, m_J^r) = (-1, -2, 1/2)$ for counterpropagating (green) and $(0, 1, -1/2)$ for copropagating (blue) geometries.

C.1 Parameter values used for measurements and numerical simulations

The power and beam radius of the probe laser were set to 0.015 mW and 699 μm, respectively. For the coupling laser we used a beam radius of 731.5 μm for copropagating arrangements and 1227 μm for counterpropagating arrangements. Table C.1 lists the values of the coupling laser power used for the different cases.

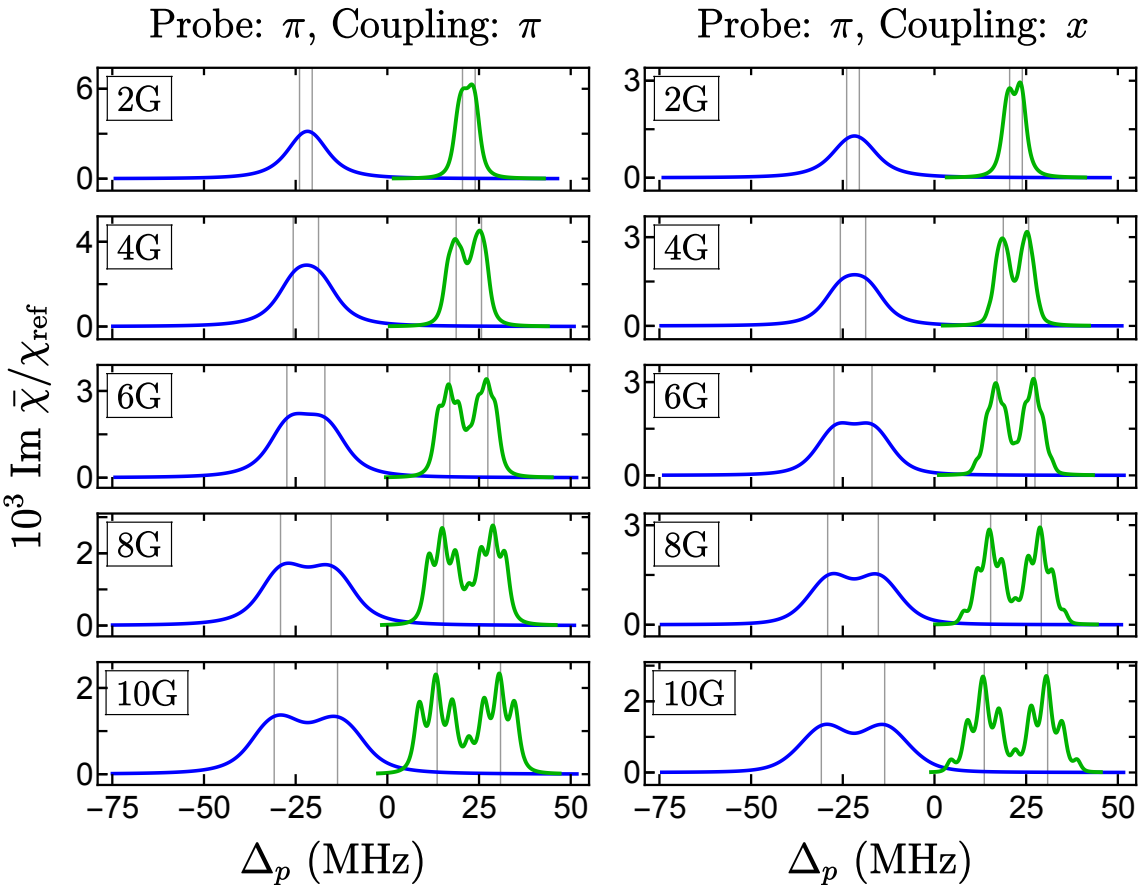


Figure C.2: Steady-state difference susceptibility with $\Delta_c = -36$ MHz for π-π (left) and π-x (right) polarizations. For both counterpropagating (green) and copropagating (blue) cases the vertical lines tracking the peaks are obtained from Eq. (4.18) with $(m_F^g, m_F^e, m_J^r) = (0, 0, \pm 1/2)$.

Table C.1: Coupling laser power P_c used in different plots.

Figure	Arrangement	P_c (mW)
Figure 4.4	$T = 0$	220
Figure 4.6	Counterpropagating	50
Figure 4.6	Copropagating	250
Figure 4.8	Counterpropagating	220
Figure 4.8	Copropagating	220
Figure 4.9	Counterpropagating	20
Figure 4.9	Copropagating	150
Figure C.1	Counterpropagating	20
Figure C.1	Copropagating	150
Figure C.2	Counterpropagating	20
Figure C.2	Copropagating	150
Figure 4.5	Counterpropagating	20
Figure 4.5	Copropagating	150

Bibliography

[1] T. Gallagher, "Rydberg Atoms," in *Springer Handbook of Atomic*, p. 235, 2006. (document)

[2] J. Wang, J. Bai, J. He, and J. Wang, "Single-photon cesium rydberg excitation spectroscopy using 318.6-nm uv laser and room-temperature vapor cell," *Optics Express*, vol. 25, no. 19, pp. 22510–22518, 2017. (document)

[3] A. Facon, E.-K. Dietsche, D. Grosso, S. Haroche, J.-M. Raimond, M. Brune, and S. Gleyzes, "A sensitive electrometer based on a rydberg atom in a schrödinger-cat state," *Nature*, vol. 535, no. 7611, pp. 262–265, 2016. (document), 3.4

[4] H. Fan, S. Kumar, J. Sedlacek, H. Kübler, S. Karimkashi, and J. P. Shaffer, "Atom based rf electric field sensing," *Journal of Physics B: Atomic, Molecular and Optical Physics*, vol. 48, no. 20, p. 202001, 2015. (document)

[5] M. Saffman and T. Walker, "Analysis of a quantum logic device based on dipole-dipole interactions of optically trapped rydberg atoms," *Physical Review A*, vol. 72, no. 2, p. 022347, 2005. (document)

[6] M. Berholts, R. Knut, R. Stefanuik, H. Wikmark, S. Saha, and J. Söderström, "Quantum watch and its intrinsic proof of accuracy," *Physical Review Research*, vol. 4, no. 4, p. 043041, 2022. (document)

[7] M. D. Lukin, M. Fleischhauer, R. Cote, L. Duan, D. Jaksch, J. I. Cirac, and P. Zoller, "Dipole blockade and quantum information processing in mesoscopic atomic ensembles," *Physical review letters*, vol. 87, no. 3, p. 037901, 2001. (document)

[8] E. Urban, T. A. Johnson, T. Henage, L. Isenhower, D. Yavuz, T. Walker, and M. Saffman, "Observation of rydberg blockade between two atoms," *Nature Physics*, vol. 5, no. 2, pp. 110–114, 2009. (document), 1, 2.2.3

[9] A. Gaëtan, Y. Miroshnychenko, T. Wilk, A. Chotia, M. Viteau, D. Comparat, A. Pillet, Pierre Browaeys, and P. Grangier, "Observation of collective excitation of two individual atoms in the rydberg blockade regime," *Nature Physics*, vol. 5, pp. 115–118, 2009. (document)

[10] T. Wilk, A. Gaëtan, C. Evellin, J. Wolters, Y. Miroshnychenko, P. Grangier, and A. Browaeys, "Entanglement of two individual neutral atoms using rydberg blockade," *Phys. Rev. Lett.*, vol. 104, p. 010502, Jan 2010. (document)

[11] X.-F. Shi and Y. Lu, "Quantum gates with weak van der waals interactions of neutral rydberg atoms," *Physical Review A*, vol. 104, no. 1, p. 012615, 2021. (document)

[12] E. Distante, P. Farrera, A. Padrón-Brito, D. Paredes-Barato, G. Heinze, and H. De Riedmatten, "Storing single photons emitted by a quantum memory on a highly excited rydberg state," *Nature communications*, vol. 8, no. 1, p. 14072, 2017. (document)

[13] K.-J. Boller, A. Imamoğlu, and S. E. Harris, "Observation of electromagnetically induced transparency," *Phys. Rev. Lett.*, vol. 66, pp. 2593–2596, May 1991. (document)

[14] A. K. Mohapatra, T. R. Jackson, and C. S. Adams, "Coherent optical detection of highly excited rydberg states using electromagnetically induced transparency," *Phys. Rev. Lett.*, vol. 98, p. 113003, Mar 2007. (document)

[15] J. A. Sedlacek, A. Schwettmann, H. Kübler, R. Löw, T. Pfau, and J. P. Shaffer, "Microwave electrometry with rydberg atoms in a vapour cell using bright atomic resonances," *Nature physics*, vol. 8, no. 11, pp. 819–824, 2012. (document), 3.4

[16] D. A. Anderson, S. A. Miller, G. Raithel, J. Gordon, M. Butler, and C. Holloway, "Optical measurements of strong microwave fields with rydberg atoms in a vapor cell," *Physical Review Applied*, vol. 5, no. 3, p. 034003, 2016. (document)

[17] H. Jen, B. Xiong, A. Y. Ite, and D.-W. Wang, "Electromagnetically induced transparency and slow light in quantum degenerate atomic gases," *JOSA B*, vol. 30, no. 11, pp. 2855–2863, 2013. (document)

[18] M. T. Simons, A. B. Artusio-Glimpse, A. K. Robinson, N. Prajapati, and C. L. Holloway, "Rydberg atom-based sensors for radio-frequency electric field metrology, sensing, and communications," *Measurement: Sensors*, vol. 18, p. 100273, 2021. (document), 1

[19] W. Bowden, R. Hobson, P. Huillery, P. Gill, M. Jones, and I. R. Hill, "Rydberg electrometry for optical lattice clocks," *Physical Review A*, vol. 96, no. 2, p. 023419, 2017. (document)

[20] C. Halter, A. Miethke, C. Sillus, A. Hegde, and A. Görlitz, "Trap-loss spectroscopy of rydberg states in ytterbium," *Journal of Physics B: Atomic, Molecular and Optical Physics*, vol. 56, 02 2023. (document)

[21] R. Grimm, M. Weidemüller, and Y. B. Ovchinnikov, "Optical dipole traps for neutral atoms," in *Advances in atomic, molecular, and optical physics*, vol. 42, pp. 95–170, Elsevier, 2000. (document), 5.2, 5.2, 5.2

[22] J. He, B.-d. Yang, Y.-j. Cheng, T.-c. Zhang, and J.-m. Wang, "Extending the trapping lifetime of single atom in a microscopic far-off-resonance optical dipole trap," *Frontiers of Physics*, vol. 6, pp. 262–270, 2011. (document), 5.2, 5.2

[23] E. Dietsche, A. Larrouy, S. Haroche, J. Raimond, M. Brune, and S. Gleyzes, "High-sensitivity magnetometry with a single atom in a superposition of two circular rydberg states," *Nature Physics*, vol. 15, no. 4, pp. 326–329, 2019. (document)

[24] H. Bernien, S. Schwartz, A. Keesling, H. Levine, A. Omran, H. Pichler, S. Choi, A. S. Zibrov, M. Endres, M. Greiner, *et al.*, "Probing many-body dynamics on a 51-atom quantum simulator," *Nature*, vol. 551, no. 7682, pp. 579–584, 2017. (document)

[25] R. Dumke, M. Volk, T. Müther, F. B. J. Buchkremer, G. Birkl, and W. Ertmer, "Micro-optical realization of arrays of selectively addressable dipole traps: A scalable configuration for quantum computation with atomic qubits," *Phys. Rev. Lett.*, vol. 89, p. 097903, Aug 2002. (document)

[26] A. Duspayev, C. Owens, B. Dash, and G. Raithel, "An optical atomic clock using $4d\_j$ states of rubidium," *arXiv preprint arXiv:2406.09352*, 2024. 1

[27] H. F. Rice, V. Benischek, and L. Sczaniecki, "Application of atom interferometric technology for gps independent navigation and time solutions," in *2018 IEEE/ION Position, Location and Navigation Symposium (PLANS)*, pp. 1097–1106, IEEE, 2018. 1

[28] C. L. Degen, F. Reinhard, and P. Cappellaro, "Quantum sensing," *Reviews of modern physics*, vol. 89, no. 3, p. 035002, 2017. 1

[29] C. T. Fancher, D. R. Scherer, M. C. S. John, and B. L. S. Marlow, "Rydberg atom electric field sensors for communications and sensing," *IEEE Transactions on Quantum Engineering*, vol. 2, pp. 1–13, 2021. 1, 2.2

[30] D. Bouwmeester and A. Zeilinger, "The physics of quantum information: basic concepts," in *The physics of quantum information: quantum cryptography, quantum teleportation, quantum computation*, pp. 1–14, Springer, 2000. 1

[31] C. Monroe, "Quantum information processing with atoms and photons," *Nature*, vol. 416, no. 6877, pp. 238–246, 2002. 1

[32] M. Saffman, T. G. Walker, and K. Mølmer, "Quantum information with rydberg atoms," *Reviews of modern physics*, vol. 82, no. 3, pp. 2313–2363, 2010. 1

[33] J. Gué, A. Hees, J. Lodewyck, R. Le Targat, and P. Wolf, "Search for vector dark matter in microwave cavities with rydberg atoms," *Physical Review D*, vol. 108, no. 3, p. 035042, 2023. 1

[34] T. F. Gallagher, "Rydberg atoms," in *Springer Handbook of Atomic, Molecular, and Optical Physics*, pp. 231–240, Springer, 1994. 1, 2.2, 3.3, 3.3, 7.2.4

[35] C. S. Adams, J. D. Pritchard, and J. P. Shaffer, "Rydberg atom quantum technologies," *Journal of Physics B: Atomic, Molecular and Optical Physics*, vol. 53, no. 1, p. 012002, 2019. 1, 3, 7.2.4

[36] S. E. Harris, "Electromagnetically induced transparency," *Physics today*, vol. 50, no. 7, pp. 36–42, 1997. 1

[37] L. A. Downes, L. Torralbo-Campo, and K. J. Weatherill, "A practical guide to terahertz imaging using thermal atomic vapour," *New Journal of Physics*, vol. 25, no. 3, p. 035002, 2023. 1

[38] C. G. Wade, N. Šibalić, N. R. De Melo, J. M. Kondo, C. S. Adams, and K. J. Weatherill, "Real-time near-field terahertz imaging with atomic optical fluorescence," *Nature Photonics*, vol. 11, no. 1, pp. 40–43, 2017. 1

[39] D. Li, Z. Bai, X. Zuo, Y. Wu, J. Sheng, and H. Wu, "Room temperature single-photon terahertz detection with thermal rydberg atoms," *arXiv preprint arXiv:2403.05833*, 2024. 1

[40] S. Haroche, "Nobel lecture: Controlling photons in a box and exploring the quantum to classical boundary," *Rev. Mod. Phys.*, vol. 85, pp. 1083–1102, Jul 2013. 1

[41] P. Schauss, "Quantum simulation of transverse ising models with rydberg atoms," *Quantum Science and Technology*, vol. 3, no. 2, p. 023001, 2018. 1, 8.2

[42] D. Stuart and A. Kuhn, "Single-atom trapping and transport in dmd-controlled optical tweezers," *New Journal of Physics*, vol. 20, no. 2, p. 023013, 2018. 1

[43] G. Gauthier, I. Lenton, N. M. Parry, M. Baker, M. Davis, H. Rubinsztein-Dunlop, and T. Neely, "Configurable microscopic optical potentials for bose-einstein condensates using a digital-micromirror device," *arXiv preprint arXiv:1605.04928*, 2016. 1

[44] E. Schonbrun, R. Piestun, P. Jordan, J. Cooper, K. D. Wulff, J. Courtial, and M. Padgett, "3d interferometric optical tweezers using a single spatial light modulator," *Optics express*, vol. 13, no. 10, pp. 3777–3786, 2005. 1

[45] H. Labuhn, D. Barredo, S. Ravets, S. De Léséleuc, T. Macrì, T. Lahaye, and A. Browaeys, "Tunable two-dimensional arrays of single rydberg atoms for realizing quantum ising models," *Nature*, vol. 534, no. 7609, pp. 667–670, 2016. 1

[46] T. L. Nguyen, J.-M. Raimond, C. Sayrin, R. Cortinas, T. Cantat-Moltrecht, F. Assemat, I. Dotsenko, S. Gleyzes, S. Haroche, G. Roux, *et al.*, "Towards quantum simulation with circular rydberg atoms," *Physical Review X*, vol. 8, no. 1, p. 011032, 2018. 1, 8.2

[47] X. Zhang, A. Gill, L. Isenhower, T. Walker, and M. Saffman, "Fidelity of a rydberg-blockade quantum gate from simulated quantum process tomography," *Physical Review A—Atomic, Molecular, and Optical Physics*, vol. 85, no. 4, p. 042310, 2012. 1

[48] H. Levine, A. Keesling, A. Omran, H. Bernien, S. Schwartz, A. S. Zibrov, M. Endres, M. Greiner, V. Vuletić, and M. D. Lukin, "High-fidelity control and entanglement of rydberg-atom qubits," *Physical review letters*, vol. 121, no. 12, p. 123603, 2018. 1

[49] A. J. Daley, "Quantum trajectories and open many-body quantum systems," *Adv. Phys.*, vol. 63, no. 2, p. 77, 2014. 2.1.1

[50] M. Fleischhauer, A. Imamoglu, and J. P. Marangos, "Electromagnetically induced transparency: Optics in coherent media," *Rev. Mod. Phys.*, vol. 77, pp. 633–673, Jul 2005. 2.1.1

[51] J. P. Marangos, "Electromagnetically induced transparency," *Journal of modern optics*, vol. 45, no. 3, pp. 471–503, 1998. 2.1.2

[52] M. Fleischhauer, A. Imamoglu, and J. P. Marangos, "Electromagnetically induced transparency: Optics in coherent media," *Reviews of modern physics*, vol. 77, no. 2, pp. 633–673, 2005. 2.1.2

[53] J. R. Rydberg, "Xxxiv. on the structure of the line-spectra of the chemical elements," *The London, Edinburgh, and Dublin philosophical magazine and journal of science*, vol. 29, no. 179, pp. 331–337, 1890. 2.2

[54] W. Li, I. Mourachko, M. Noel, and T. Gallagher, "Millimeter-wave spectroscopy of cold rb rydberg atoms in a magneto-optical trap: Quantum defects of the ns, np, and nd series," *Physical Review A*, vol. 67, no. 5, p. 052502, 2003. 2.2, 3.3

[55] M. Seaton, "Quantum defect theory," in *Molecular Applications of Quantum Defect Theory*, pp. 108–198, Routledge, 2019. 2.2

[56] Z. Lai, S. Zhang, Q. Gou, and Y. Li, "Polarizabilities of rydberg states of rb atoms with n up to 140," *Physical Review A*, vol. 98, no. 5, p. 052503, 2018. 2.2

[57] M. Piotrowicz, C. MacCormick, A. Kowalczyk, S. Bergamini, I. Beterov, and E. Yakshina, "Measurement of the electric dipole moments for transitions to rubidium rydberg states via autler–townes splitting," *New Journal of Physics*, vol. 13, no. 9, p. 093012, 2011. 2.2

[58] V. Yerokhin, S. Buhmann, S. Fritzsche, and A. Surzhykov, "Electric dipole polarizabilities of rydberg states of alkali-metal atoms," *Physical Review A*, vol. 94, no. 3, p. 032503, 2016. 2.2

[59] T. F. Gallagher and P. Pillet, "Dipole–dipole interactions of rydberg atoms," *Advances in Atomic, Molecular, and Optical Physics*, vol. 56, pp. 161–218, 2008. 2.2, 7.2.4

[60] E. Altiere, D. P. Fahey, M. W. Noel, R. J. Smith, and T. J. Carroll, "Dipole-dipole interaction between rubidium rydberg atoms," *Physical Review A—Atomic, Molecular, and Optical Physics*, vol. 84, no. 5, p. 053431, 2011. 2.2, 7.2.4

[61] D. B. Branden, T. Juhasz, T. Mahlokozera, C. Vesa, R. O. Wilson, M. Zheng, A. Kortyna, and D. A. Tate, "Radiative lifetime measurements of rubidium rydberg states," *Journal of Physics B: atomic, molecular and optical physics*, vol. 43, no. 1, p. 015002, 2009. 2.2, 4.4

[62] J. Yuan, W. Yang, M. Jing, H. Zhang, Y. Jiao, W. Li, L. Zhang, L. Xiao, and S. Jia, "Quantum sensing of microwave electric fields based on rydberg atoms," *Reports on Progress in Physics*, 2023. 2.2

[63] A. Duspayev, R. Cardman, D. A. Anderson, and G. Raithel, "High-angular-momentum rydberg states in a room-temperature vapor cell for dc electric-field sensing," *Physical Review Research*, vol. 6, no. 2, p. 023138, 2024. 2.2

[64] J. Yuan, T. Jin, Y. Yan, L. Xiao, S. Jia, and L. Wang, "A rydberg atom-based amplitude-modulated receiver using the dual-tone microwave field," *EPJ Quantum Technology*, vol. 11, no. 1, p. 2, 2024. 2.2

[65] N. Schlossberger, A. P. Rotunno, A. B. Artusio-Glimpse, N. Prajapati, S. Berweger, D. Shylla, M. T. Simons, and C. L. Holloway, "Zeeman-resolved autler-townes splitting in rydberg atoms with tunable resonances and a single transition dipole moment," *Physical Review A*, vol. 109, no. 2, p. L021702, 2024. 2.2

[66] M. Ma, S. Wang, Y. Yan, J. Yuan, L. Zhang, L. Wang, L. Xiao, and S. Jia, "Large power dynamic range microwave electric field sensing in a vapor cell," *Optics Express*, vol. 32, no. 20, pp. 35202–35211, 2024. 2.2

[67] B. Wu, R. Mao, Y. Liu, D. Sang, Y. Zhou, Y. Lin, Q. An, and Y. Fu, "Enhancing sensitivity of atomic microwave receiver combining laser arrays," *arXiv preprint arXiv:2403.14132*, 2024. 2.2

[68] M. V. Romalis, J. Wiedemann, S. Zhang, and N. Dural, "Vapor cell rydberg atom electrometry with time-separated fields," *arXiv preprint arXiv:2406.05106*, 2024. 2.2

[69] G. Hong, W. Teng, L. Bin, and L. Yuan-Xing, "Quantum sensing (): technologies and typical examples," *PHYSICS*, vol. 53, no. 6, pp. 384–394, 2024. 2.2

[70] A. A. Rahman, "Levitated magnetic particles as ac magnetic field sensors," in *Quantum Sensing, Imaging, and Precision Metrology II*, vol. 12912, pp. 271–274, SPIE, 2024. 2.2

[71] D. H. Meyer, C. O'Brien, D. P. Fahey, K. C. Cox, and P. D. Kunz, "Optimal atomic quantum sensing using electromagnetically-induced-transparency readout," *Physical Review A*, vol. 104, no. 4, p. 043103, 2021. 2.2

[72] N. Prajapati, N. Bhusal, A. P. Rotunno, S. Berweger, M. T. Simons, A. B. Artusio-Glimpse, Y. Ju Wang, E. Bottomley, H. Fan, and C. L. Holloway, "Sensitivity comparison of two-photon vs three-photon rydberg electrometry," *Journal of Applied Physics*, vol. 134, no. 2, 2023. 2.2

[73] D. H. Meyer, Z. A. Castillo, K. C. Cox, and P. D. Kunz, "Assessment of rydberg atoms for wideband electric field sensing," *Journal of Physics B: Atomic, Molecular and Optical Physics*, vol. 53, no. 3, p. 034001, 2020. 2.2

[74] B. Liu, L. Zhang, Z. Liu, Z. Deng, D. Ding, B. Shi, and G. Guo, "Electric field measurement and application based on rydberg atoms," *Electromagnetic Science*, vol. 1, no. 2, pp. 1–16, 2023. 2.2

[75] E. J. Robertson, N. Šibalić, R. M. Potvliege, and M. P. Jones, "Arc 3.0: An expanded python toolbox for atomic physics calculations," *Computer Physics Communications*, vol. 261, p. 107814, 2021. 2.2.1

[76] I. Beterov, I. Ryabtsev, D. Tretyakov, and V. Entin, "Quasiclassical calculations of blackbody-radiation-induced depopulation rates and effective lifetimes of rydberg n s, n p, and n d alkali-metal atoms with n 80," *Physical Review A—Atomic, Molecular, and Optical Physics*, vol. 79, no. 5, p. 052504, 2009. 2.2.1, 2.2.1, 2.2.1

[77] L. D'yachkov and P. Pankratov, "On the use of the semiclassical approximation for the calculation of oscillator strengths and photoionization cross sections," *Journal of Physics B: Atomic, Molecular and Optical Physics*, vol. 27, no. 3, p. 461, 1994. 2.2.1

[78] R. J. Le Roy, "Long-range potential coefficients from rkr turning points: C 6 and c 8 for b (3πou+)-state cl2, br2, and i2," *Canadian Journal of Physics*, vol. 52, no. 3, pp. 246–256, 1974. 2.2.2

[79] K. Singer, J. Stanojevic, M. Weidemüller, and R. Côté, "Long-range interactions between alkali rydberg atom pairs correlated to the ns–ns, np–np and

nd–nd asymptotes," *Journal of Physics B: Atomic, Molecular and Optical Physics*, vol. 38, no. 2, p. S295, 2005. 2.2.2

[80] C. S. E. van Ditzhuijzen *et al.*, *Dipole-dipole interaction between cold Rydberg atoms*. PhD thesis, PhD thesis (in progress), 2009. 2.2.2

[81] N. Šibalic and C. S. Adams, "Rydberg physics," *Rydberg physics*, pp. 2399–2891, 2018. 2.2.2

[82] C.-E. Wu, T. Kirova, M. Auzins, and Y.-H. Chen, "Rydberg-rydberg interaction strengths and dipole blockade radii in the presence of förster resonances," *Optics Express*, vol. 31, no. 22, pp. 37094–37104, 2023. 2.2.2, 2.2.3

[83] A. Gaëtan, Y. Miroshnychenko, T. Wilk, A. Chotia, M. Viteau, D. Comparat, P. Pillet, A. Browaeys, and P. Grangier, "Observation of collective excitation of two individual atoms in the rydberg blockade regime," *Nature Physics*, vol. 5, no. 2, pp. 115–118, 2009. 2.2.3

[84] T. Wilk, A. Gaëtan, C. Evellin, J. Wolters, Y. Miroshnychenko, P. Grangier, and A. Browaeys, "Entanglement of two individual neutral atoms using rydberg blockade," *Physical review letters*, vol. 104, no. 1, p. 010502, 2010. 2.2.3

[85] R. Heidemann, U. Krohn, V. Bendkowsky, B. Butscher, R. Löw, L. Santos, and T. Pfau, "Evidence for coherent collective rydberg excitation in the strong blockade regime," *Physical Review Letters*, vol. 99, no. 16, p. 163601, 2007. 2.2.3

[86] J. Kumlin, C. Braun, C. Tresp, N. Stiesdal, S. Hofferberth, and A. Paris-Mandoki, "Quantum optics with rydberg superatoms," *Journal of Physics Communications*, vol. 7, no. 5, p. 052001, 2023. 2.2.3

[87] X.-Q. Shao, S.-L. Su, L. Li, R. Nath, J.-H. Wu, and W. Li, "Rydberg superatoms: An artificial quantum system for quantum information processing and quantum optics," *Applied Physics Reviews*, vol. 11, no. 3, 2024. 2.2.3

[88] T. Weber, M. Höning, T. Niederprüm, T. Manthey, O. Thomas, V. Guarrera, M. Fleischhauer, G. Barontini, and H. Ott, "Mesoscopic rydberg-blockaded ensembles in the superatom regime and beyond," *Nature Physics*, vol. 11, no. 2, pp. 157–161, 2015. 2.2.3

[89] M. Aymar, C. H. Greene, and E. Luc-Koenig, "Multichannel rydberg spectroscopy of complex atoms," *Reviews of Modern Physics*, vol. 68, no. 4, p. 1015, 1996. 3.3, 3.3

[90] A. Tauschinsky, R. Newell, H. Van Linden van den Heuvell, and R. Spreeuw, "Measurement of 87 rb rydberg-state hyperfine splitting in a room-temperature vapor cell," *Physical Review A—Atomic, Molecular, and Optical Physics*, vol. 87, no. 4, p. 042522, 2013. 3.3, 3.3, 4.1.3

[91] S. Li, J. Yuan, L. Wang, L. Xiao, and S. Jia, "Measurement of the quantum defects of 85rb p and f-series via microwave-assisted electromagnetically induced transparency spectroscopy," *Results in Physics*, vol. 29, p. 104728, 2021. 3.3

[92] B. Sanguinetti, H. Majeed, M. Jones, and B. Varcoe, "Precision measurements of quantum defects in the np3/2 rydberg states of 85rb," *Journal of Physics B: Atomic, Molecular and Optical Physics*, vol. 42, no. 16, p. 165004, 2009. 3.3

[93] A. Ramos, R. Cardman, and G. Raithel, "Measurement of the hyperfine coupling constant for n s 1/2 rydberg states of rb 85," *Physical Review A*, vol. 100, no. 6, p. 062515, 2019. 3.3

[94] S. R. Cohen and J. D. Thompson, "Quantum computing with circular rydberg atoms," *PRX Quantum*, vol. 2, no. 3, p. 030322, 2021. 3.4

[95] D. A. Steck, "Rubidium 87 d line data," 2001. 4.1.1, 4.4, 5.1.1, 5.1.2, 5.1.4

[96] E. Arimondo, M. Inguscio, and P. Violino, "Experimental determinations of the hyperfine structure in the alkali atoms," *Rev. Mod. Phys.*, vol. 49, pp. 31–75, Jan 1977. 4.1.2

[97] J. B. Naber, A. Tauschinsky, H. B. van Linden van den Heuvell, and R. J. C. Spreeuw, "Electromagnetically induced transparency with Rydberg atoms across the Breit-Rabi regime," *SciPost Phys.*, vol. 2, p. 015, 2017. 4.1.3

[98] J. B. Naber, A. Tauschinsky, H. B. van Linden van den Heuvell, and R. J. C. Spreeuw, "Electromagnetically induced transparency with Rydberg atoms across the Breit-Rabi regime," *SciPost Phys.*, vol. 2, p. 015, 2017. 4.4

[99] N. Šibalić, J. D. Pritchard, C. S. Adams, and K. J. Weatherill, "ARC: An open-source library for calculating properties of alkali Rydberg atoms," *Comput. Phys. Commun.*, vol. 220, p. 319, 2017. 4.4

[100] A. Tauschinsky, R. Newell, H. B. van Linden van den Heuvell, and R. J. C. Spreeuw, "Measurement of ^{87}Rb Rydberg-state hyperfine splitting in a room-temperature vapor cell," *Phys. Rev. A*, vol. 87, p. 042522, Apr 2013. 4.4

[101] M. Swar, D. Roy, D. D, S. Chaudhuri, S. Roy, and H. Ramachandran, "Measurements of spin properties of atomic systems in and out of equilibrium via noise spectroscopy," *Opt. Express*, vol. 26, pp. 32168–32183, Nov 2018. 4.4

[102] V. S. Chauhan, R. Kumar, D. Manchaiah, P. Kumar, and R. K. Easwaran, "Narrowing of electromagnetically induced transparency by using structured coupling light in 85rb atomic vapor medium," *Laser Physics*, vol. 30, p. 065203, may 2020. 4.5

[103] E. K. Dietsche, A. Larrouy, S. Haroche, J. M. Raimond, M. Brune, and S. Gleyzes, "High-sensitivity magnetometry with a single atom in a superposition of two circular Rydberg states," *Nat. Phys.*, vol. 15, no. 4, pp. 326–329, 2019. 4.5

[104] J. B. Brask, R. Chaves, and J. Kołodyński, "Improved quantum magnetometry beyond the standard quantum limit," *Phys. Rev. X*, vol. 5, p. 031010, Jul 2015. 4.5

[105] T. W. Hänsch and A. L. Schawlow, "Cooling of gases by laser radiation," *Optics Communications*, vol. 13, no. 1, pp. 68–69, 1975. 5

[106] S. Chu, "Nobel lecture: The manipulation of neutral particles," *Reviews of Modern Physics*, vol. 70, no. 3, p. 685, 1998. 5

[107] S. Chu, "Laser manipulation of atoms and particles," *Science*, vol. 253, no. 5022, pp. 861–866, 1991. 5

[108] E. L. Raab, M. Prentiss, A. Cable, S. Chu, and D. E. Pritchard, "Trapping of neutral sodium atoms with radiation pressure," *Physical review letters*, vol. 59, no. 23, p. 2631, 1987. 5

[109] P. Gould, "New measurements with optical molasses pl gould, pd lett, and wd phillips," in *Laser Spectroscopy VIII: Proceedings of the Eighth International Conference, Åre, Sweden, June 22-26, 1987*, p. 64, Springer-Verlag Berlin and Heidelberg GmbH & Co. K, 1987. 5

[110] W. D. Phillips, "Nobel lecture: Laser cooling and trapping of neutral atoms," *Reviews of Modern Physics*, vol. 70, no. 3, p. 721, 1998. 5, 5.1.4

[111] H. J. Metcalf and P. Van der Straten, *Laser cooling and trapping*. Springer Science & Business Media, 1999. 5.1.1

[112] S. Chu, L. Hollberg, J. E. Bjorkholm, A. Cable, and A. Ashkin, "Three-dimensional viscous confinement and cooling of atoms by resonance radiation pressure," *Physical review letters*, vol. 55, no. 1, p. 48, 1985. 5.1.4

[113] C. Cooper, G. Hillenbrand, J. Rink, C. Townsend, K. Zetie, and C. Foot, "The temperature of atoms in a magneto-optical trap," *Europhysics Letters*, vol. 28, no. 6, p. 397, 1994. 5.1.4

[114] P. Kohns, P. Buch, W. Süptitz, C. Csambal, and W. Ertmer, "On-line measurement of sub-doppler temperatures in a rb magneto-optical trap-by-trap centre oscillations," *Europhysics Letters*, vol. 22, no. 7, p. 517, 1993. 5.1.4

[115] P. D. Lett, R. N. Watts, C. I. Westbrook, W. D. Phillips, P. L. Gould, and H. J. Metcalf, "Observation of atoms laser cooled below the doppler limit," *Physical review letters*, vol. 61, no. 2, p. 169, 1988. 5.1.5

[116] C. Cohen-Tannoudji and A. Kastler, "I optical pumping," in *Progress in optics*, vol. 5, pp. 1–81, Elsevier, 1966. 5.1.5

[117] J. Dalibard and C. Cohen-Tannoudji, "Laser cooling below the doppler limit by polarization gradients: simple theoretical models," *JOSA B*, vol. 6, no. 11, pp. 2023–2045, 1989. 5.1.5, 5.1.5, 5.1.5, 5.1.5, 5.1.5

[118] Y.-S. Chin, M. Steiner, and C. Kurtsiefer, "Polarization gradient cooling of single atoms in optical dipole traps," *Physical Review A*, vol. 96, no. 3, p. 033406, 2017. 5.1.5

[119] A. Steane, G. Hillenbrand, and C. Foot, "Polarization gradient cooling in a one-dimensional sigma+-sigma-configuration for any atomic transition," *Journal of Physics B: Atomic, Molecular and Optical Physics*, vol. 25, no. 22, p. 4721, 1992. 5.1.5, 5.1.5

[120] O. Emile, R. Kaiser, C. Gerz, H. Wallis, A. Aspect, and C. Cohen-Tannoudji, "Magnetically assisted sisyphus effect," *Journal de Physique II*, vol. 3, no. 12, pp. 1709–1733, 1993. 5.1.5

[121] P. J. Ungar, D. S. Weiss, E. Riis, and S. Chu, "Optical molasses and multilevel atoms: theory," *JOSA B*, vol. 6, no. 11, pp. 2058–2071, 1989. 5.1.5

[122] A. Steane, M. Chowdhury, and C. Foot, "Radiation force in the magneto-optical trap," *JOSA B*, vol. 9, no. 12, pp. 2142–2158, 1992. 5.1.5

[123] M. Landini, S. Roy, L. Carcagní, D. Trypogeorgos, M. Fattori, M. Inguscio, and G. Modugno, "Sub-doppler laser cooling of potassium atoms," *Physical Review A—Atomic, Molecular, and Optical Physics*, vol. 84, no. 4, p. 043432, 2011. 5.1.5

[124] Z. Ji, J. Yuan, Y. Zhao, X. Chang, Y. Yang, L. Xiao, and S. Jia, "Optimization and analysis of experimental parameters for polarization gradient cooling in optical molasses," *arXiv preprint arXiv:1304.7066*, 2013. 5.1.5

[125] A. Ashkin, "Acceleration and trapping of particles by radiation pressure," *Physical review letters*, vol. 24, no. 4, p. 156, 1970. 5.2

[126] S. Chu, J. Bjorkholm, A. Ashkin, and A. Cable, "Experimental observation of optically trapped atoms," *Physical review letters*, vol. 57, no. 3, p. 314, 1986. 5.2

[127] W. Alt, D. Schrader, S. Kuhr, M. Müller, V. Gomer, and D. Meschede, "Single atoms in a standing-wave dipole trap," *Physical Review A*, vol. 67, no. 3, p. 033403, 2003. 5.2

[128] N. Schlosser, G. Reymond, and P. Grangier, "Collisional blockade in microscopic optical dipole traps," *Physical review letters*, vol. 89, no. 2, p. 023005, 2002. 5.2, 5.2

[129] Y. Fung and M. Andersen, "Efficient collisional blockade loading of a single atom into a tight microtrap," *New Journal of Physics*, vol. 17, no. 7, p. 073011, 2015. 5.2

[130] M. Weber, J. Volz, K. Saucke, C. Kurtsiefer, and H. Weinfurter, "Analysis of a single-atom dipole trap," *Physical Review A—Atomic, Molecular, and Optical Physics*, vol. 73, no. 4, p. 043406, 2006. 5.2

[131] T. Savard, K. O'hara, and J. Thomas, "Laser-noise-induced heating in far-off resonance optical traps," *Physical Review A*, vol. 56, no. 2, p. R1095, 1997. 5.2, 5.2

[132] J. Bai, S. Liu, J. Wang, J. He, and J. Wang, "Single-photon rydberg excitation and trap-loss spectroscopy of cold cesium atoms in a magneto-optical trap by using of a 319-nm ultraviolet laser system," *IEEE Journal of Selected Topics in Quantum Electronics*, vol. 26, no. 3, pp. 1–6, 2019. 6

[133] H. Zhang, L. Zhang, L. Wang, S. Bao, J. Zhao, S. Jia, and G. Raithel, "Autler-townes spectroscopy with interaction-induced dephasing," *Physical Review A*, vol. 90, no. 4, p. 043849, 2014. 6

[134] Q.-B. Liang, B.-D. Yang, J.-F. Yang, T.-C. Zhang, and J.-M. Wang, "Autler—townes doublet in the absorption spectra for the transition between excited states of cold cesium atoms," *Chinese Physics B*, vol. 19, no. 11, p. 113207, 2010. 6

[135] H. Zhang, L. Wang, J. Chen, S. Bao, L. Zhang, J. Zhao, and S. Jia, "Autler-townes splitting of a cascade system in ultracold cesium rydberg atoms," *Physical Review A—Atomic, Molecular, and Optical Physics*, vol. 87, no. 3, p. 033835, 2013. 6.2

[136] U. Raitzsch, R. Heidemann, H. Weimer, B. Butscher, P. Kollmann, R. Löw, H. Büchler, and T. Pfau, "Investigation of dephasing rates in an interacting rydberg gas," *New Journal of Physics*, vol. 11, no. 5, p. 055014, 2009. 6.2

[137] B. J. DeSalvo, J. Aman, C. Gaul, T. Pohl, S. Yoshida, J. Burgdörfer, K. Hazzard, F. Dunning, and T. Killian, "Rydberg-blockade effects in autler-townes spectra of ultracold strontium," *Physical Review A*, vol. 93, no. 2, p. 022709, 2016. 6.2

[138] T. Y. Abi-Salloum, "Electromagnetically induced transparency and autler-townes splitting: Two similar but distinct phenomena in two categories of three-level atomic systems," *Physical Review A—Atomic, Molecular, and Optical Physics*, vol. 81, no. 5, p. 053836, 2010. 7

[139] I. Beterov, D. Tretyakov, I. Ryabtsev, V. Entin, A. Ekers, and N. Bezuglov, "Ionization of rydberg atoms by blackbody radiation," *New Journal of Physics*, vol. 11, no. 1, p. 013052, 2009. 7.2.4

[140] G. Lehman, "Rate of ionisation of h and na rydberg atoms by black-body radiation," *Journal of Physics B: Atomic and Molecular Physics*, vol. 16, no. 12, p. 2145, 1983. 7.2.4

[141] W. Li, M. W. Noel, M. P. Robinson, P. J. Tanner, T. F. Gallagher, D. Comparat, B. Laburthe Tolra, N. Vanhaecke, T. Vogt, N. Zahzam, *et al.*, "Evolution dynamics of a dense frozen rydberg gas to plasma," *Physical Review A—Atomic, Molecular, and Optical Physics*, vol. 70, no. 4, p. 042713, 2004. 7.2.4

[142] L. Zhang, Z. Feng, J. Zhao, C. Li, and S. Jia, "Evolution of the pairs of ultracold rydberg atoms in the repulsive potential," *Optics Express*, vol. 18, no. 11, pp. 11599–11606, 2010. 7.2.4

[143] W. Li, P. J. Tanner, and T. F. Gallagher, "Dipole-dipole excitation and ionization in an ultracold gas of rydberg atoms," *Physical review letters*, vol. 94, no. 17, p. 173001, 2005. 7.2.4

[144] T. Amthor, M. Reetz-Lamour, S. Westermann, J. Denskat, and M. Weidemüller, "Mechanical effect of van der waals interactions observed in real time¡? format?¿ in an ultracold rydberg gas," *Physical Review Letters*, vol. 98, no. 2, p. 023004, 2007. 7.2.4

[145] S. A. Saakyan, V. A. Sautenkov, S. V. Klimov, A. A. Nazarov, A. A. Bobrov, and B. B. Zelener, "Excitation dynamics of interacting rydberg atoms in lithium magneto-optical trap," *Journal of Russian Laser Research*, vol. 44, no. 3, pp. 264–270, 2023. 7.2.4

[146] V. S. Chauhan, R. Kumar, D. Manchaiah, P. Kumar, and R. K. Easwaran, "Narrowing of electromagnetically induced transparency by using structured coupling light in 85rb atomic vapor medium," *Laser Physics*, vol. 30, no. 6, p. 065203, 2020. 8.2

[147] D. McGloin, G. C. Spalding, H. Melville, W. Sibbett, and K. Dholakia, "Applications of spatial light modulators in atom optics," *Optics Express*, vol. 11, no. 2, pp. 158–166, 2003. 8.2

[148] H. Weimer, M. Müller, I. Lesanovsky, P. Zoller, and H. P. Büchler, "A rydberg quantum simulator," *Nature Physics*, vol. 6, no. 5, pp. 382–388, 2010. 8.2

[149] X. Wu, X. Liang, Y. Tian, F. Yang, C. Chen, Y.-C. Liu, M. K. Tey, and L. You, "A concise review of rydberg atom based quantum computation and quantum simulation," *Chinese Physics B*, vol. 30, no. 2, p. 020305, 2021. 8.2